MEMBRANE INSERTED THERMO-ELECTROCHEMICAL GENERATOR FOR ENHANCED POWER GENERATION

SYED WAQAR HASAN

THESIS SUBMITTED IN FULFILMENT OF THE REQUIREMENTS FOR THE DEGREE OF DOCTOR OF PHILOSOPHY

FACULTY OF ENGINEERING
UNIVERSITY OF MALAYA
KUALA LUMPUR

2017

UNIVERSITY OF MALAYA
ORIGINAL LITERARY WORK DECLARATION

Name of Candidate: SYED WAQAR HASAN

Registration/Matric No: KHA140042

Name of Degree: DOCTOR OF PHILOSOPHY

Title of Project:

MEMBRANE INSERTED THERMO-ELECTROCHEMICAL GENERATOR FOR ENHANCED POWER GENERATION

Field of Study: RENEWABLE ENERGY

I do solemnly and sincerely declare that:

(1) I am the sole author/writer of this Work;
(2) This Work is original;
(3) Any use of any work in which copyright exists was done by way of fair dealing and for permitted purposes and any excerpt or extract from, or reference to or reproduction of any copyright work has been disclosed expressly and sufficiently and the title of the Work and its authorship have been acknowledged in this Work;
(4) I do not have any actual knowledge nor do I ought reasonably to know that the making of this work constitutes an infringement of any copyright work;
(5) I hereby assign all and every rights in the copyright to this Work to the University of Malaya ("UM"), who henceforth shall be owner of the copyright in this Work and that any reproduction or use in any form or by any means whatsoever is prohibited without the written consent of UM having been first had and obtained;
(6) I am fully aware that if in the course of making this Work I have infringed any copyright whether intentionally or otherwise, I may be subject to legal action or any other action as may be determined by UM.

Candidate's Signature Date:

Subscribed and solemnly declared before,

Witness's Signature Date:

Name:

Designation:

MEMBRANE INSERTED THERMO-ELECTROCHEMICAL GENERATOR FOR ENHANCED POWER GENERATION

ABSTRACT

Thermo-Electrochemical cells (Thermocells/TECs) transform thermal energy into electricity by means of electrochemical potential disequilibrium between electrodes induced by a temperature gradient (ΔT). Heat conduction across the terminals of the cell is one of the primary reasons for device inefficiency. Herein, Poly(Vinylidene Fluoride) (PVDF) membrane was embedded in thermocells to mitigate the heat transfer effects – these membrane-thermocells are referred to as MTECs. At a ΔT of 12 K, an improvement in the open circuit voltage (V_{oc}) of the TEC from 1.3 mV to 2.8 mV is obtained by employment of the membrane. The PVDF membrane is employed at three different locations between the electrodes i.e. x=2 mm, 5 mm, and 8 mm where 'x' defines the distance between the cathode and PVDF membrane. It was found that the membrane position at x=5 mm achieves the closest internal ΔT (i.e. 8.8 K) to the externally applied ΔT of 10 K and corresponding power density is 254 $nWcm^{-2}$; 78% higher than the conventional TEC. The thermal resistivity model based on infrared thermography has been proposed which explains the mass and heat transfer within the thermocells.

Furthermore, the dependence of physical and morphological properties of membranes on the MTEC performance was also examined. Investigating four membrane thicknesses of 100 μm, 200 μm, 400 μm and 600 μm, it was realized that membrane resistance increases by the thickness. We have found a significant correlation between the membrane thickness and maximum power generation as well. Membranes with all thicknesses significantly elevates the power density as compared to membrane-less TEC, however, maximum power density is achieved with 200 μm thick membrane. Moreover, effect of electrode-to-electrode separation was also investigated by examining two configurations (0.5 cm & 1.5 cm). Thus, highest power generation of 16 mW.m^{-2} is observed with the 200 µm thick PVDF membrane, 1.5 cm electrode-to-electrode separation and highly concentrated electrolyte (0.3M).

As the final segment of this experimental investigation, polymer fibrous composites were tested to amplify the thermal gradient across the cell. The highly thermal insulating composite mats of poly(vinylidene fluoride) (PVDF) and polyacrylonitrile (PAN) blends were used as the separator membranes. The fibrous membranes improve the thermal-to-electrical energy conversion efficiency of thermally driven electrochemical cells up to 95%. The justification of the improved performance is an intricate relationship between the porosity, electrolyte uptake, electrolyte uptake rate of the electrospun fibrous mat and the actual temperature gradient at the electrode surface. When the porosity is too high (87%) in PAN membranes the electrolyte uptake and electrolyte uptake rate were significantly high as 950% and 0.53 µLs^{-1}, respectively. In such a case, the convective heat flow within the cell is high and the power density is limited to 32.7 mW.m^{-2}. When the porosity was lesser (upto 81%) in PVDF membranes the electrolyte uptake and spread rate were relatively low as 434% and 0.13 µLs^{-1}, respectively. In this case, although the convective flows shall be low, however, the maximum power density of 63.5 mW.m^{-2} was obtained with PVDF/PAN composites as the aforementioned parameters were optimized. In addition, multilayered membrane structures were also investigated for which a bilayered architecture produces highest output power density of 102.7 mW.m^{-2}.

Keywords: thermoelectrics, electrochemical cells, polymer membranes, ionic liquids

MEMBRANE INSERTED THERMO-ELECTROCHEMICAL GENERATOR FOR ENHANCED POWER GENERATION

ABSTRAK

Sel-sel termo-elektrokimia (TEC) mengubah tenaga terma kepada tenaga elektrik dengan menggunapakai ketidakseimbangan keupayaan elektrokimia di antara elektrod-elektrod yang dihasilkan oleh perbezaan suhu. Kekonduksian haba merentasi terminal-terminal sel ialah salah satu penyebab utama yang mencetuskan ketidakcekapan alat ini. Membran poly(Vinylidene Florida) (PVDF) telah digunakan di dalam sel sel termo yang digunakan di dalam kajian ini untuk mengatasi masalah yang disebabkan oleh kesan pemindahan haba. Untuk perbezaan suhu sebanyak 12K, peningkatan voltan litar terbuka, Voc oleh TEC dari 1.3 mV sehingga 2.8 mV telah diperoleh dengan menggunakan membran. Membran PVDF telah digunakan pada 3 lokasi elektrod yang berbeza, contohnya pada x=2 mm, 5 mm, and 8 mm di mana x didefinisikan sebagai jarak di antara katod dan PVDF membrane. Kami telah mendapati bahawa posisi membran pada x=5 mm telah mencapai perbezaan suhu dengan kehilangan haba paling minimum iaitu dengan $\Delta T=8.8$ K apabila perbezaan suhu 10 K telah dijangka. Ketumpatan kuasa 254 nWcm^{-2}; 78% lebih tinggi dari TEC yang konvensional telah dicapai. Akhir sekali, model rintangan haba juga diperkenalkan berdasarkan termografi infra-merah yang boleh menerangkan mengenai perpindahan jisim dan haba di dalam TEC.

Tambahan lagi, kesan ketebalan membran juga telah dikaji ke atas kecekapan MTEC. Rintangan membran didapati meningkat selanjar dengan kenaikan ketebalan membran. Hubungan yang sangat penting/berimpak tinggi di antara ketebalan membrane dan penghasilan kuasa yang maksimum juga telah diperhatikan. Membran-membran dengan semua jenis ketebalan yang dikaji menunjukkan kenaikan di dalam ‘power density’ berbanding dengan TEC tanpa membran, walaubagaimanapun, ‘power density’ yang maksimum dicapai oleh membran berketebalan 200 µm. Tambahan lagi, kesan penjarakan elekrod ke elektrod juga telah dikaji dengan memeriksa dua konfigurasi jarak (0.5 cm & 1.5 cm). Dengan itu, kuasa yang paling tinggi dihasilkan ialah sebanyak 16 $mW.m^{-2}$ oleh PVDF membran dengan ketebalan 200 µm dan jarak elektrod ke elektrod sejauh 1.5 cm dengan elektrolit berkepekatan 0.3M. Membran-membran PVDF dan larutan-larutan elektrolit dikaji dengan lebih mendalam dengan menggunakan FT-IR, CV dan SEM. Akhirnya, keputusan-keputusan dari kajian ke atas MTEC dan TEC dijelaskan lagi dengan mencadangkan model rintangan elektrik yang sehubungan dengannya.

Bahan baharu sebagai membran untuk aplikasi MTEC sedang dikaji iaitu PVDF-HFP, PAN (Poly-Acrylonitrile) dan PEO (Poly-Ethylene Oxide) walaupun sebelum ini cuma membran konvensional sahaja digunakan di dalam semua set eksperimen kajian yang dijalankan. Membran-membran ini disediakan melalui dua metod iaitu Inversi Fasa dan ‘Electrospinning’ untuk mendalami morfologi membran ke atas prestasi MTEC. Eksperimen-eksperimen telah pun lengkap dan untuk masa semasa analisis yang teliti dan mendalam sedang dijalankan.

Keywords: termoelektrik, sel-sel elektrokimia, membrane-membran polimer, cecair ionik

ACKNOWLEDGEMENTS

I start this acknowledgment with a sincere thanks to the Creator of this universe, who created me and blessed me with the ability to think, question and find the answers. Indeed, exploring science is a great way to acknowledge His presence, magnificence and authority.

In this wonderful journey of my Ph.D. studies there have been some remarkable personalities who have a great contribution not only in my research but also on my personality. First of all, I am indebted to **Dr. Suhana Mohd Said** and **Dr. Ahmad Shuhaimi** for accepting me as a Ph.D. student. Their technical support, valuable suggestions and precious time have been a great help throughout my research. The meetings and discussions with **Dr. Mohd Faizul Mohd Sabri** also have a significant impact on my work. I also acknowledge the worthy time I spent at Guangxi Univeristy, China with **Prof. Guoqiang He** at his laboratory as a visiting researcher. The University of Malaya has been a wonderful place for me where, although, I am a foreigner but the loving and friendly nature of my Malaysian labmates made me feel like home. I want to thank Shafinie Surapandi, Aisyah, Shahrir Razey, Megat Mohammad Iksan and all other labmates for making my life convenient at University Malaya. Especial thanks to my friends Zain Taha, Imran Haider, Hasan Abbas and many others for all of the lovely memories.

Finally my family! I have no words to express my love and gratitude to my father. I still remember the days of my undergraduation in which my father, **Prof. Syed Muhammad Iqbal**, used to encourage me for the academic career. My brother, **Dr. Faraz Hasan** has always been an inspiration and a role model for me, I am grateful for all of his efforts and help he offered for me to secure scholarships for my higher studies. My sweet “**shillo**”, respected **bhabhi** and caring **Khadeeja** – thank you all for your love. And finally, the love of my life my mother. **Ammi Jan**, I know you have been missing me - I love you.

TABLE OF CONTENT

LIST OF FIGURES

LIST OF TABLES

LIST OF SYMBOLS AND ABBREVIATIONS

TE	Thermoelectric
TEC	Thermo-electrochemical cells
MTEC	Membrane-embedded Thermo-electrochemical cells
CO	Carbon monoxide
CO_2	Carbon dioxide
GISS	Goddard Institute for Space Studies
Th	Higher temperature (K)
Tc	Colder temperature (K)
ΔT	Temperature/Thermal gradient (K)
ΔT_{calc}	Calculated temperature (K)
ΔT_{act}	Actual temperature (K)
T	Absolute temaperature (K)
Voc	Open-circuit Voltage (mV)
ΔV	Potential gradient (mV)
Se	Electrochemical Seebeck (mV/K)
σ	Ionic conductivity ($S.cm^{-1}$)
ρ	Ionic resistivity (Ω.cm)
α	Seebeck coefficient (mVK^{-1})
K_{th}	Thermal conductivity ($W.m^{-1}K^{-1}$)
K_{elec}	Electronic contribution of thermal conductivity ($W.m^{-1}K^{-1}$)
K_{latt}	Phononic contribution of thermal conductivity ($W.m^{-1}K^{-1}$)
η	Efficiency
ZT	Dimensional-less figure of merit of thermoelectric materials

n	Carrier concentrations (cm^{-3})
Nr	Reduced ion flux density ($mol.m^{-2}s^{-1}$)
No	Oxidized ion flux density ($mol.m^{-2}s^{-1}$)
j	Current density ($A.m^{-2}$)
F	Faraday constant ($C.mol^{-1}$)
Z	Ion charge number
D	Diffusion coefficient (m^2s^{-1})
C	Concentration ($mol.m^{-3}$)
Q_o	Heat of transport of oxidized ions ($J.mol^{-1}$)
Q_r	Heat of transport of reduced ions ($J.mol^{-1}$)
R	Gas constant ($Jmol^{-1}K^{-1}$)
Φ	Potential difference (mV)
$Fe(CN)_6^{3-}/Fe(CN)_6^{4-}$	Ferri/ferrocyanide redox couple
I^-/I_3^-	Iodide/triiodide redox couple
Fc/Fc^+	Ferrocene/ferrocenium redoc couple
Cu^{2+}/Cu	Copper/Copper sulphate redox couple
DMSO	Dimethyl sulfoxide
MPN	3-Methoxypropionitrile
NMP	1-Methyl-2-Pyrrolidinone
DMF	N,N-Dimethylformamide
PC	Polycarbonate
ACN	Acetonitrile
PEDOT:PSS	
R_{MT}	Mass transfer resistance (Ω)

R_{OHM}	Ohmic resistance (Ω)
R_{CT}	Charge transfer resistance (Ω)
SS	Stainless Steel
RGO	Reduced Graphene Oxide
Nu	Nusselt number
Sh	Sherwood number
Le	Lewis number
E(T)	Electrode Potential (V)
ΔS_{rc}	Entropy change of redox couple
P	Power Density ($W.m^{-2}$)
Z’	Real component of impedance (Ω)
Z’’	Imaginary component of impedance (Ω)
Φ_{in}	Inner diameter (mm)
Φ_{out}	Outer diameter (mm)
e-to-e	Electrode-to-electrode separation
ΔE_p	Peak separation (V)
i_{pc}	Cathodic peak current (A)
i_{pa}	Anodic peak current (A)
A	Electrode area (m^2)
R_b	Bulk resistance (Ω)
U	Spread rate ($L.s^{-1}$)

$[C_4mim][BF_4]$	1-Butyl-3-methylimidazolium Tetrafloutoborate
$[EMIM][EtSO_4]$	1-Ethyl-3-methylimidazolium Ethylsulphate
[PMIM]	3-Propyl-1-methylimidazolium Iodide
[BMIM]	1-Butyl-3-methylimidazolium Iodide
PVDF	Poly-Vinylidene Flouride
PVDF-HFP	Poly-Vinylidene Flouride co-hexafluoropropylene
PAN	Poly-Acrylonitrile

CHAPTER 1: GENERAL INTRODUCTION

Scientists and researchers bear a serious responsibility to address the issues and challenges faced by the human community for their convenient lifestyles and safe ecological environment of the universe. In this 21st century all the major human developments are based on electricity. Since the 1st law of thermodynamic states that energy can neither be created nor destroyed, however; it can be transformed from one to another forms (Riedi, 1976). Therefore, electric energy can only be harnessed out of some other form of energy, for example, in internal combustion engines (ICEs) chemical energy of the fossil fuel is transformed first to mechanical work and later to electrical energy (Demirel, 2012). Or in case of steam engines, coal or fossil fuel (petroleum/diesel) is used to produce superheated steam which later runs a turbine coupled with an electric generator which generates electricity (Demirel, 2012). Although, these mechanical engines have high Carnot efficiency, however; they significantly pollute the global environment with green-house gases including Carbon monoxide (CO) and Carbon dioxide (CO_2). These gases are hazardous to the ecological system of the world rising the global temperature(Dincer, 2000; Jadhao & Thombare, 2013). The NASA Goddard institute for space studies (GISS) shows that the global temperature has rapidly increased over the past 6 decades owing to these green-house gases(Ali Hussain Kazim, 2017). It has been estimated that for a safer environment the global temperature should not exceed 2˚C, however, the GISS shows that currently the global temperature has been increased to 0.8˚C and is in the increasing trend as almost 81.1% of the desired electricity is generated from the fossil fuel. In order to minimize the green-house gases the trend to convert the chemical energy of the fossil fuels into electricity has to be replaced by clean or green energy conversion. The clean energy technology refers to the energy conversion (or more specifically electricity generation) from the natural resources including solar, wind, geothermal and biofuels etc. These natural resources suffice our electricity need with zero green-house gases emissions for an instant (a) transforming the light energy of the sun into electricity, (b) utilizing work energy of wind, tides, or flowing water to rotate a turbine-generator system to generate electricity or (c) consuming the geothermal energy (i.e. the under-ground heat of the earth) to run a steam turbine. All of these techniques are some examples of 'Clean energy technologies'(Dincer, 2000).

Amongst many clean energy generators, thermo-electric (TE) devices have uniqueness i.e. in addition of generating clean and scalable electricity TE devices can be used to recover waste-heat from mechanical engines. The Carnot efficiency of a mechanical engine is generally limited to 40~44% which indicates that almost 60% of the heat energy is wasted in the environment. The US Department of Energy (DOE) estimates this 60% of heat loss as the loss of $6 million per year. Nevertheless, thermoelectric modules can be utilized to harness electricity from this waste-heat. Supplementary advantages of thermoelectric energy conversion include silent operation, no maintenance cost and no moving/translating/rotation parts.

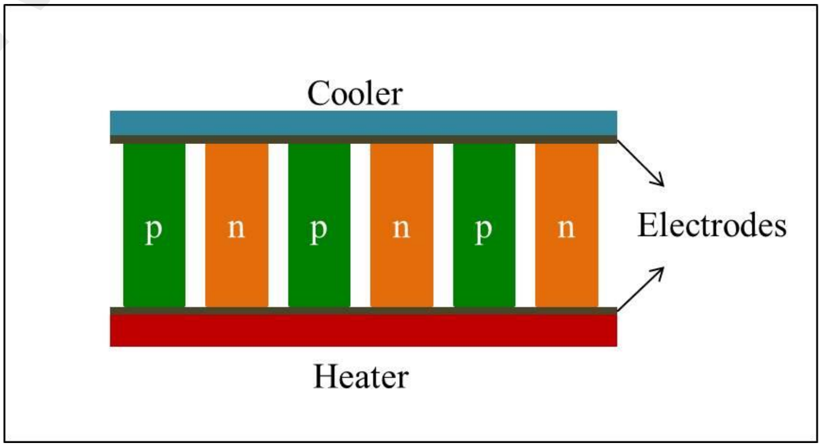

Figure 1.1: Thermoelectric model

1.1 Working Principle of Thermoelectric Modules

Thermoelectricity, a phenomenon where a temperature gradient is converted into electricity, is a topic of intense research interest primarily for energy harvesting applications. A conventional thermoelectric (TE) module consists of an array of p- and n-type semiconducting materials assembled between two electrodes maintained at different temperatures as shown in Figure 1.1(Tritt, 2011). The state-of-the-art TE materials for room temperature applications include chalcogenide materials like Sb_2Te_3 and Bi_2Te_3 (Poudel et al., 2008). The efficiency of a typical TE device is governed by the temperatures of the hot and cold electrodes (Th and Tc) as well as the intrinsic properties of TE materials. Thus, a dimensionless Figure of merit (ZT) is defined by equation (1.1) as a quantitative measure of energy conversion capability of TE materials (p- and n- type materials).

$$ZT = \left(\frac{\sigma \cdot \alpha^2}{K_{elec} + K_{latt}} \right) \cdot T \tag{1.1}$$

where "σ" is electrical conductivity (S/m), "α" is the thermoelectric, or "Seebeck", coefficient (V/K), "T" is the absolute temperature (K) while K_{elec} and K_{latt} are the electronic and lattice contribution of thermal conductivity (W/m·K) of the material, respectively(Martín-González, Caballero-Calero, & Díaz-Chao, 2013; Mohanraman et al., 2015; Snyder & Toberer, 2008). Therefore, the overall device efficiency (η) in the literature (Telkes, 1947) is expressed as:

$$\eta = \frac{\sqrt{1+ZT} - 1}{\sqrt{1+ZT} + \left(\frac{Tc}{Th} \right)} \tag{1.2}$$

Researchers have subjected intensive efforts to attain higher ZT values through various routes but the highest value in bulk materials is around 1.4 – 1.6 which is still insufficient for large scale industrial applications (Poudel et al., 2008). The foremost challenge to exceed the ZT value is to overcome the interdependency of electronic and thermal properties of the materials. The equation (1.1) suggests that a high ZT is dependent on high electrical conductivity (σ) and Seebeck coefficient (α), and low thermal conductivity (K). Furthermore, an increase in charge carrier concentration (n, cm^{-3}) will have a proportional effect of increasing σ, but decreasing α. Thus, there is a significant tradeoff between the three key parameters σ, α and K, where typically a material of high electrical conductivity will also have high thermal conductivity, but consequently low ZT. Strategies such as phonon glass electron crystal (PGEC) structures, quantum dots and superlattices have been devised in order to provide both high electrical conductivity and low thermal conductivity(Martín-González et al., 2013).

In recent times, novel thermoelectric effects apart from the semiconductor-based Seebeck effect have been introduced, such as the Spin Seebeck effect and the electrochemical Seebeck effect. The electrochemical Seebeck effect arises in thermo-electrochemical cells (TECs), when a solution containing a redox couple is subjected to a temperature gradient. The temperature gradient between the electrodes disturbs the electrochemical potential equilibrium between the electrolyte and electrode surface causing the current to flow when the circuit is complete(Brian Burrows, 1976; Mua & Quickenden, 1996; Quickenden & Mua, 1995). This effect can result in significantly high Seebeck coefficients of redox electrolytes, which translate into potentially high power outputs. Furthermore, these solutions generally possess low thermal conductivity, which can contribute to a higher thermoelectric figure of merit.

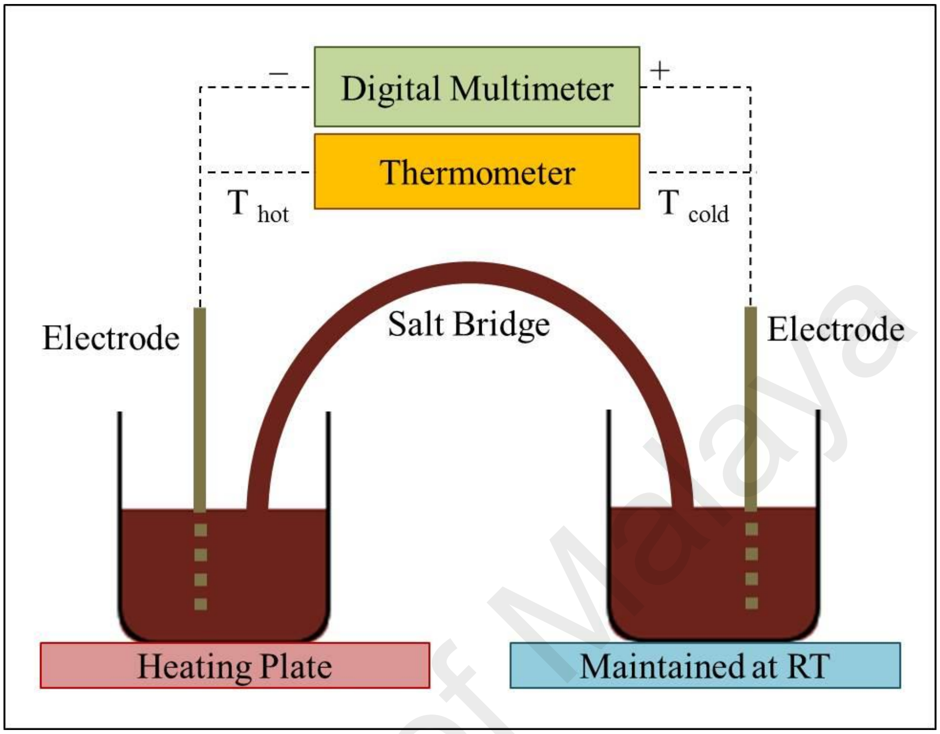

Figure 1.2: Two-beaker arrangement of Thermo-Electrochemical Cell

1.2 Working Principle of Thermo-electrochemical Cells

Thermo-electrochemical cells (TECs), traditionally known as thermo-galvanic cells, have been studied since the early 1980s (Brian Burrows, 1976; Chum, Fahlsing, & Jayadev, 1980; Quickenden & Vernon, 1986). TECs generate steady electric current by the virtue of a temperature gradient between the two electrodes placed in an electrolyte. Conventionally, characterization of the electrochemical Seebeck coefficient, S_e, is conducted using a two-compartment setup, connected by a salt bridge, which allows a physical pathway for ion transfer between the two compartments(Gunawan et al., 2013). The two compartments are subjected to a temperature gradient (ΔT), and ion migration is enabled from the hotter compartment to the colder compartment through the salt bridge as shown in Figure 1.2. Thermal gradient created between the two electrodes placed in a redox electrolyte disturbs the electrochemical potential equilibrium between the electrodes and the electrolyte; creating a potential drop. The resulting potential difference (ΔV) is used as the basis for the calculation of S_e (where $S_e=\Delta V/\Delta T$). The thermoelectric effects in liquids can be studied in either a two-beaker arrangement or a cell configuration as shown in Figure 1.2 and Figure 1.3, respectively. Thus steady-state current can be drawn from the circuit on load conditions. The electrons contributing in the current flow are produced by reduction-oxidation reaction taking place at anode and cathode, respectively. Thus, the current density (j; A m^{-2}) in the circuit is balanced by the ion flux density (N_r & N_o; mol m^{-2} s^{-1}) from hotter to colder electrodes as represented by Salazar et al (Salazar, Kumar, & Cola, 2014) in equation 1.3.

$$j = \Sigma F(Z_\mathrm{r}N_\mathrm{r} + Z_\mathrm{o}N_\mathrm{o}) \cdot \bar{n} \tag{1.3}$$

where F is Faraday constant (C mol^{-1}), Z is the ion charge number, and $\bar{n}$ is the number of electrons transferred in the redox reaction. Since redox systems have 2 way ion transport mechanism suffixes “o” and “r” represents oxidized and reduced species, respectively. In iodide/triiodide ($\mathrm{I}^-/\mathrm{I}_3^-$) redox couple, reduced species are generated at electrolyte/cathode interface when cathode donates two electrons to Iodine molecule (I_2) transforming it into tri-iodide ion (I_3^-). Tri-iodide ions carry those additional electrons to anode where they release the electrons and get back to Iodine ion (I^-) as shown in equations (1.4) and (1.5) and Figure 1.3.

$$\mathrm{I}_2 + \mathrm{I}^- \leftrightarrow \mathrm{I}_3^- \tag{1.4}$$

$$\mathrm{I}_3^- + 2\mathrm{e}^- \leftrightarrow 3\mathrm{I}^- \tag{1.5}$$

Now the oxidized species (I^-) return back to cathode and thus the cycle is continuous. This ionic transport mechanism i.e. ionic flux is influenced mainly by the thermal gradient between the two electrodes; however, concentration gradient and potential gradient between the electrodes also contribute towards this flux as explained by Salazar et al in equation 1.6 (Salazar, Kumar, et al., 2014; Salazar, Stephens, Kazim, Pringle, & Cola, 2014).

$$N_{o,r} = C_{o,r}\bar{u} - D_{o,r}\,\nabla C_{o,r} - Z_{o,r}FC_{o,r}\nabla\phi - \left(\frac{Q_{o,r}}{RT^2}\right) D_{o,r}\,C_{o,r}\nabla T \qquad (1.6)$$

where $D, C, Q_{o,r}$ and $\bar{u}$ are diffusion coefficient ($m^2\ s^{-1}$), concentration (mol m^{-3}), heat of transport (J mol^{-1}) and bulk vector velocity (m s^{-1}) of the transporting ions, respectively. R is the gas constant (J mol^{-1} K^{-1}), T is the temperature (K) and symbol “∇” represents the gradient. The term $C_{o,r}\bar{u}$ represents the **natural convection** of the ions. The second term ($-D_{o,r}\,\nabla C_{o,r}$) is referred to as **diffusion** which happens due to the concentration gradient created during the redox reaction at electrode/electrolyte interface. The third term ($-Z_{o,r}FC_{o,r}\nabla\phi$) represents the **migration** of ions under the effect of potential difference between the electrodes. Nevertheless, the most significant influence is of thermal gradient which generates **Soret effect** (thermal-diffusion) within the thermocell represented by the last term (Salazar, Stephens, et al., 2014). Hence the recent reports indicate high convection and faster ionic diffusion rate as key parameters for optimised TEC performance (Abraham, MacFarlane, Baughman, et al., 2013; Gunawan et al., 2014; Salazar, Stephens, et al., 2014). We show that by a simple, easy to fabricate and inexpensive mesoporous polymer membrane employed between the two electrodes in thermocells, the output power density increases from nano-Watts to milli-Watts. The polymer membrane has the role of improving thermal gradient across the cell and simultaneously reducing the charge transfer resistance between the electrode and electrolyte interface. In our previous report (Hasan et al., 2016), we illustrated the advantage of PVDF membrane in terms of mitigating the heat flow between the electrodes. In this work we aim to relate the power density of MTEC with electrical resistance and ionic conductivity of membranes. For further optimization of TEC we also investigated the role of electrolyte concentration and electrode-to-electrode separation.

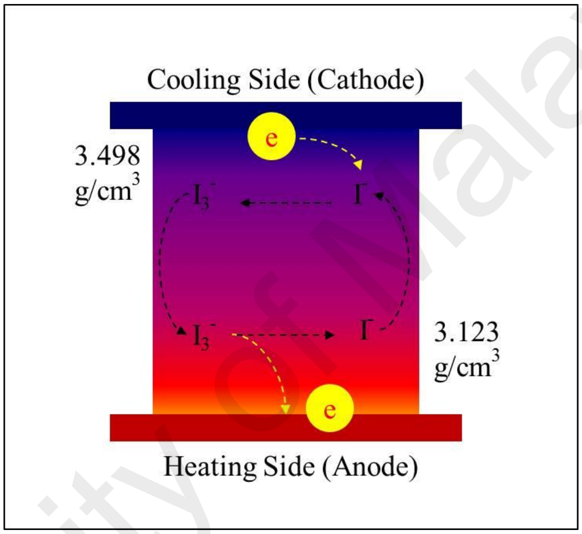

Figure 1.3: Cell configuration of Thermo-Electrochemical Cell

1.3 Problem Statement

For application of these devices, the TEC is used as a cell structure as shown in Figure 1.3 where the electrolyte and both the electrodes are confined in a single chamber. The ion transport within the cell configuration is a complex combination of natural convection, migration, thermal and chemical diffusion. Although, cell configuration is practically more applicable but maintaining the temperature gradient between electrodes is a key challenge which limits the performance of the TEC, as the thermal conductivity of the electrolyte solution will inevitably reduce ΔT. Typical strategies to maintain the integrity of the temperature gradient in the “cell configuration” include an auxiliary cooling system on the cold side electrode, which adds complexity, cost and bulk to the overall system. Thus, in this work, the inclusion of a mesoporous membrane in the TEC is used as a strategy for mitigating heat flow across the TEC whilst maintaining ionic transfer between the cathode and anode.

1.4 Research Objectives

The principal research objective of this dissertation is to comprehend the role of a porous polymer membrane in the power generation characteristics of thermocells. Subjectively the objectives are listed as follows:

1. **To study and identify the impact of a membrane on the thermal transport within the thermocell.** Furthermore, it also the topic of interest that how does the membrane position between the electrodes can affect the actual temperature gradient between the electrodes.
2. **To experimentally optimize the morphological, physical and electrical properties of the membrane for high power density of thermocells.** Moreover, it is interesting to investigate if these properties, especially membrane thickness, porosity and ionic resistance, have any inter-dependent relation.
3. **To experimentally evaluate different polymers and composites as potential membrane materials.** Additionally, electrospinning and phase inversion techniques have to be compared for membrane synthesis.
4. **To formulate an equivalent electrical circuit of membrane-embedded thermocells to fully analyze the role of the membranes.**

1.5 Thesis Outline

The focus of this thesis is to harness clean and scalable electricity out of the thermal energy using thermo-electrochemical cells (TECs). Currently, the utilization of TECs for practical applications is limited owing to lower output power densities and lower cell efficiency. The newer design of TECs incorporating a mesoporous polymer membrane is invented referred to as MTECs (Membrane embedded thermocells). This thesis explains the role of the membrane on power generation characteristics of MTECs, furthermore, the physical and morphological optimization of the membranes is also discussed for improvement in power density. The thesis is outlined as follows:

The chapter 1 is dedicated for the general introduction of the field. It gives a brief overview of the current energy crisis we presently face owing to the limited amount of fossil fuel and the global warming. Hence it is the need of time to expand thermoelectric research which can simultaneously fulfill our energy demands and also maintain the global temperature upto the desired level. The chapter further discusses the working principles of solid-state thermoelectric modules and thermo-electrochemical cells followed by the problem statement addressing the reason of lower efficiencies of thermoelectric modules. The chapter is concluded with a description of the strategy to improve the cell performance and specific research objectives of this research thesis.

The literature review of the thermo-electrochemical cells is presented in chapter 2. The research and developments over several decades subjected on electrolytes, electrodes, redox couples and physical geometry of thermocells has been thoroughly discussed.

Although, the experimental work on membranes starts from chapter 4, nevertheless, it was necessary to show the significance of this research theme i.e. to limit the thermal flow across the cell. Therefore, the chapter 3 is dedicated to explain the role of electrolyte thermal conductivity on the cell performance. With the ionic liquid, namely 1-Ethyl-3-Methylimidazolium Ethylsulfate [(EMIM)($EtSO_4$)], it is shown that the increased thermal conductivity of the electrolyte can seriously deteriorate the power outputs.

The main research begins with the question **"Whether it is good for TEC performance to place a porous membrane in between the electrodes?"** The motivation to place the membrane is to hinder the convective heat flow across the cell which is the main source of lower power densities and efficiency. Therefore, TECs with membranes (MTECs) are prepared and compared with the performance of the conventional membrane-less TEC. The experimental details and the results are elaborated in Chapter 4. In the same chapter, it is shown that a position of the membrane between the electrodes can significantly impact the power generation, however, at any particular position MTECs perform better than TECs. Finally, in chapter 4, thermal resistive models for TEC and MTECs are presented; explaining the increased thermal resistivity of MTECs as the main reason for the performance improvement.

Once the positive outcomes of the membrane in MTECs were experimentally proven, the research was expanded in search of optimized physical and morphological properties of the membranes. The main motivation of the chapter 5 was **"Is there any threshold thickness of the membrane suitable for the MTEC performance?"** Moreover, an intricate relationship between the membrane thickness, porosity, and ionic conductivity of the memrbanes is presented and discussed in details.

The further experimental investigation of this thesis was carried out with the motivation **"What type of materials can be ideal for MTECs?"** The target was to study the behavior of different polymers and their composites in MTECs. Additionally, it was necessary to compare phase inversion method and electrospinning technique to prepare the membranes. The results are presented and explained in chapter 6.

The chapter 7 is an attempt to propose an equivalent electrical model of TEC and MTECS. In this chapter Electrochemical Impedance Spectroscopy (EIS) of TEC and MTECs is used to generate the Nyquist plots. The EIS curve fitting is used to propose the electrical models.

Finally, this thesis is complemented with a detailed conclusions and summarization of the key findings of this research. Moreover, recommendations have also been added which will be beneficial for the future MTEC research. The conclusions and the recommendations are presented in chapter 8.

CHAPTER 2:

LITERATURE REVIEW

The charm of converting the waste heat into useful and scalable electricity has always been the attraction in thermo-electrochemical cells and literature since 1970s can be found on this subject(BW Burrows, 1975; Brian Burrows, 1976; Chum et al., 1980; Markov & Kuzyakin, 1972; Quickenden & Vernon, 1986). Thermocells, traditionally referred to as thermo-galvanic cells, are galvanic cells with an electrolyte and two electrodes in a non-isothermal state. Unlike batteries, the electrodes of thermocells can be of homogeneous composition and the driving force of the electron transfer is mainly the different temperatures at which the electrodes are maintained. However, a limitation in the previous decades was the only aqueous based redox electrolytes were available which limited the working temperature of thermocells upto ~ 100 ˚C(Mua & Quickenden, 1996; Quickenden & Mua, 1995). This stalemate was overcome recently in 2011 by Abraham et al when ionic liquids proved to be suitable base solutions for redox couples(Abraham, MacFarlane, & Pringle, 2011). The high thermal stability and non-volatility of ionic liquids now allow the thermocell application at higher temperatures (~200 ˚C) which is a competitive temperature zone with the solid-state thermoelectric materials e.g. Bi_2Te_3 and Sb_2Te_3. In this section, we shall mention all the stages of the research history of thermo-electrochemical cells. Thermocells, as shown in Figure 1.2 and 1.3 has four major components namely redox couples, base electrolytes, electrodes, and thermocell body and for each of these components researchers have conducted various studies which we present in the coming sections.

2.1 Electrolytes

The role of electrolytes which become the base for the redox reaction is very significant in the performance of thermocells. An ideal base electrolyte should have low viscosity, high ionic diffusion, high thermal stability, and high electrochemical window. If the viscosity is too high the thermal gradient will be improved between the two electrodes, however, the high viscous solutions also have low ionic diffusion thus the overall power generation will be diminished. A range of electrolytes may be utilized in TEC applications which can be generalized in three main categories namely aqueous redox solutions, organic redox solutions, and molten salts (and Ionic Liquids). The initial studies of thermogalvanic cells (a traditional name of modern thermocells) are published with aqueous electrolytes containing redox couples. Generally, aqueous electrolytes perform better than many other solvents owing to the relatively faster ionic diffusions. The $Fe(CN)_6^{3-}/Fe(CN)_6^{4-}$ is the most favorable redox compound for aqueous media as it has shown high electrochemical Seebeck values (S_e) of -1.4 mV/K and highest efficiency of 1.4% (Hu et al., 2010). However, the low boiling point of water and quicker evaporation rate has always been a source of limitation for the aqueous thermocells in practical implementation. Thus, all reports utilizing aqueous media for redox couple dissolution are limited under the operating condition of <100˚C. In this scenario, liquids with higher boiling temperature and better thermal stability like ionic liquids and organic solvents are preferred. Moreover, those redox couples which are unstable or undissolved in water media can be easily prepared in non-aqueous electrolytes.

A break-through strategy in molten salt thermo-electrochemical research was to utilize Ionic Liquids with redox solutions in thermocells as reported by Abraham and coworkers in 2011(Abraham et al., 2011). The ILs are low melting temperature organic salts composed of a bulky organic cation (imidazoliums, pyrrolidinium or alike) and an organic (e.g. ethyl sulphate) or inorganic (Cl^- or I^- etc) anion. Thermal stability of ILs (~200˚C) now enables moderate temperature thermo-electrochemical characterization; which carries a huge potential for large scale industrial applications of thermocells. In addition of having higher boiling temperatures and low vapor pressures, ILs also have tunable ionic conductivities and relatively lower thermal conductivities(Armand, Endres, MacFarlane, Ohno, & Scrosati, 2009; Singh et al., 2012; Wei & Ivaska, 2008). Furthermore, the wide range of electrochemical windows of ILs also enables higher Seebeck coefficents of redox couples. All of these factors give a highly encouraging potential of higher power outputs in thermocells containing ILs as the base electrolytes. In one of the initial reports describing the role of ILs in thermocell applications, several Fe and Cr based redox couples was prepared in 1-butyl-1-methylpyrrolidinium bis(trifluoro-methanesulfonyl)amide ([C_4mpyr][NTf]). They found that the sign of the Seebeck coefficient of the redox couple depends upon the charge numbers of the oxidant and reductant species in the couple. If the charge of oxidant is larger than the reductant, the Seebeck coefficient is positive and vice versa. It is interesting to note that the Seebeck coefficient of $[Fe(CN)_6]^{3-/4-}$ in ([C_4mpyr][NTf]) is -1.49 mVK-1 which is very closer to the aqueous $[Fe(CN)_6]^{3-/4-}$(Migita, Tachikawa, Katayama, & Miura, 2009). In a separate study many Fe-based redox couples were prepared in different ILs. Although, none of the solutions resulted in higher Seebeck coefficient as compared with the aqueous solution but a relation between the seebeck coefficient and the charge density of the ionic liquid was established. The authors observed that with higher charge density of the ionic liquids the Seebeck coefficient is increased(Yamato, Katayama, & Miura, 2013). In a recent study, Abraham et al firstly studied S_e of 0.4 M iodide/triiodide redox (I^-/I_3^-) in water and various Ionic Liquids (ILs) namely methyoxy-propionitrile, [C_2mim][BF_4], [$P_{4,4,4,6}$][NTf_2], [C_2mim][NTf_2],

[C_4mpyr][NTf_2], [C_2mim][$B(CN)_4$] and [$P_{2,2,2,(101)}$][NTf_2]. The highest Se of 0.53 mVK^{-1} was noted in water solution followed by methylpropionitrile (0.34 mVK^{-1})(Abraham, MacFarlane, Baughman, et al., 2013; Abraham et al., 2011; Abraham, Tachikawa, MacFarlane, & Pringle, 2014). In ILs, [C_2mim][BF_4] performed better than all others exhibiting the Se of 0.26 mVK^{-1} which is quite lower as compared to the aqueous solution. However, the hot electrode in case of [C_2mim][BF_4] was maintained at 130˚C expressing the advantage of high temperature applications. They further showed that higher Seebeck values can be obtained in diluted solution i.e. the Se value for [C_2mim][BF_4] gradually decreases from 0.47 mVK^{-1} to 0.26 mVK^{-1} as the concentration is increased from 0.02 to 0.4 M. Since there are several hundred ILs presently available, some researchers have developed simulation models anticipating the Se performance of particular ILs for thermocell applications. A. Sosnowska et al estimated the Seebeck coefficient values for ILs with 0.01 M I-/I3- redox couple using read-across analysis and quantitative structure property relationship (QSPR) and found a deep relation between the Seebeck value, size, symmetry, branching of cations and vertical electron-binding energy of the anion. The authors concluded that Seebeck coefficient is highest with ILs consisting of small, less branched and relatively symmetric cations, along with anions with a high vertical electron binding energy(Sosnowska et al., 2016).

A limitation associated with ILs which reduces the thermocell performance is their relatively higher viscosity. Higher viscosity implicates slower rates of redox ion diffusion rate(Abraham, MacFarlane, & Pringle, 2013). On the other hand, aqueous solution or organic solvents which generally have lower viscosity do not face the challenge of low ionic diffusion rates, rather they have their own circumstances such as higher charge transfer resistance. Thus, mixtures of ILs and organic solvents have already been studied to address the slow ionic diffusion of ILs. A very early study of the mixed solutions was reported with [C_2mim][BF_4] and acetonitrile using thiolate/disulfide organic redox couple. The neat acetonitrile exhibited the Seebeck coefficient of 0.13 mVK-1 which gradually increased with the addition of [C_2mim][BF_4] reaching the maximum of 0.6 mVK^{-1} at 5.5 M solution(Zinovyeva, Nakamae, Bonetti, & Roger, 2014). The effect of viscosity on TEC performance is very subjective on the nature of ILs. For example the Seebeck coefficient of 0.1 M $Co^{2+/3+}(bpy)_3(NTf_2)_{2/3}$ in two mixed solutions of DMSO/[C_2mim][eFAP] and MPN/[C2mim][$B(CN)_4$] was found to decrease with increasing IL composition(Lazar, Al-Masri, MacFarlane, & Pringle, 2016). In some particular ILs e.g. trihexyl(tetradecyl)phosphonium ([$P_{6,6,6,1,4}$])[BF_4] had no influence on the Seebeck coefficient of 0.1 M $Co^{2+/3+}(bpy)_3(NTf_2)_{2/3}$. The highest reported Seebeck coefficient of 2.19 mVK^{-1} of 0.1 M $Co^{2+/3+}(bpy)_3(NTf_2)_{2/3}$ in non-aqueous solution i.e. MPN. In the same report, the performance of MPN is compared with other ILs, however, the MPN exceeds all the ILs in terms of Seebeck value. This is because of better ionic diffusion and low mass transfer resistance of MPN. However, [C_2mim][$MeSO_3$] in the same redox couple has resulted in the Seebeck of 2.13 mVK^{-1} which is slightly lower than MPN. The Seebeck coefficient does not exceed this value even if the PC (Polycarbonate) is added in the IL i.e. the highest Seebeck of 2.16 mVK^{-1} in IL:PC is observed. However, in an another report the Seebeck coefficient of the same redox couple has largely increased from 1.6 mVK^{-1} in pure [C_2mim][eFAP] to ~ 2 mVK-1 when DMSO is added in the IL (upto 75%) (He, Al-Masri, MacFarlane, & Pringle, 2016). Whilst the role of organic solvents (PC, DMSO or MPN) in IL may not be distinguishable in terms of Seebeck coefficient, but significant difference can be observed in terms of power generation. For example, the power density of pure [C_2mim][$B(CN)_4$] and MPN containing $Co^{2+/3+}(bpy)_3(NTf_2)_{2/3}$ redox couple is found to be ~200 $mW.m^{-2}$ and ~450 $mW.m^{-2}$ respectively, however in the mixture of these two solutions the power density is higher in all the compositions touching ~780 $mW.m^{-2}$ in the 75:25 MPN:IL ratio. Similar observation has been noted with [C_2mim][eFAP]/DMSO mixtures.

In recent publications, researchers have proposed a novel idea of "composite electrolytes" in thermocells. The composite electrolytes refer to the electrolytes containing additives like CNTs or PEDOT:PSS (Black, Murphy, Atkin, Dolan, & Aldous, 2016; Ali H Kazim & Cola, 2016; Lazar et al., 2016; Salazar, Stephens, et al., 2014; Zhou, Yamada, & Kimizuka, 2016). Magnetically stirring an electrolyte during thermo-electrochemical characterization is another way to impart turbulence in electrolytes as presented by Salazar et al (Salazar, Stephens, et al., 2014). They prepared multiwalled Carbon Nanotube (MWCNT) mixed ionic liquids as the electrolyte solution and placed a magnetic bar in the cell. Without stirring, the inclusion of MWCNTs in ionic liquids results in a decreasing trends of power density curve. However, an improvement of 25% in power density was achieved by stirring the solution (400 rpm) as compared to stagnant electrolytes. In fact without any MWCNT inclusion the power density of stirred electrolyte resulted as 24.5 mW/m^2 which is 1.4 times higher than the motionless electrolytes. Simultaneously the fast ionic diffusion adversely affect the thermal stability between the electrodes, as the quickly diffusing ions will also carry thermal energy from one to another electrode destabilizing the thermal gradient.

As the ions transference occurs inside the cell; the balancing electrons are transferred in the external circuit. An electrical circuit can be modelled to account all the electrical resistances present in the circuit. And the resistance imparted by the ionic transport is referred to as mass transfer resistance "R_{MT}". Simultaneously, Ohmic resistance "R_{OHM}" and charge-transfer resistance "R_{CT}" account for the electrolyte resistance and the interface resistance between electrolyte and electrode, respectively (Ali H Kazim & Cola, 2016; Salazar, Stephens, et al., 2014). Recently, it was shown that in composite electrolyte solutions the R_{CT} and R_{OHM} is significantly less as compared to the pristine electrolyte solution. This emerges mainly because of increased electrical conductivity of the solutions and improved contact between the electrode/electrolyte interface because of the additives (Ali H Kazim & Cola, 2016).

With respect to the practical applications, as issue associated with the liquid electrolytes is the leakage of the electrolyte. For example, a thermocell attached to an automobile engine to harvest the waste heat into electricity will be subjected to continuous vibrations. A slight wear on the thermocell body causing electrolyte leakage can halt the cell operation. Therefore, “quasi-solid state” electrolytes are a better choice as the electrolyte. Moreover, these quasi-solid-state electrolytes can also provide low thermal conductivity further improving the cell performance. The concept of quasi solid state materials is to trap a conductive liquid electrolyte in a polymer matrix. In such a system, stable mechanical properties can be achieved while maintaining the lower thermal conductivity and higher Seebeck coefficients of liquids. The very first report presenting the solid electrolyte prepared the two gel electrolyte samples containing ferri/ferrocyanide and ferric/ferrous chloride in PVA matrix. The ferri/ferrocyanide behaved as n-type material resulting in -1.2 mVK^{-1} and ferric/ferrous chloride exhibited p-type material with 1.02 mVK-1. These gels were connected in series to obtain higher cell potentials, however, the power outputs were not significant but this study enlightens the possible applications of flexible thermocells in wearable applications. Quasi-solid-state electrolytes have been prepared by using PVA, Agar-Agar, cellulose and poly(sodium acrylate) beads, although the generated power with poly(sodium acrylate) is only 1.6 mWm^{-2}. In a separate study, cellulose matrix is used to trap $[Fe(CN)_6]^{3-/4-}$ redox couple forming a gel. The power density of pure liquid was still higher than the gel and the power density was further decreased as the cellulose composition was increased. This happens because in high concentrations of the cellulose, the channels within the gel are narrowed down limiting the mass transfer within the gel.

Amongst other aqueous electrolytes are KBr/Br_2 (S_e=5.68 mV/K) and NaCl (S_e=3.7 mV/K). Aqueous solutions are ideal base electrolytes as they have very low viscosity and very high ionic diffusion rate but the high volatility limits the application of the aqueous solutions. Inspired by the idea to explore organic electrochemistry, Bonetti in 2011 studied thermo-electrochemical seebeck of tetraalkylammonium macroions in organic solvents such as octanol, dodecanol and ethylene-glycol(Bonetti, Nakamae, Roger, & Guenoun, 2011). In particular, their combination of 1-dodecanol with 0.1 M concentration of tetrabutylammonium yielded S_e of 7 mV/K. In the case of the molten salt electrolytes, LiCl + KCl have been studied in the past, however, high melting temperature of the salts, impose some negative aspects with respect to electrodes including embrittlement (Gunawan et al., 2013). A range of ILs have been identified for S_e performance such as 1-ethyl-3-methylimidazolium tetraflouroborate (S_e=0.26 mV/K), 1-ethyl-3methylimidazolium-tris(pentafluoroethyl)trifluorophosphate (S_e=1.88 mV/K), 1-ethyl-3-methylimidazolium-bis(trifluoromethanesulfonyl)amide (S_e=1.64 mV/K), 1-ethyl-3-methyl-tetracyanoborate (S_e=1.55 mV/K) are some to mention. Whilst the highest S_e (2.19 mV/K) was recorded with the high temperature organic solvent 3-methoxypropionitrile (MPN) (Bonetti et al., 2011). Thus far inorganic redox couple e.g. $Fe(CN)_6^{3-}/Fe(CN)_6^{4-}$ and (I^-/I_3^-) were mixed with ILs for TEC applications, however, V. Zinovyeva et al have reported thermocell with thiolate/disulfide based organic redox couple with open-circuit voltage ranging from 1 – 5 mV at a temperature gradient of 8 K (Zinovyeva et al., 2014). Another organic redox couple tested for thermocell applications is Cobalt based redox couples like Cobalt bipyridyl [$Co^{II/III}$tris(bipyridyl)(NTf_2)$_{2/3}$]. The advantage of [$Co^{II/III}$tris(bipyridyl)(NTf_2)$_{2/3}$] over other inorganic redox couples is higher Seebeck coefficients.

2.2 Redox Couples

Thermocells depend heavily on the free electrons produced/consumed during the oxidation/reduction reaction of the redox couple. The molar entropy change between the redox species and the electrodes originated by the different temperatures of the electrodes generates a potential difference across the electrodes i.e. open-circuit voltage. The magnitude of the entropy change of a redox couple is influenced primarily by the structural changes in the redox species e.g. spin-crossover, effects from their solvent shells and chemistry between the redox couple and the solvent. Likewise solid thermoelectric materials, the entropy change of the redox couple (i.e. the Seebeck coefficient) can be either positive of negative depending on the difference of absolute charges of the reduced and oxidized species – giving a positive sign if the charge number of the oxidized species is larger.

Although, a wide range of redox couples have been identified but ferri/ferrocyanide ($Fe(CN)_6^{3-}/Fe(CN)_6^{4-}$) and iodide/triiodide ($I^-/I_3^-$) have highest Seebeck coefficient of -1.4 mVK^{-1} and 0.53 mVK^{-1} (in aqueous), respectively (Abraham et al., 2011; Hu et al., 2010). Thus $Fe(CN)_6^{3-}/Fe(CN)_6^{4-}$ is the archetypical couple for thermocell applications whereas I^-/I_3^- provides a wide scope of Seebeck coefficient improvement ranging from 0.53 ~ 0.97 mV K^{-1} depending upon the concentration of the redox couple in the solvent. Unlike $Fe(CN)_6^{3-}/Fe(CN)_6^{4-}$, the Seebeck coefficient of the I^-/I_3^- results in the positive value. It has been established throughout the literature that the magnitude of the Seebeck coefficient is highest with diluted electrolytes i.e. having particularly low redox concentrations, however, the power generation characteristics of a thermocell demands higher redox concentrations(Uhl et al., 2014). The Seebeck coefficient of the $Fe(CN)_6^{3-}/Fe(CN)_6^{4-}$ and I^-/I_3^- mainly depends on the solvent reorganization entropy. However, Cobalt base redox couples i.e. $Co^{2+/3+}(bpy)_3(NTf_2)_{2/3}$ have exhibited highest Seebeck coefficient of 2.19 mVK-1 in 0.01 M concentrated 3-methoxypropionitrile (MPN) owing to an additional electron add-up phenomenon known as spin-crossover i.e. the change in the spin state of $Co^{2+/3+}$ during simultaneous oxidation and reduction(He et al., 2016; Lazar et al., 2016). Although a single redox couple suffices the requirement to complete the electron transfer between the electrodes and electrolyte but L. Aldous and coworkers explored the possibility to merge the ferrocene/ferrocenium (Fc/Fc^+) and iodide/triiodide. The electrochemical Seebeck of ferrocenium triiodides $[Fe][I_3]$ by mixing the two redox couples aqueous solutions and some ILs was studied. The Seebeck coefficient of pristine redox couples were very low as for Fc/Fc^+ it was 0.1 mVK^{-1} and for I^-/I_3^- was 0.057 mVK^{-1} but mixing the two redox couples had an increasing effect on the Seebeck coefficient (FcI3; 0.81 mVK-1). The linearity between Voc (open circuit voltage) and ΔT (thermal gradient) in $[Fe][I_3]$ solutions was lost owing to the unstoppable reactions, however the power generation in $[Fe][I_3]$ was significantly higher than the Fc/Fc^+ redox solutions (Anari et al., 2016). The highest Seebeck value they obtained was 1.67 mVK^{-1} with the mixture of 1,1`dibutanoylferrocene and I_2. In this case it may be highlighted that the methodology for the Seebeck evaluation was not the conventional 2-beaker arrangement. In a conventional way, two beakers are maintained at different temperatures and open-circuit voltage is noted. In a systematic way, many open-circuit voltages are noted at increased thermal gradient and the Seebeck coefficient is taken as the slope between the open-circuit voltage-thermal gradient linear plot. However, those authors took the maximum cell potential (a single value) at load conditions (that is also the open-circuit voltage) and divided it with the thermal gradient – this may not be a very accurate method for Seebeck evaluation.

In addition to the mentioned inorganic redox couples, organic counterparts e.g. thiolate/disulphide ($McMT^-/BMT$) have also been studied and resulted in competitive Seebeck of -0.6 mVK^{-1}. The advantage of the organic redox couples over inorganic is the minimization of the corrosive effect on the electrode surface as for example the I/I_3^- has a very corrosive behavior(Zinovyeva et al., 2014). As a slight deviation with the thermocell definition where electrodes are mainly electron pathways rather than electron generators, are the $Cu^{2+}/Cu_{(s)}$ electrode systems. In such a system solid copper is used as electrodes with $CuSO_4$ as an electrolyte. While maintaining the electrodes at different temperatures the anode gets oxidized releasing electrons to the electrolyte producing C^{2+} ions. These ions are transferred to the cathode where reduction occurs and the additional electrons are utilized for energy generation purposes. Thus, these systems cannot operate continuously as the anode will ultimately be consumed marking a limitation for the practical implementation of such systems (Gunawan et al., 2014; Gunawan et al., 2013). Although, the Seebeck value produced with 0.7 M $CuSO_4$ resulted in a competitive value of 0.84 mVK^{-1}.

Finally there have been some reports mentioned extra-ordinary high Seebeck values of ~7 mVK^{-1} in organic solvents (as highlighted in section 2.1). Interestingly, these organic electrolytes do not contain any redox couple, thus the rise of Seebeck effect in such electrolytes are not based on the change in molar entropies of reduced or oxidized species rather it is originated as the Soret effect. When the thermal gradient is applied across the electrodes, it brings a slight change in the concentration of the solution. This concentration gradient causes the ionic transfer between the respective electrodes and this phenomenon is referred to as Soret effect. In the presence of the redox couple the Soret effect is mainly neglected as the change in entropies is the predominating driving force. The side effect of the thermocells prepared without redox couples is that upon connecting them in load conditions the power outputs are not so high owing to the abundance of electrons generated at the electrode surface.

2.3 Electrode Materials

Electrodes play a crucial role in the performance of thermocells. The electron generated through the redox reaction has to be transmitted to the electronic circuit through the electrode materials. Furthermore, the electrochemical potential equilibrium between the electrodes and the redox couple is another important aspect of electrodes' role. Since the redox reactions are extremely oxidative in nature the commonly available electrodes like Copper, Nickel, or Aluminium are unsuitable for thermocell applications. Therefore, Platinum (Pt), Glassy carbon, Carbon and Graphite are ordinary electrode materials (Im et al., 2016; Qian, Cao, Xie, & Dong, 2016; Romano et al., 2013; Romano, Razal, Antiohos, Wallace, & Chen, 2015; Salazar, Kumar, & Cola, 2012). However, quantum confinement in nanomaterials has resulted in appreciable results. CNTs which are well-known for efficient electron transfer were used as electrode materials by R. Hu and coworkers demonstrated appreciably high power output of 1.8 $W.m^{-2}$ with Carnot efficiency of 1.4% (Hu et al., 2010). Single walled CNTs-coated-Carbon electrodes were tested to harvest body heat into electricity through thermocell utilizing ferri/ferrocyanide by H. Im et al. They have reported the open-circuit voltage of 20 mV at 15 K with the maximum power density of 0.46 $mW.m^{-2}$ (Im et al., 2014). Since issues of toxicity and high cost encircle both Pt and CNTs, Abraham et al conducted a survey exploring various economic and efficient electrode materials. Keeping Pt and Stainless Steel (SS) as the main competitors, they prepared platinized (Pt deposited) and Poly (3,4 ethylenedioxythiophene) PEDOT coated Pt and SS electrodes. Owing to the low catalytic activity of SS, its performance was not appreciable; however, Platinized SS and PEDOT-SS exhibited the power density of 188 mWm^{-2} and 179 mWm^{-2} which is quite close to solid Pt electrodes (183 $mW.m^{-2}$). Thus, electro-catalytic coatings on SS can significantly reduce the device cost, preserve the performance and render TECs more eco-friendly (Abraham et al., 2014).

Carbon based materials like CNTs, Graphene, Graphene oxide, and Reduced Graphene Oxide (RGO) have been studied for thermocell applications. Furthermore Nitrogen doped and Boron doped CNTs have also been explored. However, a study worthy of discussion is that of aerogel CNT electrodes reported in. In this study firstly CNTs are prepared in the form of porous aerogel structures. The power output with the Aerogel CNTs after annealing 15 minutes at ΔT of 50 K was 3.8 $W.m^{-2}$ with the corresponding efficiency of 2.3%. The power density was further extended to 5.5 Wm^{-2} with 3.6% efficiency by depositing Pt nanoparticles on the Aerogel CNTs (Im et al., 2016). However, the highest efficiency of 3.95% was achieved by compressing the Pt-deposited Aerogel CNTs generating maximum power density of 6.6 Wm^{-2}. All of the above discussed literature has the common factor that the thermal gradient between the electrodes was the only driving force which generates electron between Anode and Cathode. H. Zhou et al presented the concept of “Host-Guest Complexation” where iodine ion gets absorbed in the complex ionic structure of the electrolyte in the cold electrode area but the iodine ions leave the electrolyte structure when heated at the hot electrode. This free iodine ion absorbs the electron from anode travels to the cathode (cold electrode) leaves the electron and gets absorbed in the electrolyte. In this cycle, the driving force is not the thermal gradient alone. The absorption of the iodine in electrolyte at cold electrode creates a concentration gradient in the iodine composition in the overall solution. This concentration gradient is a supplement to the thermal gradient improving the maximum power density (Zhou et al., 2016).

2.4 Thermocell Design Parameters

In thermocells, thermodynamics, electro-kinetics, and fluid dynamics all have significant contributions. Currently efforts to scale down the size of TEC modules from millimetre to several microns are under way. Stefanie Uhl et al have fabricated micro-sized thermocells by Solid-on-Liquid deposition technique. This technique allowed efficient encapsulation of liquid between electrodes. Various ILs with (I^-/I_3^-) redox couple were studied exhibiting different Seebeck values ranging from -0.044 ~ 0.851 mV/K (Uhl et al., 2014). Every slight change in the physical features of the thermocells bring a notable change in thermocell performance. For example, if the electrode to electrode separation is too high the electrolytic ohmic resistance will become so high that the power will be reduced. Similarly, if the electrodes are brought to closer even than the power density will be reduced as the thermal gradient will be diminished. Hence optimization is required in every aspect of the design parameters.

Cell orientation, heating direction, electrolyte volume and electrode separation can significantly influence the cell performance. There are mainly three heating orientations (i) cold-above-hot arrangement where heating is carried out at the bottom, (ii) hot-above-cold configuration which is opposite to the former where heat is provided from the top electrode and finally (iii) the horizontal assembly where heat travels from hotter to colder electrode in a horizontal direction as shown in Figure 2.1 (Quickenden & Mua, 1995). Generally, the hot-above-cold arrangement has lower performance as compared to other two as the direction of the natural flow of ions contradicts with the heat direction. Thermal diffusion and convection are the two modes of ionic movement within the cell out of which the later has a dominating contribution. Natural convection within the electrolyte happens due to the temperature-dependent density of the electrolyte. Considering the cold-above-hot configuration, the electrolyte closer to the hot electrode has low density and naturally tends to move upwards. Once it gets cooled at cathode, the density is increased and the electrolyte flows down. In this way, convectional cycles are continued in the cell. However, in hot-above-cold arrangement the electrolyte after absorbing heat from the top electrode naturally stays at top, thus the electron transfer from anode to cathode is not very effective and the power outputs are suppressed.

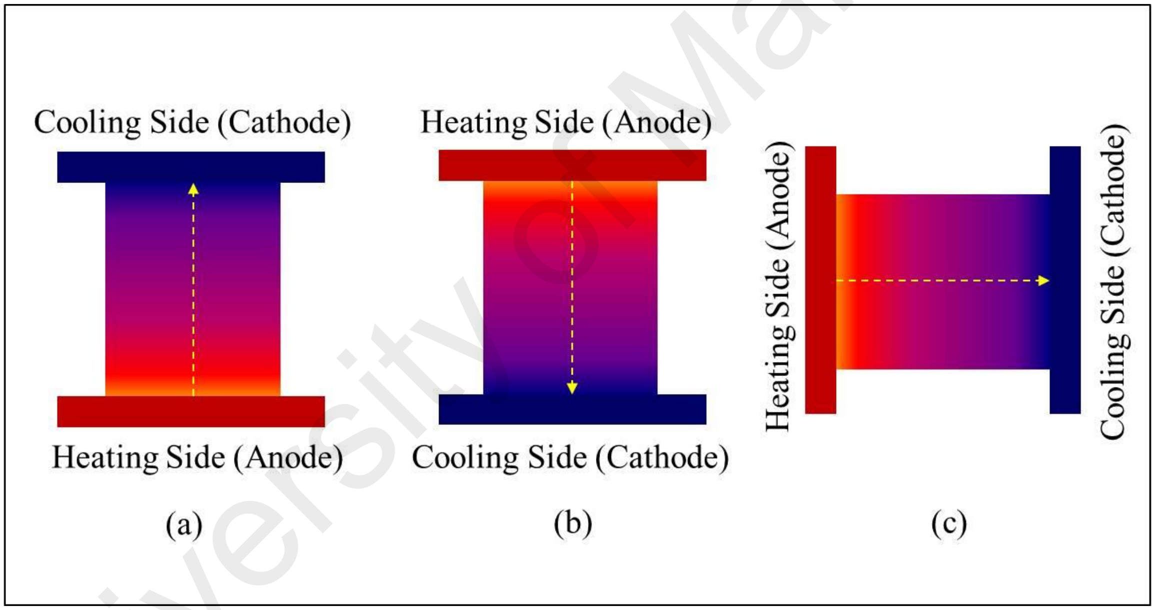

Figure 2.1: TEC orientations based on heating direction (a) Cold-above-Hot configuration where cooling side is at the top and heating is done from the bottom (b) Hot-above-Cold configuration in which heat is supplied from the top while keeping the bottom electrode at lower temperature and (c) Vertical configuration where the two electrodes are vertically placed and heating is done from either of the sides.

The performance of the cell is dependent on many mass transport properties namely Ionic diffusion, migration, thermodiffusion (Soret effect) and natural convection. In the absence of natural convection, the mass transfer and electron exchange process at the respective electrodes will not be homogenous i.e. (when there is no convection) Soret effect will produce excessive concentration species at respective electrodes and the cell performance shall decay over time. Furthermore, diffusion at colder electrode is slightly sluggish as the density is higher further contributing in the performance decay. By incorporating natural convection, homogenous ionic transfer and electron exchange is achieved and power can be improved as high as 88%. However, increasing convection simultaneously increases the heat flow within the cell. Therefore, a larger input energy is desired to maintain the cell at particular thermal gradient which decreases the cell efficiency.

The electrode-to-electrode separation has also a significant influence on the cell performance. But it is highly subjective on the electrolyte properties e.g. thermal conductivity and ionic diffusion. For ferri/ferrocyanides, increasing the electrode separation decreases the power outputs. However, Gunawan at el has shown the increment of maximum output power density from 0.8 to 1.6 μWcm^{-2} of Cu/Cu^{2+} thermocells by increasing the electrode separation from 46 mm to 100 mm. This enhancement is based on enhancing the Nusselt number (Nu), Sherwood number (Sh), and Lewis number (Le). These fluid transport coefficients define the nature of the flow on the basis of fluid density, kinematic viscosity, thermal diffusivity, ionic diffusion, gravitational forces and the length of the conduit. They have optimized Nu, Sh and Le by controlling the length of the ionic diffusion path i.e. the separation between the two electrodes (Gunawan et al., 2014). For I^-/I_3^- systems, as shall be discussed in the following sections, optimum electrode separation is desired. The separation of 20 mm (keeping the diameter 15 mm) resulted in optimized performance as compared to the two cases when the separation is either too small (i.e. 10 mm) or too long (i.e. 30 mm).

2.5 Applications of Membranes in conventional batteries and redox flow cells

Although, the role of membranes has not been investigated for thermocells before our work; however, porous membranes have been widely used for conventional batteries and other electrochemical systems like fuel cells and redox flow batteries. Herein, a brief literature review regarding the preferred materials (for batteries, fuel cells and redox flow cells) is presented.

There are diverse properties desired in membrane materials for the successful implementation in batteries for example flexibility, permeability, shut down, porosity, resistance to thermal and chemical degradation, wettability, dimensional stability, mechanical stability and cost. For batteries, polymers, polymer composites and blends are preferred. The most commonly used polymers are polyethylene (PE), polypropylene (PP), poly(ethylene oxide) (PEO), poly(acrylonitrile) (PAN), and poly(vinylidene fluoride) (PVDF) and its copolymers. In order to modify the surface properties like hydrophobicity, hydrophilicity and porosity filler materials are added in the main polymer solution before film fabrication. Most commonly used fillers are SiO_2, Al_2O_3, TiO_2, $BaTiO_3$ and carbonaceous fillers. These fillers also contribute to optimize the ionic conductivity and the mechanical strength of the membranes. A membrane is needed in the batteries to ensure a separation between the respective membranes and simultaneously providing a path flow for the charged ions between the electrodes. A relatively newer strategy is to prepare heterogeneous composite structures e.g. a sandwiched structure separators of PVDF-co-hexafluoropropylene (PVDF-HFP), sandwiched poly(m-phenylene isophthalamide)

(PMIA) between two PVDF layers (PVDF/PMIA/PVDF) and sandwiched PVDF layer between two poly(phthalazinone ether sulfone ketone) (PPESK) (PPESK/PVDF/PPESK) have been studied for Li-ion batteries (Lu et al., 2013; Zhai et al., 2014). The results show improved electrochemical performance of the heterogeneous membranes over the blends.

2.6 Conclusions

The ideal electrolyte materials for the thermo-electrochemical application should have some trade-off properties, i.e. lit should be lesser in viscosity while it should also be highly thermal resistive. Furthermore, it should have higher ionic conductivity, electrochemical Seebeck and diffusion coefficients. Another important factor is the ability to dissolve the redox couple, because without the redox couple the energy harvesting will not be practical. The electrolyte should have wider electrochemical window with high thermal and chemical stability to ensure long-term thermocell applications. For electrodes, carbon nanomaterials have brought remarkable improvements in the overall efficiency. In principal, the electrodes should have higher electron affinity with chemical stable nature. If the electrode is not chemically stable the corrosion of the electrode surface will ultimately stop the cell power generation.In terms of thermocell architecture, it is a vast area to optimize depending upon the electrolyte and the redox couple used. For particular fluids optimized electrode-to-electrode separation may differ which should be identified subjectively. The heating regime should be cold-above-hot configuration because in that case the density flow is parallel to the flow of ions, improving the electron transfer at the electrode surface.

CHAPTER 3:

THE ROLE OF ELECTROLYTE FLUIDITY ON THE POWER GENERATION CHARACTERISTICS OF THERMALLY DRIVEN ELECTROCHEMICAL CELLS

3.1 Introduction

Thermally driven electrochemical cells (thermocells) are capable of harvesting thermal energy into electricity. The thermal gradient (i.e. heat input for thermocells) can be attained from industrial engines, automobiles, solar radiations or even human bodies. Thermocells convert the applied thermal gradient into potential gradient by the virtue of thermoelectric effect of the electrolyte solution. The thermoelectric effect in solid-state materials (Bi_2Te_3 and Sb_2Te_3 etc) can also transform thermal energy into electricity, however, toxic nature of the materials, high fabrication cost and low figure of merit (ZT) gives superiority to thermocells. The Seebeck coefficients , (i.e. the voltage generated per degree Kelvin)of the electrolyte solutions generally lie in mVK^{-1} scale (as mentioned in section 2.1) while the state-of-the-art solid state thermoelectric materials is limited to 200 – 250 μVK^{-1} (Hasan et al., 2013; Hwang et al., 2015). The Seebeck coefficient for the redox based electrolyte can be defined by the following equation:

$$Se = \frac{\partial \mathrm{E(T)}}{\partial \mathrm{T}} \tag{3.1}$$

which can further be simplified as:

$$Se = \frac{\Delta Src}{\mathrm{nF}} \tag{3.2}$$

where E(T) is the electrode potential of the electrode in the electrolyte, T is the absolute temperature, n is the number of electrons transferred during the reduction-oxidation reaction, F is the Faraday’s constant and ΔS_{rc} is the entropy change of the redox couple in the electrolyte at the electrode surface. The change in the entropy emerges because the equilibrium potential of the redox couple varies at the electrode surface depending upon the electrode temperature (He et al., 2016).

Another factor influencing the entropy change of the redox couple is the medium or the liquid in which the redox couple is dissolved i.e. a redox couple shows different Seebeck coefficient at same concentration in different liquids. Therefore, the thermo-physical properties of the medium electrolyte are equally significant to the thermocell performance as compared to the redox couple itself. For thermoelectric characterization ionic conductivity, ionic diffusion, and thermal conductivity of the electrolyte solution are important properties besides the Seebeck coefficient.

As the general rule, the ideal electrolyte for thermocell application should have high ionic conductivity, diffusion coefficient, wider electrochemical window, and thermal stability(Abraham, MacFarlane, & Pringle, 2013). Nonetheless, thermal conductivity is a crucial thermo-physical property of the electrolyte which has a significant share in the overall performance of the thermocell. Higher thermal conductivity refers to convenient heat transport within the electrolyte (from hot to cold electrode) which implicates an unstable and reduced temperature gradient across the electrodes (Salazar, Stephens, et al., 2014). Therefore, an electrolyte with intrinsically lower thermal conductivity favors the thermocell applications as the heat flow across the electrodes is minimized; enabling improved ∆T. A recent development in thermocell research is to include additives such as MWCNTs (Salazar, Stephens, et al., 2014) or PEDOT:PSS (Ali H Kazim & Cola, 2016) in the electrolyte. It was reported that MWCNT dispersed in the electrolyte reduces the mass transfer resistance which has the effect of increasing the power density of the composite electrolyte. It is noteworthy that the addition of the MWCNT (from *0* to *0.3* wt%) has not affected the thermal conductivity of the electrolyte; thus permitting the improvement in the overall performance (Salazar, Stephens, et al., 2014).

Alternatively, composite solutions have also been explored in which ILs are mixed with various organic solvents such as methanol, polycarbonate (PC), dimethyl sulfoxide (DMSO), 3-methoxypropionitrile (MPN) or acetonitrile (ACN). There have been many publications appreciating the composite electrolytes for thermocell performance. For an instance, V. Zinovyeva et al showed that the electrochemical Seebeck and the open-circuit voltage for the mixture of acetonitrile and 1-ethyl-3-methylimidazolim tetrafluoroborate is higher than the acetonitrile alone(Zinovyeva et al., 2014). Similar trend was observed by M. A. Lazar et al upon mixing MPN and DMSO in the IL i.e. the performance of the mixture was found better than the solvent or IL alone (Lazar et al., 2016). J. He et al also noticed that the mixing ILs with polycarbonate (PC), improves the power outputs of the mixture as compared to the pure ILs, however, the highest power density was achieved for the pure PC (He et al., 2016). As a general understanding, the organic solvents like PC, DMSO, or MPN reduces the viscosity and increases the diffusion coefficient in the electrolytes resulting in higher power density. In all of the above discussed composite electrolytes the thermocell performance is improved as compared to the pure IL, however, (1) the impact of the organic solvent on the thermal conductivity of the IL and (2) the overall role of thermal conductivity of the mixture on the thermocell performance has not been elaborated.

The motivation of this chapter is to highlight the significance of thermal conductivity of the composite electrolytes. The composite electrolyte is prepared by mixing an organic solvent (i.e. Acetonitrile) in the ionic liquid (i.e. 1-Ethyl-3-Methylimidazolium Ethylsulfate). The hypothesis is that if the thermal conductivity of the composite electrolyte is higher than the pure ionic liquid, it can deteriorate the power density even if other thermo-physical parameters are improved.

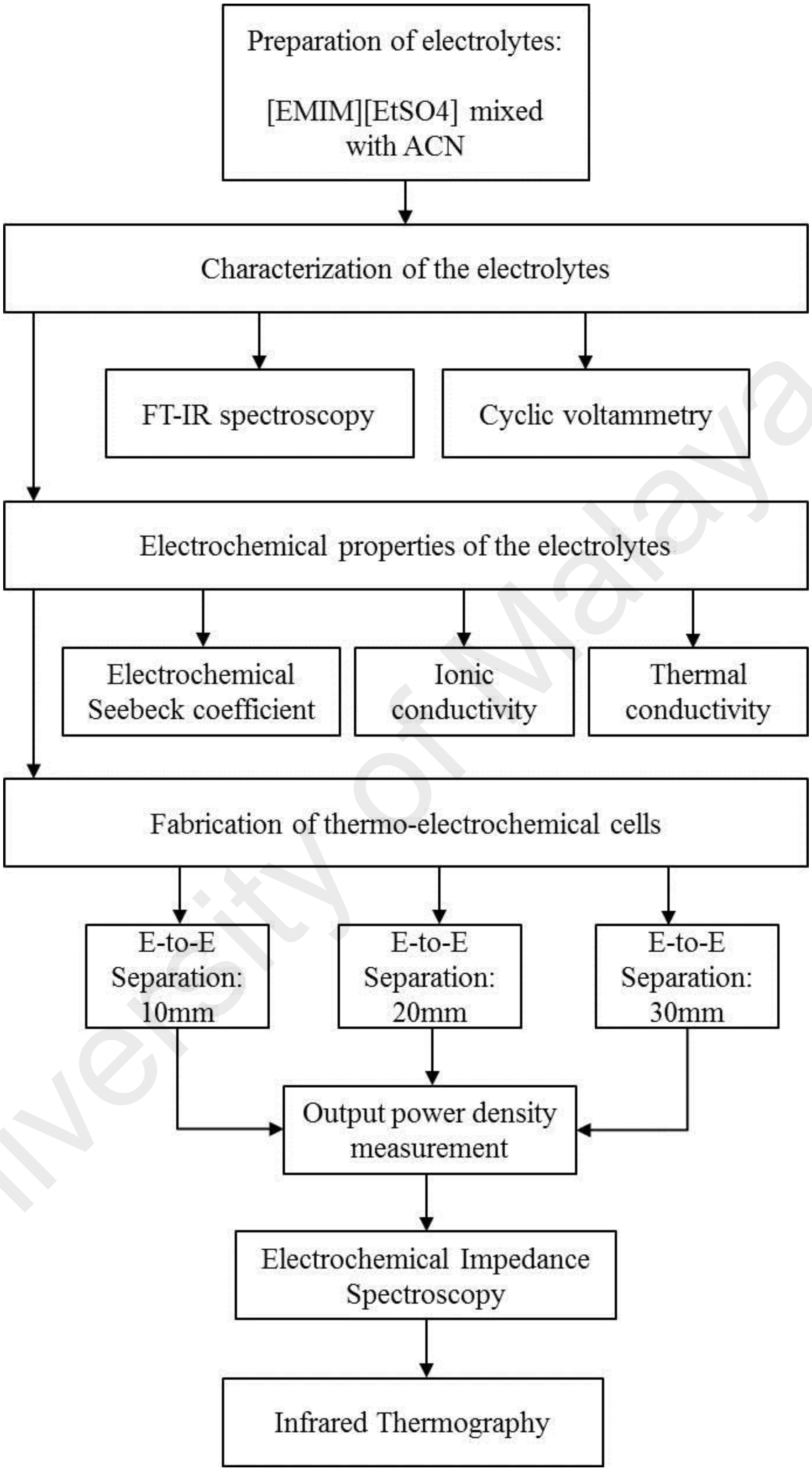

Figure 3.1: Flowchart of the experimental methodology and results

3.2 Methodology

1-Ethyl-3-Methylimidazolium Ethylsulfate ([EMIM][EtSO$_4$]) was purchased from MERCK. Iodide/triiodide (I^-/I_3^-) redox solution was prepared by Iodine (≥ *99.8*%) and Potassium Iodide (≥ *99.5*%) in *1:2* compositions. Iodide/triiodide redox couple was added in ([EMIM][EtSO$_4$]) and heated upto *100* ˚C under magnetic stirring for *1* hour. Anhydrous Acetonitrile (≥ *99.8*%), purchased from Sigma Aldrich, was used as a solvent at various compositions (*0.002, 0.004,* and *0.010* mol) in prepared [EMIM][EtSO$_4$] solution. The mixture was heated upto *120* ˚C for *24* hours to ensure homogeneity. The infrared (IR) spectrum of the electrolytes was recorded in the range of *450* to *4000* cm^{-1}.

Since the electrochemical Seebeck is the materials' property the standard approach to determine the S_e is a two-beaker experiment. Electrochemical Seebeck coefficient (S_e) was evaluated by the slope of linear curves between $V_{oc} - \Delta T$. The power characteristics of the thermocell containing [EMIM][EtSO$_4$] and ACN-diluted-[EMIM][EtSO$_4$] was studied in *13* mm diameter while the length of the cell (i.e. electrode-to-electrode separation) was varied to *10, 20* and *30* mm. Once the desired ΔT was achieved the electrodes were connected to a variable resistor box Elenco RS-500 to apply external loads (R; Ω). The cell potential (V) across the electrodes was measured by Agilent 34461A 61/2 digital multimeter and power ($P=V^2/R$) was calculated by ohm's law as described in literature. The infrared thermal imaging was carried out by R300SR-HB (Nippon Avionics Co. Ltd.). The graphite and Pt rods were used as electrode materials in thermocell and 2-beaker experiments, respectively. The systematic flowchart of the experimental procedures and the results is shown in Figure 3.1.

3.3 Results

The chemical structure of the ionic liquid i.e. [EMIM][EtSO$_4$] and the polar solvent i.e. Acetonitrile is shown in Figure 3.2 (a). The bulky cation of the ionic liquid i.e. [EMIM]$^+$ is attached with the anion i.e. [SO$_4$]$^-$ by the weak interatomic forces. The IR spectrum of the pure [EMIM][EtSO$_4$] as shown in the Figure 3.2(b) matches well with the literature (Dhumal, Kim, & Kiefer, 2011). Generally, the IR spectrum of any molecule is segregated into low and high frequency regions. The stronger bond vibrations like C−H stretching are observed from *3150* to *2900* cm^{-1}. These stretching modes are associated with the aromatic imidazolium ring of the cation of [EMIM][EtSO$_4$]. The band observed at 3102.51 cm^{-1} is the characteristic of the [EMIM]$^+$ cation representing vibrational stretching mode between C−H.

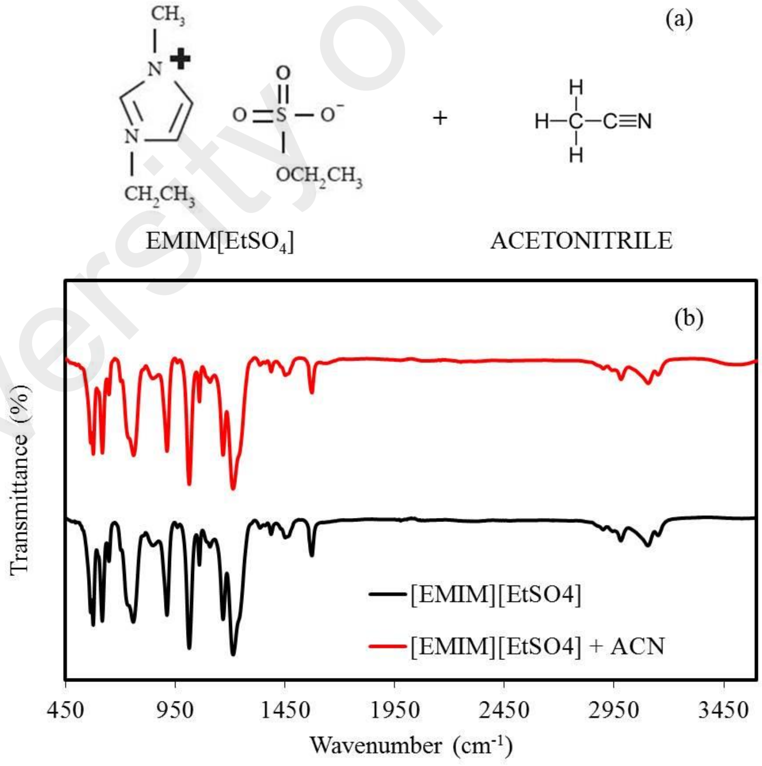

Figure 3.2: (a) The chemical structure of [EMIM][EtSO$_4$] and ACN (b) FT-IR spectrum of [EMIM][ETSO$_4$] and ACN-diluted-[EMIM][ETSO$_4$]

The IR traces of N-C-H rocking appear in the lower frequency region at *1572.28* and *1337.15* cm^{-1}. For the anion i.e. $[EtSO_4]^-$, the characteristic peak is at *912.67* cm^{-1} representing the O-S-O symmetrical stretching. Another band to be noted for the anion is at 757.13 cm^{-1} which is attributed to the wagging of C-C-H. It is notable that the IR spectrum does not show any significant alteration by the addition of ACN. However, there is a minute shift for the peaks at *3103.27* and *757.13* cm^{-1} to *3104.80* and *759.97* cm^{-1}, respectively by the effect of ACN. The organic solvent added in the base electrolyte generally amends the inter-atomic interactions within the molecular structure of the electrolyte and the phenomenon is referred as “solvent reorganization”. T. Kim et al studied the performance of methanol-added aqueous electrolyte in thermocells. They observed the FTIR peak (C≡N of $Fe(CN)_6^{4-}$ at *2044* cm^{-1}) broadening in the methanol-water electrolyte and related it with the rearrangement of the solvated molecules around $Fe(CN)_6^{4-}$ (Kim et al., 2017). This solvated rearrangement increases the overall entropy change and improves the electrochemical Seebeck (He et al., 2016; Kim et al., 2017; Lazar et al., 2016). Therefore, these peak shifts (i.e. from *3103.27* to *3104.80* cm^{-1} and *757.13* to *759.97* cm^{-1}) indicate weakening of these bonds reducing the electrolyte viscosity.

This improvement in solvent rearrangement can also be observed in electron transfer mechanism at electrode/electrolyte interface. The cyclic voltammetry of the electrolytes shown in Figure 3.3 explicitly indicates higher anodic/cathodic peak currents with diluted $[EMIM][EtSO_4]$. For the viscous electrolytes a thick boundary layer is produced at the surface of the electrode hindering the electron transfer from the electrolyte to electrode or vice versa, thus we observe the similar phenomenon with pure $[EMIM][EtSO_4]$ as it is intrinsically very viscous.

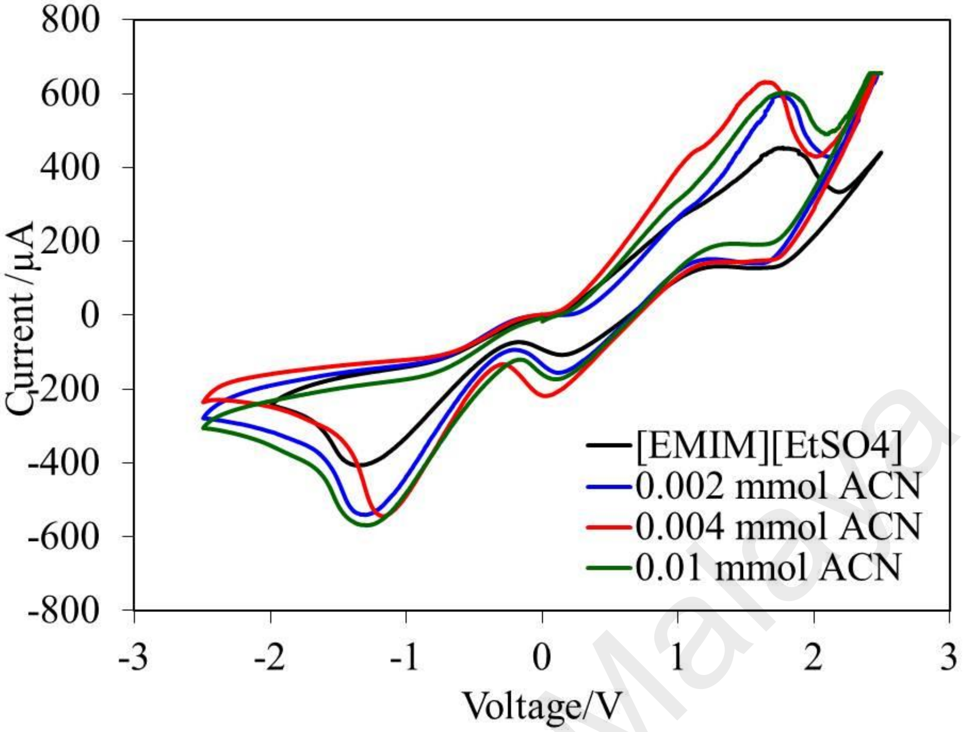

Figure 3.3: Cyclic Voltammetry of [EMIM][ETSO$_4$] and ACN-diluted-[EMIM][ETSO$_4$] samples

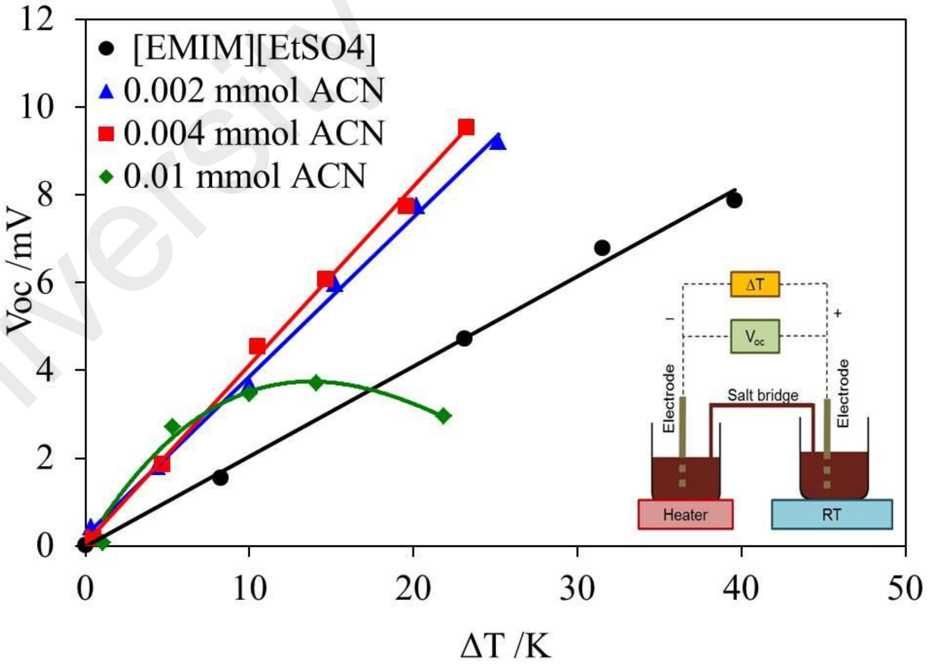

Figure 3.4: Electrochemical Seebeck Coefficient evaluation of [EMIM][ETSO$_4$] and ACN-diluted-[EMIM][ETSO$_4$] samples

Once ACN is added in the electrolyte, its fluidity is increased removing the boundary layer at the electrode surface; hence improving the electron transfer. Diluting the ionic liquids with organic solvents also has a direct impact on the diffusion coefficient (D, m^2s^{-1})(He et al., 2016; Lazar et al., 2016). The diffusion coefficient for [EMIM][$EtSO_4$] and ACN-diluted-[EMIM][$EtSO_4$] was calculated from Randles Sevick equation (as shown below) using the peak current from the cyclic voltammetry and represented in the Table 3.1.

$$D = \frac{I_L}{4\mathrm{nFCa}} \tag{3.3}$$

where I_L is the limiting current, n is the number of electrons involved in the reaction, F is the Faraday's constant, C is the concentration of the redox couple and a is the radius of the electrode. As expected, the diffusion coefficient has increased upon adding the ACN. As expected, the electrochemical Seebeck (S_e) has an increasing trend with respect to the addition of ACN. The impact of ACN on the electrochemical Seebeck (S_e) can be observed in Figure 3.4.

As the electrochemical Seebeck (S_e) defines the capability of the electrolyte to transform the applied thermal gradient into potential difference across the electrodes, Figure 3.4 shows that the S_e of the [EMIM][$EtSO_4$] raised from *207.2* μV/K to *416.4* μV/K upon the dilution with ACN. However, no significant difference was observed by changing the composition of ACN between *0.002* to *0.004* mol. Once the composition was increased to *0.01* mol, a non-linear relationship between the V_{oc} and ΔT was realized.

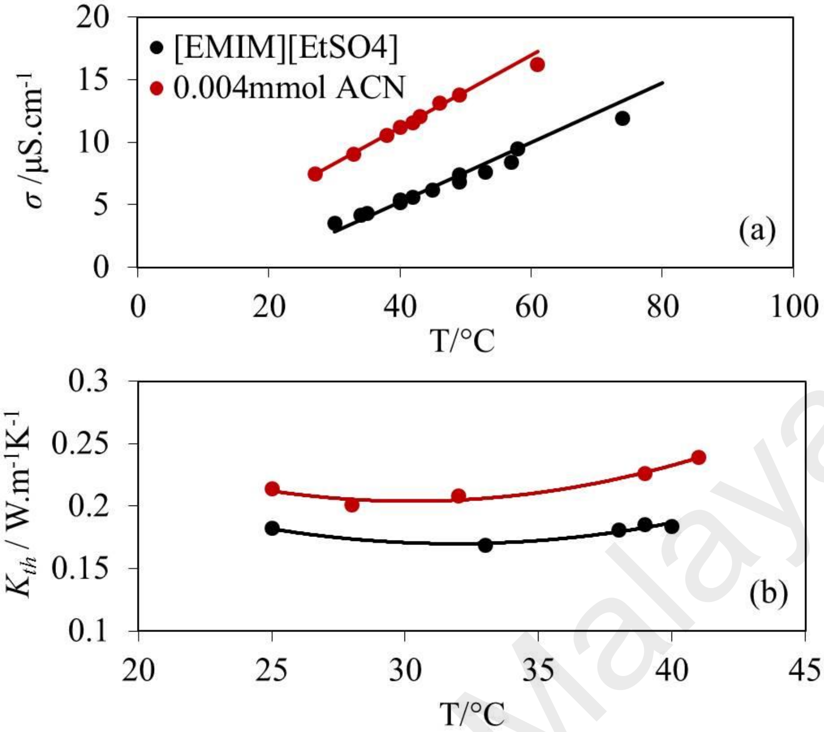

Figure 3.5: (a) Ionic and (b) Thermal conductivities of [EMIM][ETSO$_4$] and ACN-diluted-[EMIM][ETSO$_4$] samples

In addition to an improved electron transfer between the electrolyte and electrode another improvement incorporated by the dilution is observed in the ionic conductivity as shown in Figure 3.5(a). The ionic conductivity of the base [EMIM][EtSO$_4$] from *3.5* μS/cm is increased to *7.5* μS/cm at room temperature as the effect of dilution. The linear increment in the ionic conductivity of the electrolytes is also beneficial for thermocell characterization. In solid-state thermoelectrics, increment in electrical conductivity of the material is coupled with an increase in the thermal conductivity. Likewise, thermal conductivity of our samples has increased from *0.18* W.m^{-1}K^{-1} to *0.22* W.m^{-1}K^{-1} at room temperature. As the temperature is increased the thermal conductivity of both samples increases, nevertheless, it is higher for ACN-diluted-[EMIM][EtSO$_4$] samples as compared to the base [EMIM][EtSO$_4$] as shown in Figure 3.5(b). This indicates that the diluted electrolytes allow fast heat propagation without maintaining the desired thermal gradient.

Since the diluted [EMIM][EtSO$_4$] has higher thermal conductivity it is less viscous; escalating the convective flow within the cell. This not only reduces the thermal gradient but also reduces the power density.

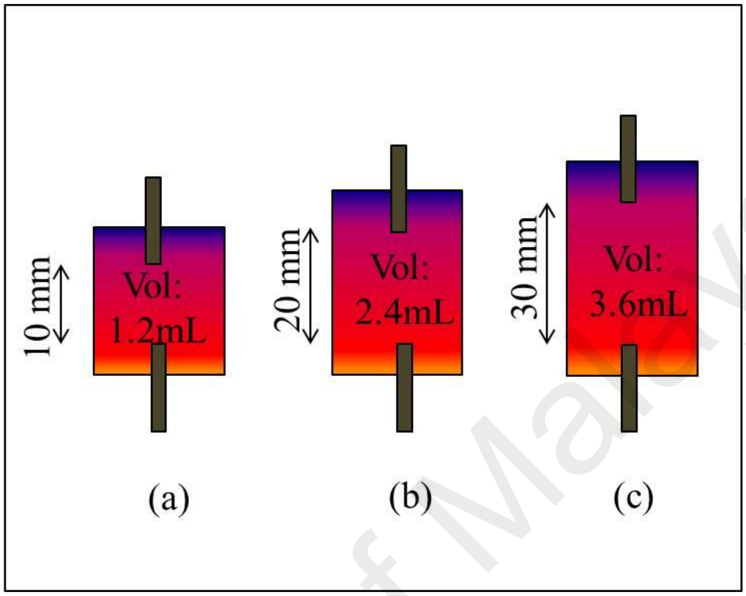

Figure 3.6: Cell configuration of TEC with variable electrode-to-electrode separations

The [EMIM][EtSO$_4$] and ACN-diluted-[EMIM][EtSO$_4$] electrolyte was taken in the thermocells with variable electrode-to-electrode (e-to-e) separation as shown in Figure 3.6. The Figure 3.7 shows the output power density of the thermocells with [EMIM][EtSO$_4$] electrolyte with e-to-e separation of 10, 20 and 30 mm. The maximum power density of ca. 6 nW.cm^{-2} is observed when the e-to-e separation is 10 mm which increases to ca. 12 nW.cm^{-2} upon increasing the e-to-e separation to 20 mm. Additionally, the maximum cell potential is also increased from 5.4 mV to 8.2 mV. The increasing e-to-e separation from 10 to 20 mm has two immediate impacts: (a) the volume of the redox electrolyte is increased from 1.2 to 2.4 mL as shown in Figure 3.6, therefore, the redox reactions taking place at the electrode surface has increased and (b) the thermal gradient maintained between the two vertical electrodes is improved (from 17 to 28K). Both of these factors result in the enhancement of the power density. However, upon any further increment in the e-to-e separation the power density is reduced to 1.1 nW.cm^{-2} owing to the increased ohmic resistance of the electrolyte with the excessive volume of 3.6 mL.

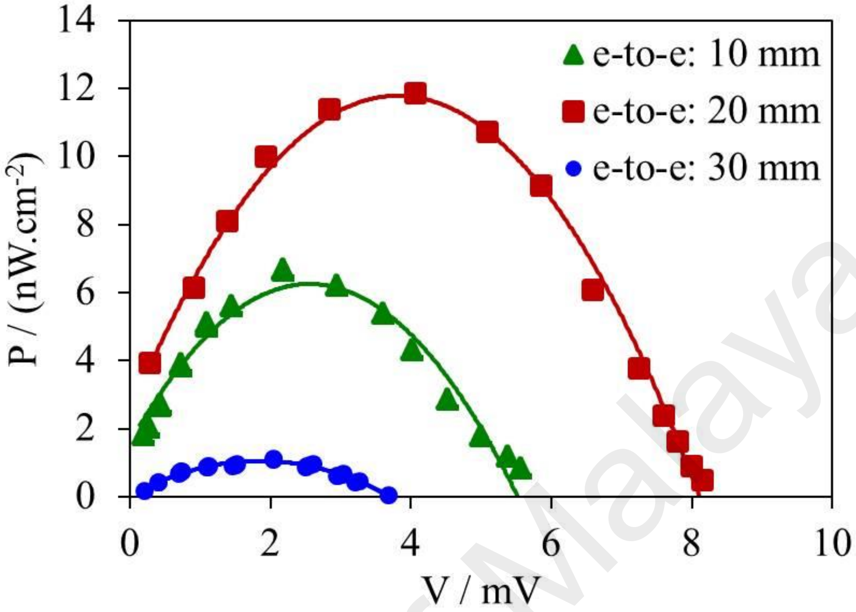

Figure 3.7: Power generation curves of TEC containing [EMIM][EtSO$_4$]

In order to diagnose the increasing Ohmic resistance of the cell with respect to the e-to-e separation, electrochemical impedance spectroscopy (EIS) is a useful characterization tool. The EIS data of the cells with variable e-to-e separations is represented as the Nyquist plot, shown in Figure 3.8. The real part of the impedance (Z’) is plotted on x-axis and imaginary part (Z’’) along y-axis. The starting point of every curve at Z’’=0 represents the ohmic resistance of the cell. The cell has the combination of resistive-capacitive behaviour expressing the kinetic and diffusion processes undergoing the thermocells during electron transfer. The cell with e-to-e separation of 10mm has the ohmic resistance of 40.15 Ω which is increased to 116.43 Ω in case of 30 mm e-to-e separation. Likewise, the charge transfer resistance is also maximum with the highest e-to-e separation. Thus, the increased ohmic resistance limits any further improvement in power density of the cell.

Similar experiments with the ACN-diluted-[EMIM][EtSO$_4$] electrolyte were carried out and the results are shown in Figure 3.9. It is noteworthy that in all of the cases of e-to-e separation the power density with ACN-diluted-[EMIM][EtSO$_4$] electrolyte is significantly smaller as compared to the base [EMIM][EtSO$_4$] electrolyte. This reduction is the indication of the increased thermal conductivity of the diluted electrolytes as discussed with respect to Figure 3.10.

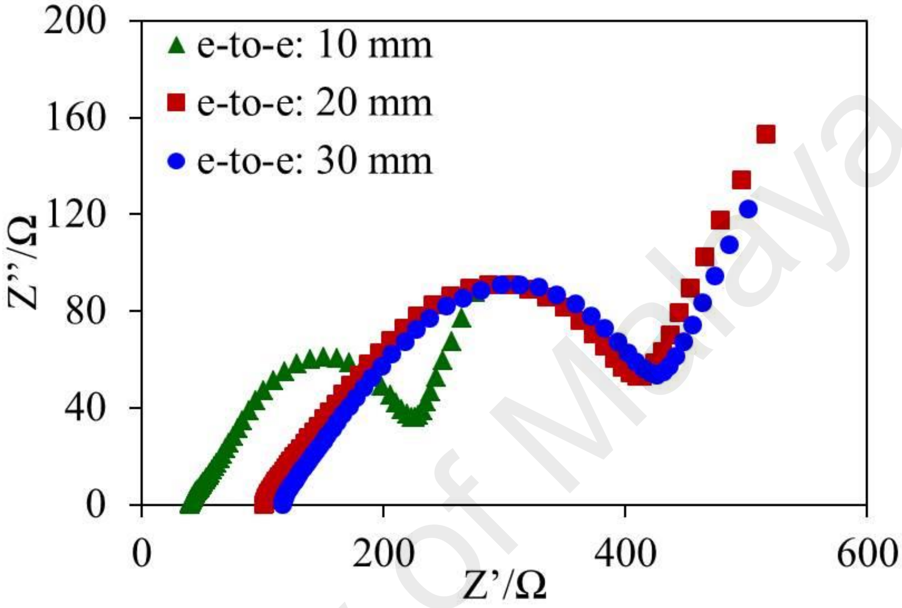

Figure 3.8: Electrochemical Impedance Spectroscopy of TEC containing [EMIM][EtSO$_4$]

The impact of the elevated thermal conductivity of the electrolyte is reflected in the power density curves as shown in Figure 3.10. The maximum power density of base [EMIM][EtSO$_4$] reaches around *118* μW.m^{-2} whereas the maximum power density for ACN-diluted-[EMIM][EtSO$_4$] is only *36* μW.m^{-2} owing to fast heat transfer. The actual temperature of the electrode surface can be evaluated by the expression $\Delta T_{act} = \Delta V / S_e$ whereas ΔV is the cell potential (taken from the Figure 3.10) whilst S_e is the electrochemical Seebeck (taken from Figure 3.4). Thus we can see that for the pure [EMIM][EtSO$_4$] sample the ΔT_{act} equals *37*°C, which is reasonably closer to the applied temperature gradient (ΔT_{app}) of *40* °C. We can attribute this to the lower fluidity of the [EMIM][EtSO$_4$] which allows lower mass and heat transfer across the cell.

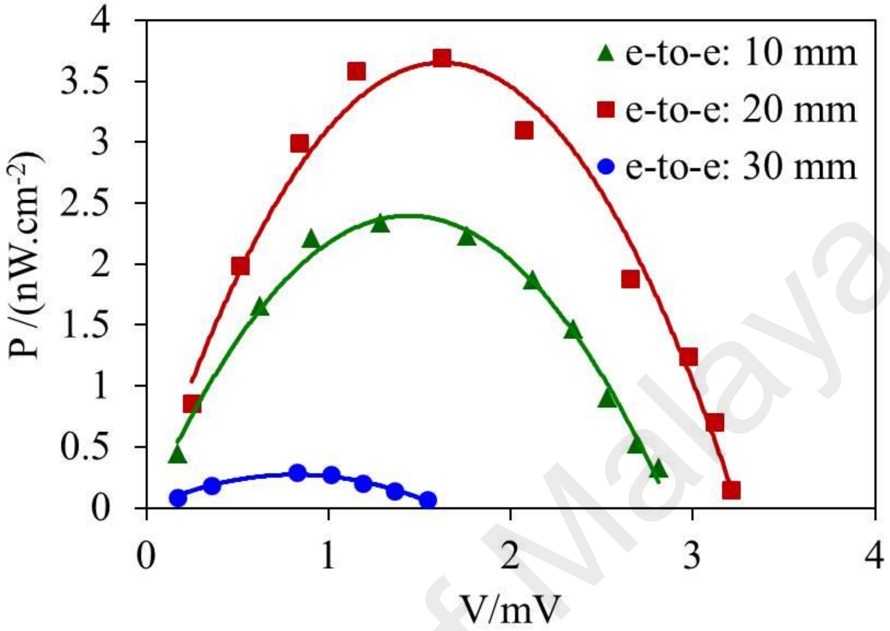

Figure 3.9: Power generation curves of TEC containing ACN-diluted-[EMIM][EtSO$_4$]

Conversely, for ACN-diluted-[EMIM][EtSO$_4$] solution a large drop in thermal gradient can be witnessed i.e. ΔT_{act}=*8*°C, due to the higher fluidity and convenient heat flow. The Figure 3.11 (infrared thermal images) demonstrates the quick heat flow in ACN-diluted-[EMIM][EtSO$_4$] solution disallowing the electrodes to maintain high temperature gradient; however, the viscous nature of the pure [EMIM][EtSO$_4$] offers significant hindrance to the heat waves from hot electrode to cold electrode maintaining better thermal gradient. The results are summarized in Table 3.1.

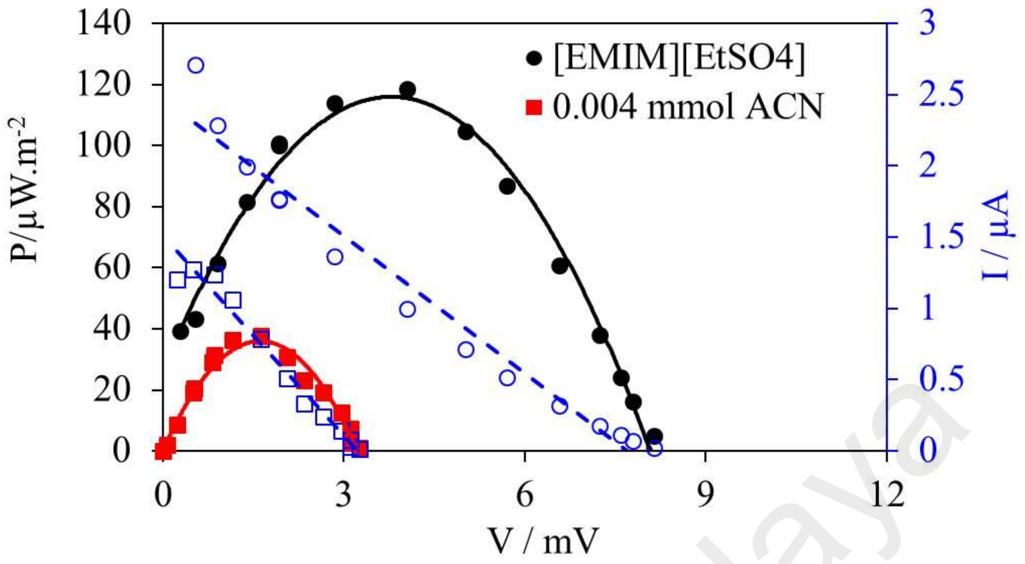

Figure3.10: Comparison of Power outputs of TEC containing [EMIM][EtSO$_4$] and ACN-diluted-[EMIM][EtSO$_4$] samples

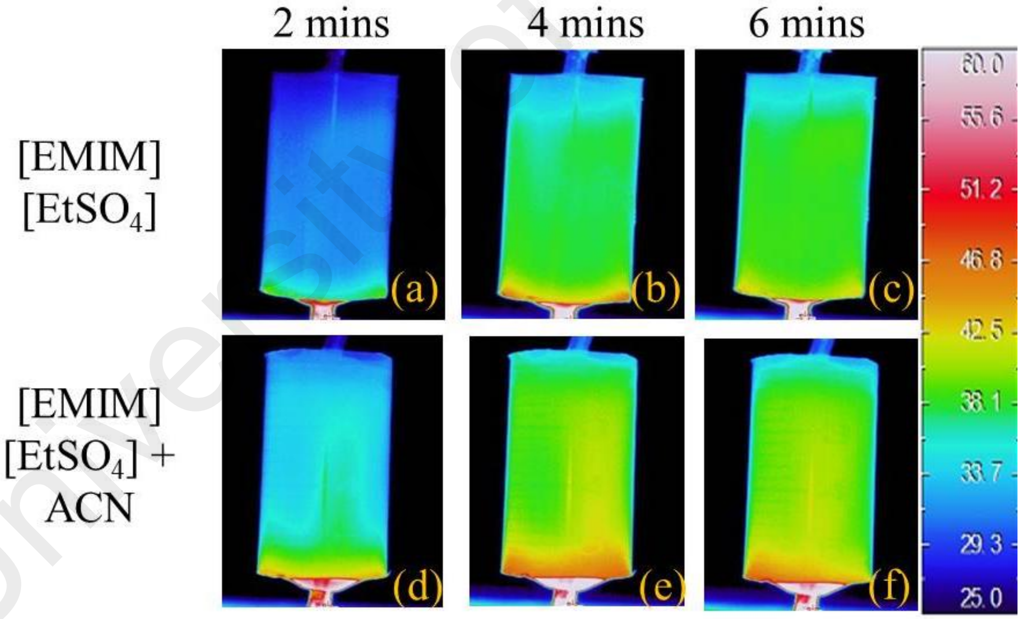

Figure3.11: Infrared Thermography of TEC containing [EMIM][EtSO$_4$] and ACN-diluted-[EMIM][EtSO$_4$] samples

Table 3.1: The interplay between thermophysical properties of the electrolytes

Samples	**Fluidity**	**σ (mS.cm^{-1})**	**D x (10^{-10}) (m^2.s^{-1})**	**K_{th} (W.m^{-1}K^{-1})**	**Max. Power Density (μW.m^{-2})**
[EMIM] [EtSO$_4$]	Increases with ACN addition	*3.5*	*0.3*	*0.18*	*118.5*
[EMIM] [EtSO$_4$] +ACN		*7.5*	*0.6*	*0.24*	*36.1*

3.4 Conclusion

Thermally driven electrochemical cells (thermocells) are able to convert thermal gradient applied across redox electrolyte into electricity. The performance of the thermocells heavily depends on the magnitude and integrity of the applied thermal gradient. Herein, the study is focused on the iodide/triiodide (I^-/I_3^-) based 1-Ethyl-3-methyl-imidazolium Ethylsulfate ([EMIM][EtSO$_4$]) solutions in a thermocell. In order to comprehend the role of fluidity of the electrolyte, three set of solutions by diluting [EMIM][EtSO$_4$] with *0.002, 0.004*, and *0.010* mol of Acetonitrile (ACN) are prepared. A significant improvement in ionic conductivity (σ) and electrochemical Seebeck (S_e) of diluted electrolytes is observed as compared to base [EMIM][EtSO$_4$] owing to the solvent organization. However, the infra-red thermography indicated faster heat flow in ACN-diluted-[EMIM][EtSO$_4$] as compared to the base [EMIM][EtSO$_4$]. Therefore, the maximum power density of base [EMIM][EtSO$_4$] (i.e. *118.5* μW.m^{-2}) is *3* times higher than the ACN-diluted-

[EMIM][$EtSO_4$] (i.e. *36.1* $\mu W.m^{-2}$) because of the lower thermal conductivity. Hence this chapter illustrates the compromise between the fast mass/flow transfer due to fluidity (of diluted samples) and the low thermal conductivity (of the pure [EMIM][$EtSO_4$]).

CHAPTER 4:

HIGH THERMAL GRADIENT IN THERMO-ELECTROCHEMICAL CELLS BY INSERTION OF A POLY(VINYLIDENE FLUORIDE) MEMBRANE

4.1 Introduction

In the previous chapter, it has been shown that the increased thermal conductivity of the composite electrolyte completely negates the improvement brought in Seebeck coefficient, ionic conductivity and the diffusion coefficient by the action of the organic solvent. This is not surprising for thermoelectric researchers as this trade-off between ionic conductivity and thermal conductivity has been a serious stalemate for thermoelectric developments. The performance of a thermoelectric module is governed by a dimensionless figure of merit (ZT) which is defined by equation (4.1).

$$ZT = \left(\frac{\sigma \cdot \alpha^2}{K_{elec} + K_{latt}} \right) \cdot T \qquad (4.1)$$

where "σ" is electrical conductivity (S/m), "α" is the thermoelectric, or "Seebeck", coefficient (V/K), "T" is the absolute temperature (K) while K_{elec} and K_{latt} are the electronic and lattice contribution of thermal conductivity (W/m·K) of the material, respectively. Here it can be noted that for a material with maximum ionic conductivity and minimum thermal conductivity shall realize highest ZT value, however, both of these conductivities are deeply rooted by a common factor of "number of electrons". Once ionic conductivity is increased by the virtue of doping free electrons, these charge carriers simultaneously increase the undesired thermal conductivity. The results presented in chapter 3 show that the same trade-off has to be overcome for liquid thermoelectrics. Hence electrolytes with minimum thermal conductivity which can offer maximum thermal resistance to the heat transport within the cell are desired.

Rather than preparing electrolytes with minimum thermal conductivity and maximum ionic conductivity this research dissertation presents a novel strategy to mitigate the heat transfer within the cell by embedding a polymer membrane between the two electrodes. The motivation of this strategy is to utilize the higher ionic conductivity of the electrolytes and hindering the heat flow externally by a thermal insulating membrane, in this way the trade-of relation between the ionic and thermal conductivity can be avoided. An ideal separator should be porous in order to allow ionic transport, yet highly thermal resistive in order to maintain a large temperature gradient between the electrodes. PVDF was chosen for this study as it is an excellent thermal insulator and is also highly chemically stable polymer, in particular with respect to the redox couple.

Additionally, films of PVDF can be easily fabricated through facile methods such as phase inversion and electrospinning. PVDF has also been used in energy storage and conversion applications such as batteries and fuel cells (Ji, Zhu, Cui, Zhang, & Xu, 2007; Q.-Y. Wu et al., 2016). For example, separators of PVDF-co-hexafluoropropylene (PVDF-HFP), sandwiched poly(m-phenylene isophthalamide) (PMIA) between two PVDF layers (PVDF/PMIA/PVDF) and sandwiched PVDF layer between two poly(phthalazinone ether sulfone ketone) (PPESK) (PPESK/PVDF/PPESK) have been studied for Li-ion batteries (Lu et al., 2013; Zhai et al., 2014). Researchers have also explored PVDF membranes in fuel cells and piezoelectric devices (Inan, Doğan, & Güngör, 2013; Shin et al., 2010). Therefore, the properties of PVDF which are desired for thermocell applications and its applications in other energy devices encouraged the implementation of PVDF as the starting candidate; however, this research is not limited to PVDF. The chapter 6 is dedicated to experimentally evaluate other materials as the membranes for thermocell applications.

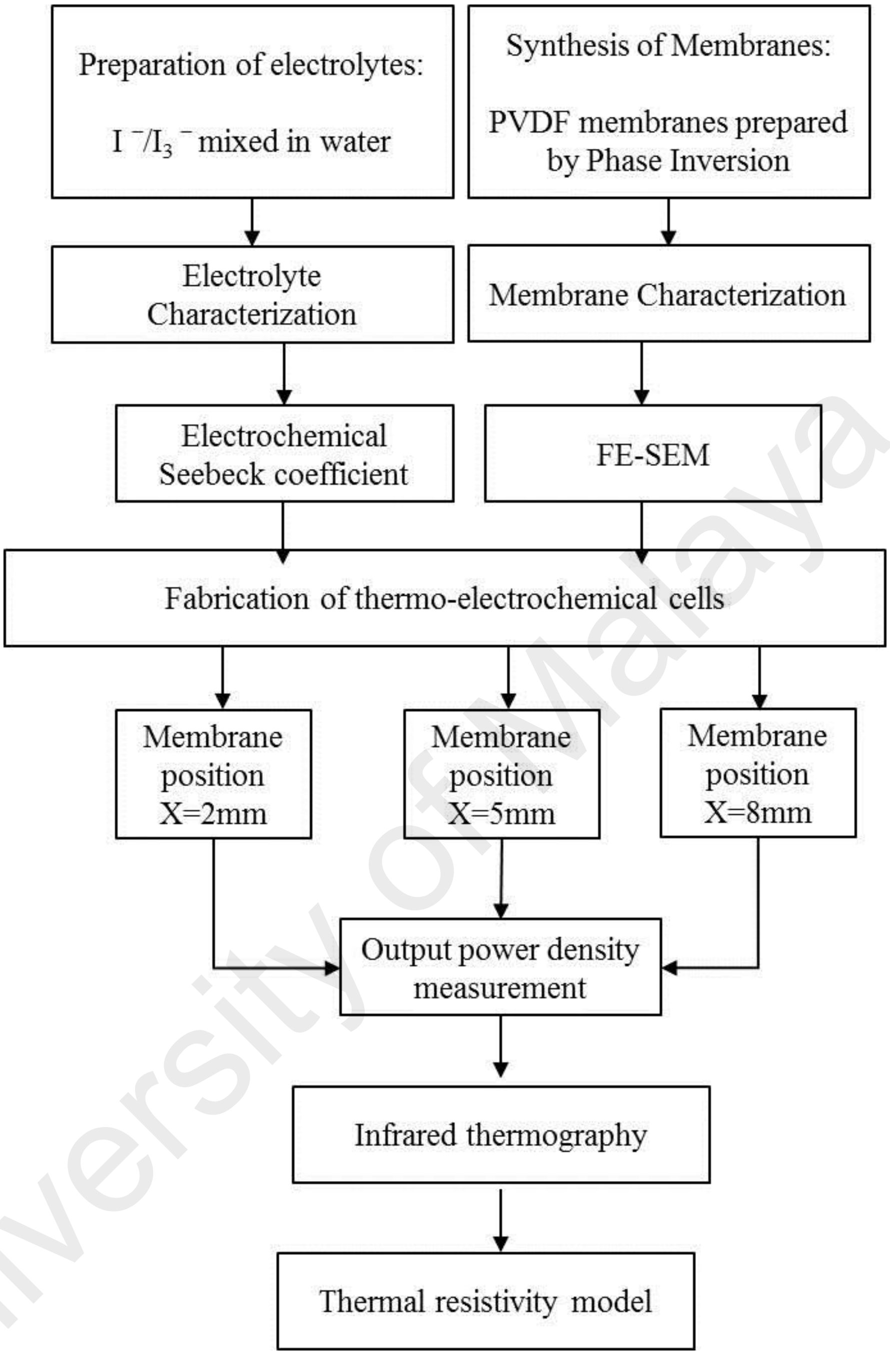

Figure 4.1: Flow-chart of the experimental methodology and results

4.2 Methodology

4.2.1 Materials

The iodide/triiodide (I^-/I_3^-) redox solution (0.7 M) was prepared in 50 ml distilled water by dissolution of Iodine (5 g, Sigma Aldrich; ≥ 99.8%) and Potassium Iodide (10 g, Sigma Aldrich; ≥ 99.5%). The solution was heated to 50 °C for 10 mins to ensure proper solubility. A 200 μm thick PVDF membrane was prepared by phase inversion method. Commercially available Poly(Vinylidene Fluoride) (PVDF, Kynar® K-761, molecular weight of 440,000, density=1.7 g/ml and melt temperature ~ 165°C) powder was mixed with 1-Methyl-2-Pyrrolidinone (NMP) in a ratio of 18% by wt. The solution was stirred for 24 hours at 60 °C. The polymer solution was then cast on a glass plate and the resultant flat sheet membranes were immediately immersed in a coagulation bath containing deionised water. The FE-SEM micrographs of the as-prepared PVDF membranes are shown in Figure 4.2.

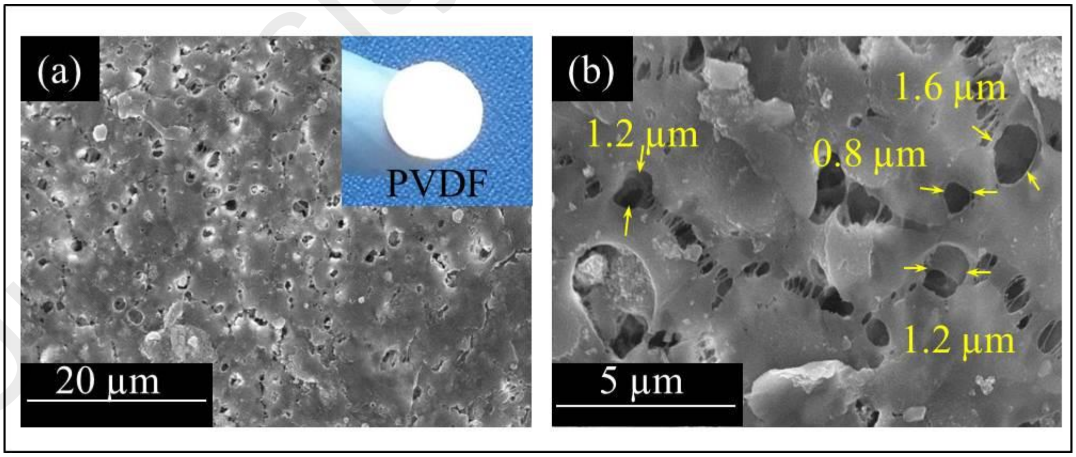

Figure 4.2: FE-SEM micrographsof the PVDF membranes embedded in MTECs

4.2.2 Measurement of the Seebeck coefficient of the I^-/I_3^- aqueous redox solution

The prepared I^-/I_3^- aqueous redox solution was put in two compartments (Pyrex glass beakers), according to the schematic shown in Figure 1.2. Each compartment contained a Pt electrode. The physical exchange of the solutions between the two compartments was established by providing a salt bridge containing the same solution. Pt electrodes were cleaned with concentrated HNO_3 followed by methanol rinsing. The thermal gradient was created by heating one of the compartments through an electrically operated heater at 0.2 °C/min rate while maintaining the other at room temperature.

4.2.3 Morphological and Heat Transfer Characterization

The surface morphology of PVDF membrane was studied by FE-SEM (HITACHI SU8030). Infrared Thermography was carried out at the framerate of 8.5 Hz through R300SR-HB (Nippon Avionics Co. Ltd.) maintaining similar environmental conditions to comprehend the role of membranes in enhancing thermal gradient within the thermocells.

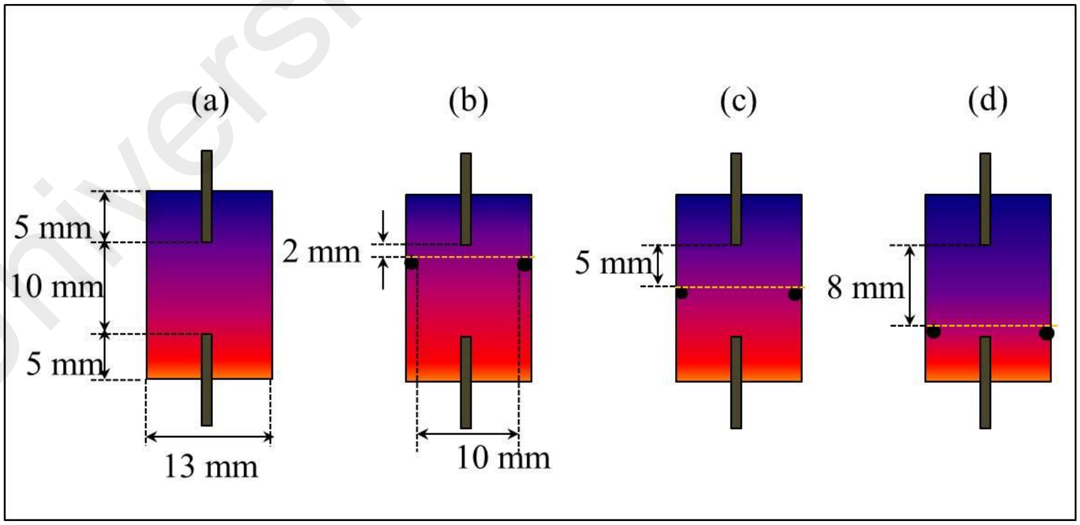

Figure 4.3: Schematic diagram of TEC and MTECs.

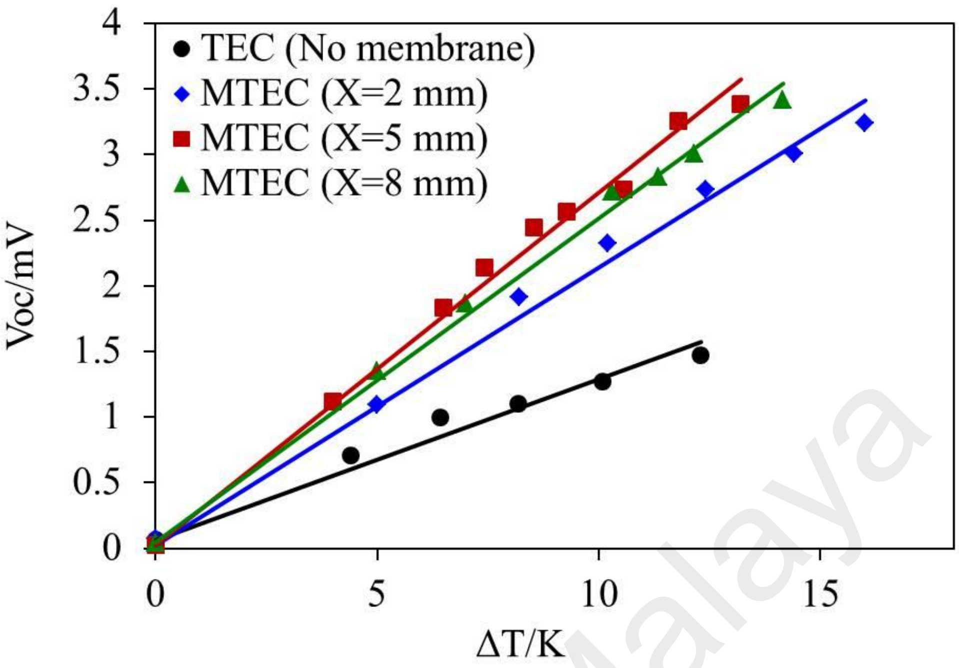

Figure 4.4: Temperature dependence of Open Circuit Voltage (V_{oc}) TEC and MTECs

4.2.4 Thermo-Electrochemical Cell Fabrication and Measurements

Thermo-electrochemical performance of the redox solution with PVDF membranes was studied in a 13 mm diameter and 20 mm length cells (Figure 4.3). The two open ends of the thermocell were closed by rubber sealants to ensure no leakage and the redox solution was inserted through a syringe. The distance between the vertically positioned graphite electrodes were kept constant at 10 mm while the membrane positions (x) were altered between 2 mm, 5 mm and 8 mm away from the top (cold) electrode. For MTECs, a rubber O-ring (ϕ_{out}=13 mm and ϕ_{in}=10 mm) was used to hold the membrane in the intended positions (Figure 4.3(b,c,d)). The reproducibility of the results was examined and the difference in Seebeck values, on average, was found to be ±0.02 mV/K. The electrodes were cleaned by abrasive paper followed by ultrasonic cleaning with acetone. The thermocells were heated in cold-above-hot arrangement at 0.2 – 0.5 °C/min and the open circuit voltage (V_{oc}) was measured by an Agilent 34461A $6_{1/2}$ digital multimeter. The electrochemical Seebeck coefficient was evaluated by the slope of the linear fit between V_{oc} and ΔT. For power output measurements the TEC and MTECs were connected to a variable resistor box (Elenco RS-500), different resistive loads (R,Ω) were applied and the corresponding cell potentials (V, mV) were recorded. The Ohm's law ($P=V^2/R$) was used to calculate the power values.

4.3 Results

The electrochemical Seebeck coefficient (S_e) for the 0.7 M $I^-/I_3^-{}_{(aq)}$ redox couple was 0.4 mV/K when tested in the two compartment cell (Figure 1.2). This is 0.13 mV/K less than the reported value of 0.53 ±0.04 mV/K for a 0.4 M solution, consistent with the expectation that for this range of concentrations, an increase in molarity results in a decrease in S_e (Abraham et al., 2011; Abraham, MacFarlane, & Pringle, 2013; Abraham et al., 2014). However, highly concentrated solutions are preferred for higher power outputs from the thermocells (Alzahrani, Black, Goonetilleke, Panchompoo, & Aldous, 2015; Uhl et al., 2014). The designs of thermocells used in present work and the thermo-electrochemical performances of TECs (membrane less) and MTECs (membrane inserted TEC) are depicted in Figure 4.3. The maximum open circuit voltage (V_{oc}) generated by the conventional TEC is 1.3 mV at the temperature gradient of 12 K. However, the introduction of a PVDF membrane in the TEC significantly enhances the V_{oc} to 2.7 mV for the case of x=5 mm, at the same value of externally applied ΔT (Figure 4.4). The details of open circuit voltages from the TEC and MTECs are given in Table 4.1. The origin of this higher performance is enhancement of the thermal gradient between the two electrodes due to the presence of the PVDF membrane, which has the effect of decreasing convective flow between the electrodes. By creating a thermal barrier between the two halves of the cell the temperature at the working surfaces of the electrodes are able to more closely approach the externally applied temperatures, thus maximizing the internal thermal gradient and achieving the maximum V_{oc}. An illustration of the heat flow in a TEC and MTEC are presented in Figure 4.5 (a,b) and the thermal barrier is quantitatively expressed as a thermal resistivity in Figure 4.6 (a,b).

In this chapter, we first discuss the influence of PVDF membrane on the power generation characteristics of the TEC and MTECs. Then, visualisation of the mass and heat transport within the TEC and MTEC using infrared thermography allows insight into the role of the membrane separator in these cells.

4.3.1 Power Generation characteristics of TEC and MTEC

Inserting the PVDF membrane into the TEC has the direct benefit of enhancing the temperature gradient, and hence the generated voltage, as illustrated in Figure 4.4. These results are summarised in Table 4.1, where an improvement of 52% was achieved for the case of membrane at x=5 mm compared to the TEC. Consequently, the overall thermo-electrochemical power generation of the MTEC is shown to be enhanced significantly compared to the TEC as expressed in Figure 4.7. The maximum power density from the MTEC was 245 nWcm^{-2} , achieved for the case of x =5 mm, measured at temperature gradient of 10 K, which is almost four times higher than the TEC maximum power density (54 nWcm^{-2}).

It is to be noted that each membrane configuration in MTECs results in improved cell potential as compared to the TEC. In Table 4.1, the calculated thermal gradient between the electrodes is presented, using $\Delta T_{calc} = \Delta V/S_e$, where S_e = 0.4 mV/K and ΔV in each case is the open-circuit voltage recorded for the cases of x= 2 mm, 5 mm, and 8 mm respectively.

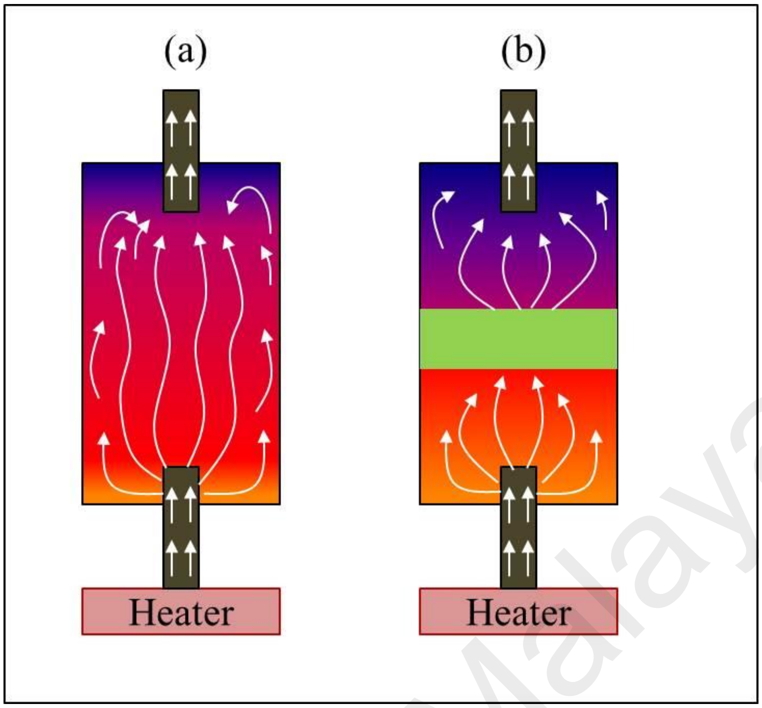

Figure 4.5: Schematic illustration of the heat flow in a (a) TEC and (b) MTEC

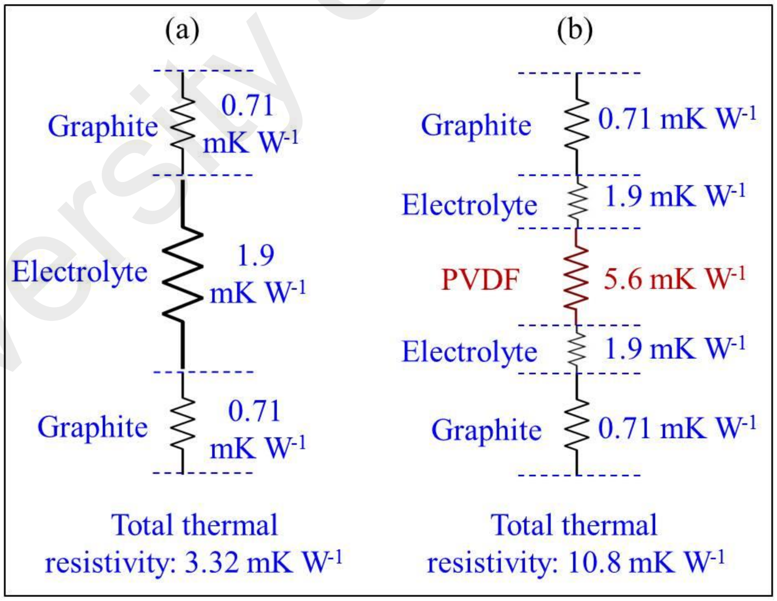

Figure 4.6: Thermal resistive model of (a) TEC and (b) MTECs

The Table 4.1 shows that a TEC is only able to provide a temperature gradient of 2.7 K between the electrodes, whereas the externally applied temperature gradient is 10 K. This observation further confirms the rapid heat flow in the TEC cases. In all the MTECs the thermal gradient between the electrodes is improved as compared to the TEC, reaching an optimal temperature gradient (8.8 K) for x=5 mm. Consequently, this MTEC provides the best power performance. Additionally, the lowest power generation of 61 nWcm^{-2} was achieved with the x=2 mm MTEC, when the membrane is closer to the cold electrode, which has the smallest thermal gradient amongst the membrane inserted cases.

Table 4.1: Summary of the TEC and MTEC results

Results summary		**(a) Data from Figure 4.4 (Electrochemical measurements)**	**(b) Data from Figure 4.7 (Power Curves)**			**(c) Data from Figure 4.9 (Infra-red thermal images)**	
		Open Circuit Voltage (V_{oc}, mV) @ *12* K)	**Max. Cell Potential (V, mV)**	**Max. Power Output (nW/cm^2)**	**Calc. Thermal gradient (ΔT_{calc}, K)**	**Peak 1**	**Peak 2**
						Range (°C)	**Range (°C)**
TEC	**No Membrane**	1.3	1.1	54	2.7	30.4-31.8	-----
MTEC	**X=2 mm**	2.6	2.6	61	6.5	30.9-31.5	34.0-34.8
	X=5 mm	2.7	3.5	245	8.8	33.7-34.8	38.7-39.6
	X=8 mm	2.8	3.0	135	7.5	34.0-35.6	39.0-40.1

4.3.2 Mass and heat transfer characteristics of the TEC

Reduction, in the case of the (I^-/I_3^-) redox couple, occurs at the colder electrode (i.e. the cathode). The reduced species, migrate towards the anode where they oxidize; releasing the electrons (Mua & Quickenden, 1996; Quickenden & Mua, 1995). This can be visualised in the infrared thermal images of the TECs in Figure 4.7(I), where the convection effects coupled with the thermal diffusion allows fast equilibration of the temperature within the cell. After 29 mins of heating the average temperature of the redox solution was 26.7 °C (±1°C). Thus, in the case of the TEC the heat transfer through mass (fluid) flow rapidly diminishes the temperature gradient across the TEC that is critical to the its operation. The images of Figure 4.7(I) indicated that after 34 and 38 mins the temperature of the solution has been increased to 28.4°C (±1°C) and 31.0°C (±1°C), and thus the temperature gradient across the vertical axis has been significantly reduced. The maximum temperature difference was achieved after 38 mins of heating, thus resulting in the maximum V_{oc}. The Figure 4.8 shows a quantitative representation of temperature distribution within the cell, extrapolated from Figure 4.7 using thermal imaging software after 38 mins of heating. In the histogram of the TEC, the temperature of the electrolyte is concentrated around ca. 30.4 - 31.8 °C (±1°C) resulting in a unimodal distribution (Figure 4.8a). The unimodal temperature distribution supports the weaker temperature gradient maintained between the electrodes of TEC.

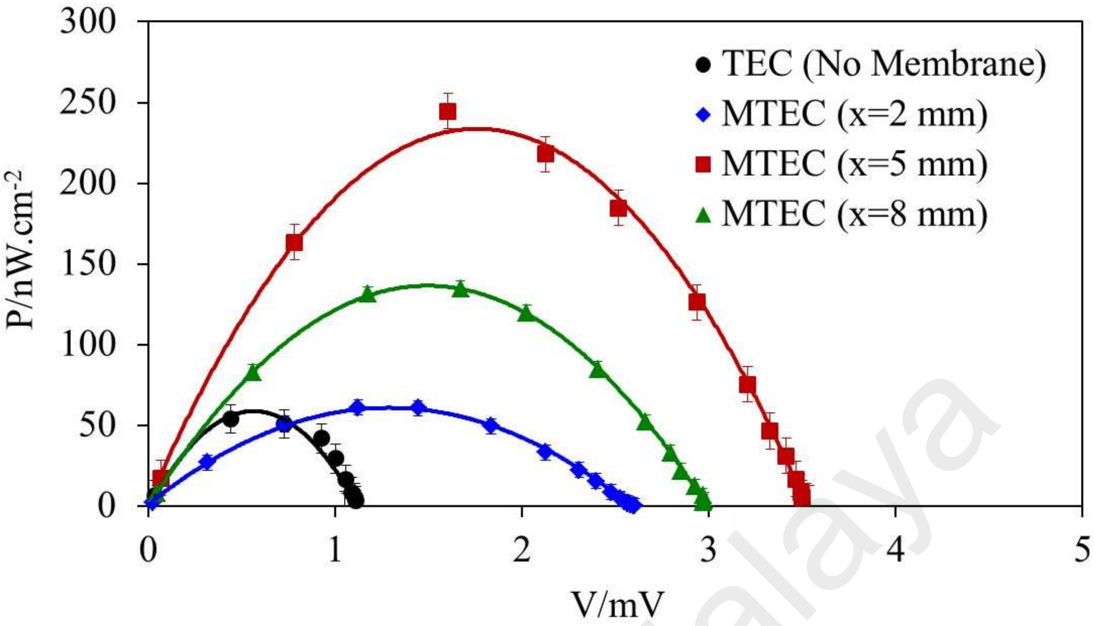

Figure 4.7: Power output curves for TEC and MTEC (x=2, 5, and 8 mm)

4.3.3 Mass and heat transfer characteristics of the MTECs

The effect of the insertion of a PVDF membrane on the heat flow is illustrated in Figure 4.8(II,III,IV) for the cases of membrane position 2 mm, 5 mm, and 8 mm, respectively. The PVDF material is an efficient thermal insulator with thermal resistivity of ~ 6 mK W^{-1} (Camacho et al., 2013; Curcio & Drioli, 2005; Yu, Huang, Wu, & Jiang, 2011). The thermal resistive effects of PVDF in MTECs obstruct the heat flow between the electrodes creating distinct temperature zones, thus resulting in bimodal temperature distribution in MTECs, as shown in Figure 4.9(b,c,d). In the TEC after heating for 38 mins the average temperature of the electrolyte was 31.0°C (±1°C), whereas after the same heating time in the MTECs temperature zones of 31°C and 35°C (±1°C) in the x=2 mm case, 34°C and 39°C (±1°C) in the x=5 mm case, and 35°C and 40°C (±1°C) in the x= 8 mm case were observed (Figure 4.9(b,c,d)). The details of the peak positions and breadths are given in Table 4.1. Therefore, in summary, the presence of the membrane acts as a thermal resistor to hinder heat flow. However, the improved open circuit voltage and maximum power density also indicate that ion transfer between the electrodes is not adversely affected by the PVDF barrier.

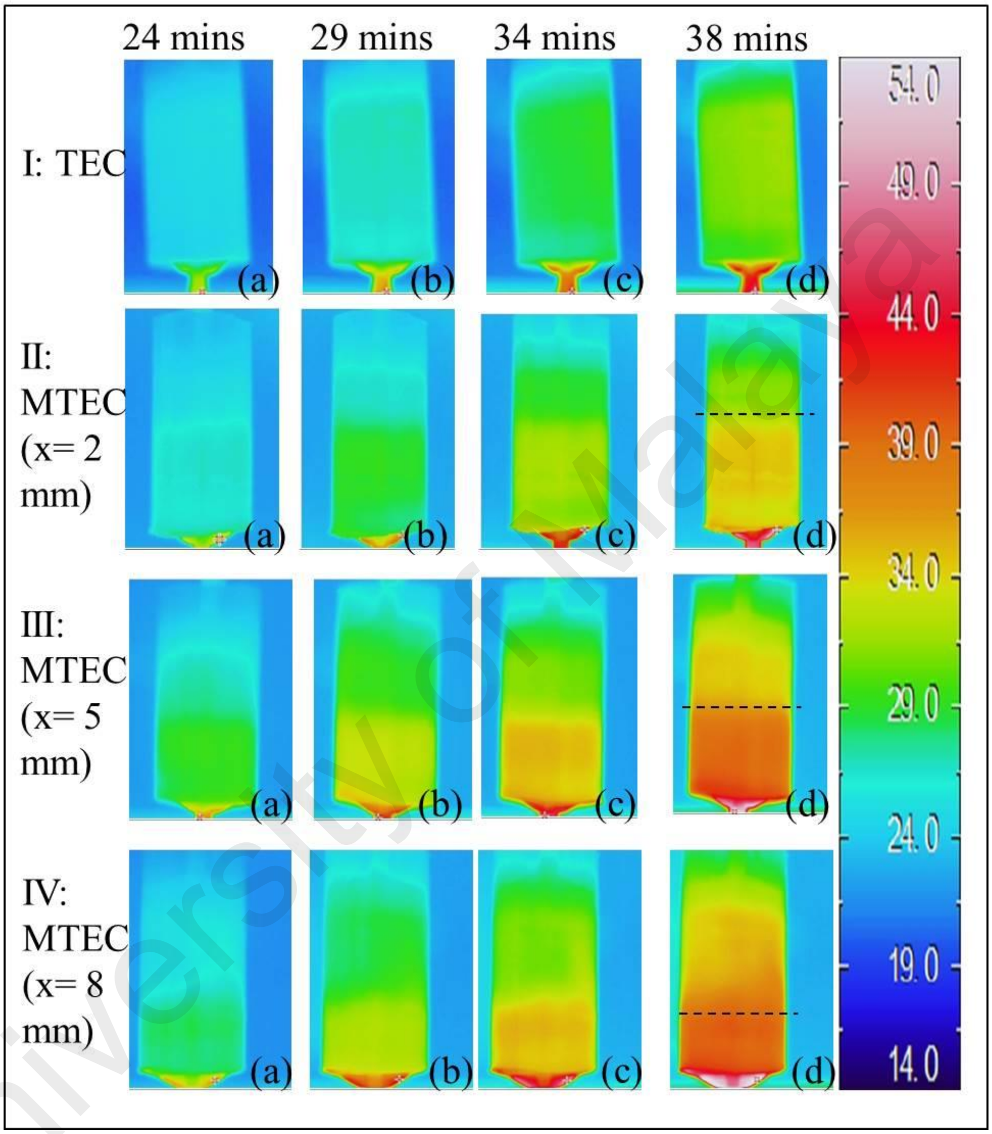

Figure 4.8: Infrared thermography of TEC and MTECs at different time spans

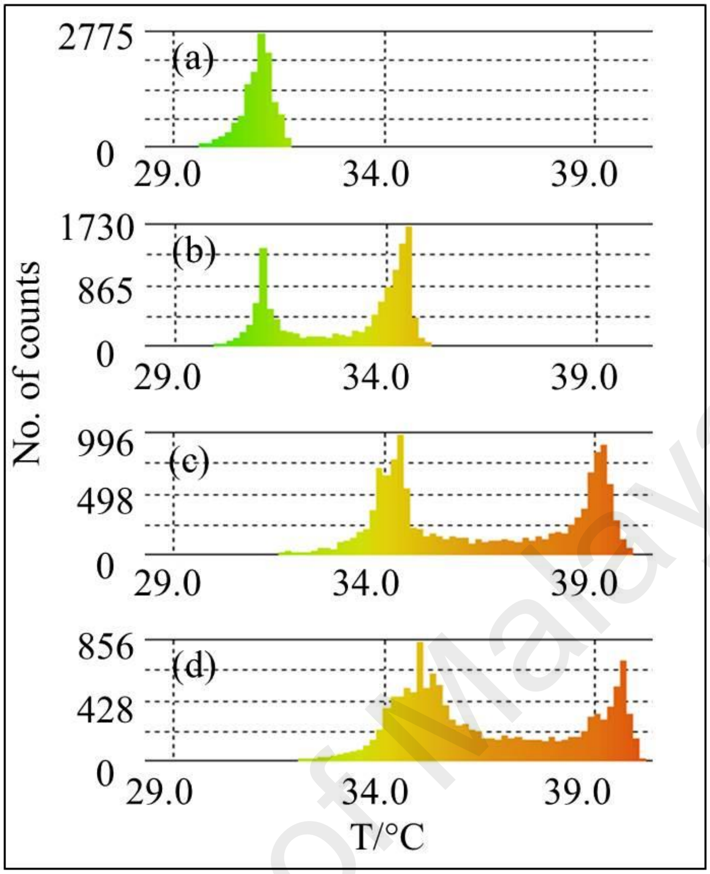

Figure 4.9: Temperature Histograms of TEC and MTECs

4.3.4 Thermal resistance model

To further elucidate the effect of the PVDF membrane inclusion in the TEC, a thermal resistance model is proposed in Figure 4.6. A temperature gradient is key to the voltage generation in a TEC, and in an ideal case this temperature gradient is maintained throughout the experiment and is equivalent to the difference in applied temperatures at the electrodes. However, more realistically, losses occur due to a number of factors: temperature gradients in the electrodes, heat lost to the environment, and convection and conduction within the solution. For TEC the equivalent thermal resistance circuit can be represented by Figure 4.6(a). For the solution, the thermal resistance may be described in terms of its thermal conductivity and thermal mass transfer (predominantly convection). In this case, the relatively high convection of the solution can be represented by a low thermal resistance. As noted previously, this results in the solution reaching thermal equilibrium relatively quickly within the TEC, which significantly diminishes the temperature gradient and the power output to 2.7 K and 54 nWcm^{-2}, respectively.

In comparison, the equivalent thermal resistance of the MTEC is represented in Figure 4.6(b), where the thermal resistance of the PVDF membrane is much larger than those of the solution or the electrodes. Furthermore, the presence of the membrane also has a direct impact on the thermal resistance of the solution: whilst the thermal conductivity may be assumed as constant, the thermal mass transfer effects (i.e. convection) is diminished as the volume is now physically divided into two half cells. Consequently, the thermal resistance of the solution is also increased prompting MTEC closer to the applied temperature gradient i.e. 8.8 K. Of further note is that the optimum performance of the cell (245 nWcm^{-2}) is achieved at a membrane position of x=5 mm, i.e. equidistant from both electrodes, where the power output in this configuration of membrane has provided 78% improvement to the performance of the TEC. This observation can also be explained within the context of limiting the convection within the half cells, as this configuration allows the minimum electrolyte volume on either side of the membrane.

4.4 Conclusion

Thermo-Electrochemical cells (Thermocells/TECs) transform thermal energy into electricity by means of electrochemical potential disequilibrium between electrodes induced by a temperature gradient (ΔT). Heat conduction across the terminals of the cell is one of the primary reasons for device inefficiency. Herein, the Poly(Vinylidene Fluoride) (PVDF) membrane was embedded in thermocells to mitigate the heat transfer effects, these membrane-thermocells are referred to as MTECs. At a ΔT of 12 K, an improvement in the open circuit voltage (V_{oc}) of the TEC from 1.3 mV to 2.8 mV is obtained by employment of the membrane. The PVDF membrane is employed at three different locations between the electrodes i.e. x=2 mm, 5 mm, and 8 mm where ‘x’ defines the distance between the cathode and PVDF membrane. We found that the membrane position at x=5 mm achieves the closest internal ΔT (i.e. 8.8 K) to the externally applied ΔT of 10 K and corresponding power density is 254 nWcm^{-2}; 78% higher than the conventional TEC. Thus, this experimental work form the basis of proposal for mass and heat transfer within thermocells and provides a highly viable strategy for heat transfer mitigation using a mesoporous membrane.

CHAPTER 5:

OPTIMIZATION OF POLY(VINYLIDENE FLUORIDE) MEMBRANES FOR ENHANCED POWER DENSITY OF THERMALLY DRIVEN ELECTROCHEMICAL CELLS

5.1 Introduction

The membrane-embedded thermocells (MTECs) have been introduced in the previous chapter. The difference between MTEC and a conventional TEC is of a mesoporous membrane held between the electrodes in MTECs. It has been shown in details that the polymer membrane acts as the thermal barrier and reduces the heat flow between the electrodes upto 70%. In batteries, generally porous polymer membranes are utilized as the separator between the electrodes which (i) serve as a pathway for the ionic flow and (ii) keep the electrodes separated avoiding any possible short-circuiting. However, in thermocells the polymer separator has an additional role of mitigating convective heat flow across the electrodes as illustrated in our previous reports. The motivation of this chapter is to study the effect of membrane thickness on the produced thermal gradient. It is logical to think that a thicker membrane can produce a higher thermal gradient, but is there any limit for the membrane thickness for the improvement in thermocell performance. Therefore, it is of my main interests to find out a threshold thickness of the membrane suitable for the cell performance? Furthermore, it is well-known that by altering the thickness of the membranes several morphological, physical and electrical properties of the membrane shall vary, therefore, a comprehensive study of these properties and their relationship is discussed in this chapter.

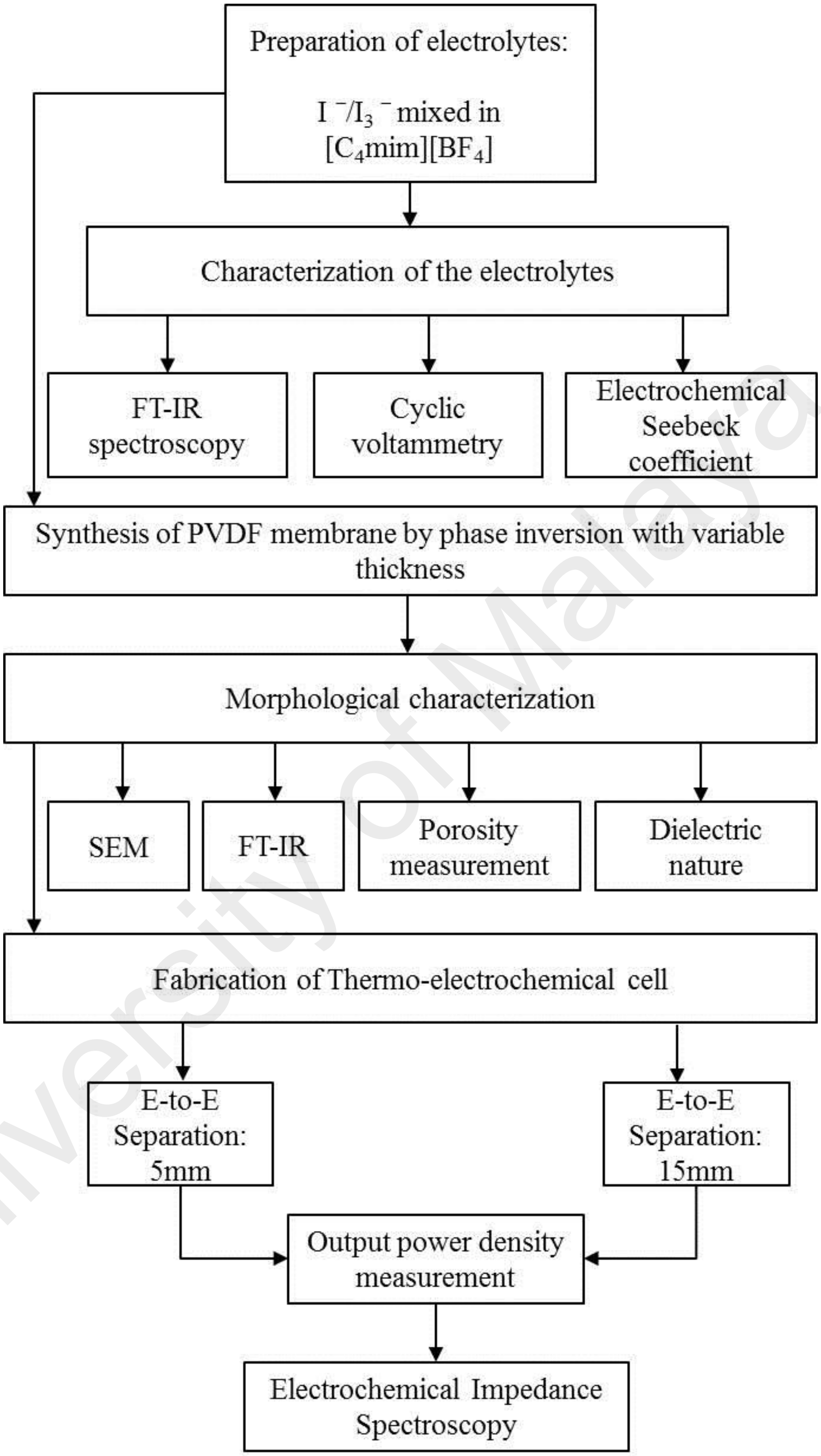

Figure 5.1: Flowchart of the experimental methodology and results

5.2 Methodology

5.2.1 Electrolyte Preparation

1-Butyl-3-Methylimidazolium Tetraflouroborate [C_4mim]·[BF_4] was purchased from MERCK and used without any further processing. Iodine and Potassium Iodide, from Sigma Aldrich, were used to prepare the 0.01M, 0.1M, and 0.3M iodide/triiodide (I^-/I_3^-) redox couples in [C_4mim][BF_4]. The electrolyte was kept at 80˚C under stirring for next 24 hours.

5.2.2 Preparation of PVDF Membranes

The poly(Vinylidene Fluoride) (PVDF) membranes were prepared by phase-inversion method as described in literature (Hashim, Liu, & Li, 2009). Briefly, PVDF powder (15% by wt) was mixed in Dimethyl Sulfoxide (DMSO; 85% by wt) at 60˚C for 24 hours to ensure complete dissolution. The polymer solution was casted on a glass plate followed by an immediate immersion in coagulation bath containing deionized water. Four sheets of PVDF membranes with different thicknesses (100 μm, 200 μm, 400 μm, and 600 μm) were prepared. The flat sheet membranes were kept in deionized water for 24 hours and then dried at room temperature. A disc of 15 mm diameter was cut from the sheets and immersed in the solution of I^-/I_3^- and [C_4mim]·[BF_4] before deploying in the thermocells. The systematic flowchart of the experiments and the results is shown in Figure 5.1.

5.2.3 Material Characterization

Surface morphology of PVDF membranes was investigated through Scanning Electron Microscopy (SEM). The electrochemical nature of the reduction-oxidation reactions of 0.01, 0.1, and 0.3M electrolytes were studied through cyclic voltammetry at the scan rate of 100 mVs^{-1} using Platinum and Carbon as counter and working electrodes, respectively (Ref

600, Gamry Instruments). The polymer structure of PVDF membrane was investigated in the range of 450-4000 cm^{-1} on Fourier Transform Infrared Spectrum (FTIR). The specific pore volume of membranes was measured by BET surface analyser (Micromeritics).

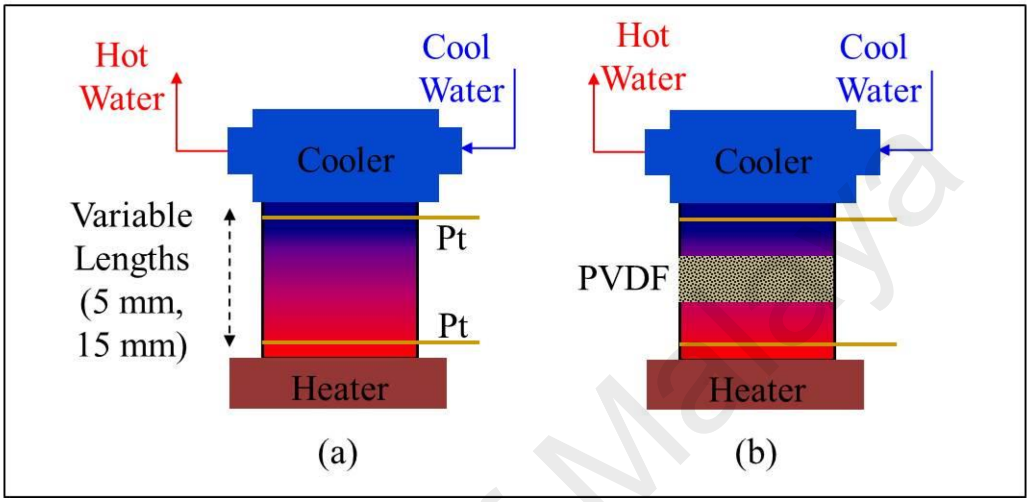

Figure 5.2: Schematic of the TEC and MTEC with auxiliary cooling system

5.2.4 Thermocell Fabrication and Characterization

Thermocells were constructed by 2 mm thick Polypropylene (PP) barrels with inner diameter of 15 mm. Since we were interested to study the effect of electrode-to-electrode (e-to-e) separation on the overall thermocell performance; each of the concentrations was studied in e-to-e separations of 5 mm and 15 mm as shown in Figure 5.2(a). For the TEC containing the membrane (we refer them as *MTECs*) a thermoplastic O-Ring was used to hold the membrane at the centre between the two platinum (Pt) rod electrodes (See Figure 5.2(b)). Pt electrodes were submersed in (conc.) HNO_3 for 1 min and washed properly by Methanol and distilled water before any measurement. After inserting electrolyte, TEC and MTECs were left idle for 30 mins allowing open-circuit voltage to stabilize. The thermocell was heated in cold-above-hot arrangement maintaining a thermal gradient of 45 K. The bottom of the thermocell was kept at 70˚C while the top part was cooled by water circulation. The criteria to proceed in measurements was a constant ΔT of 45K (±1˚C) for 30 mins. Once the desired ΔT was achieved Pt electrodes were connected to a variable resistor box Elenco RS-500 to apply external loads (R; Ω). The potential drop (ΔV) across the electrodes was measured by Agilent 34461A 61/2 digital multimeter and power ($P=\Delta V^2/R$) was calculated by ohm's law as described in (Abraham, MacFarlane, & Pringle, 2013; Gunawan et al., 2014). Corresponding resistances were applied keeping a time interval of 6 mins in between (5 mins to stabilize the cell potential and 1 min to record the potential values).

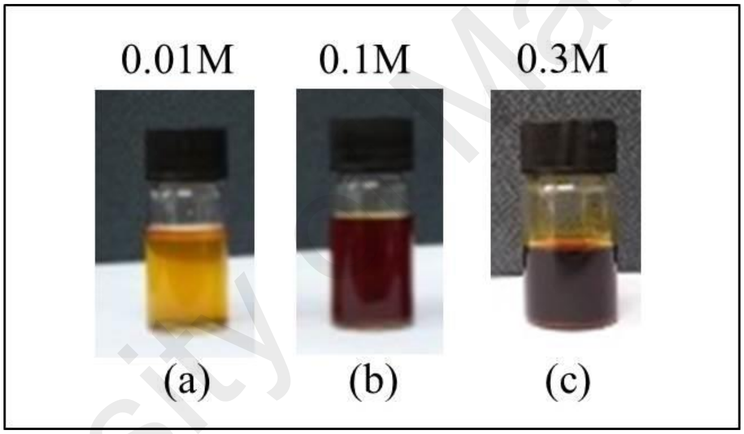

Figure 5.3: The 0.01M, 0.1M, and 0.3M iodide/triiodide (I^-/I_3^-) redox couples in [C_4mim][BF_4]

5.3 Results

5.3.1 Dependence of Power Output on electrolyte concentration

As discussed previously that three different molar concentrations of 0.01M, 0.1M and 0.3M are tested in thermocells as shown in Figure 5.3 (a-c). The electrochemical Seebeck of each electrolyte is presented in Figure 5.4 i.e. 0.44, 0.3, and 0.22 mVK^{-1} for 0.01, 0.1 and 0.3M respectively. In literature the Seebeck value of I^-/I_3^- in ([C_4mim][BF_4]) has been reported as 0.39 mVK^{-1} for 0.1 M concentration (Abraham et al., 2011). We note that our values match well with the reported values i.e. the difference of 0.09 mVK^{-1} is observed. The trend also follows the literature that is the electrochemical Seebeck of the electrolytes reduces as the concentration is increased. The least diluted solution has the Seebeck value of 0.44 mVK^{-1} which is decreased to 0.22 mVK^{-1} as the concentration is raised to 0.3M.

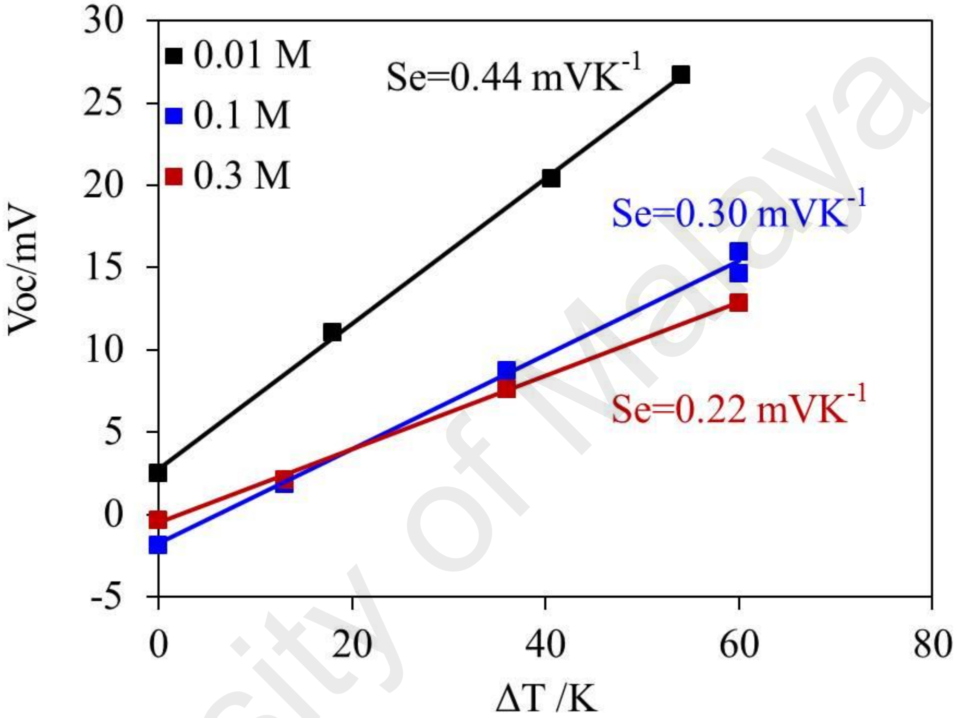

Figure 5.4: Electrochemical Seebeck evaluation of 0.01M, 0.1M, and 0.3M iodide/triiodide (I^-/I_3^-) redox couples in $[C_4mim][BF_4]$

The cyclic voltammograms of the 0.01 M solution in Figure 5.5(a) shows two distinct peaks observed at formal potentials of 62 mV and 420 mV which are attributed to the oxidation of I^- into I_3^- and the formation of I_2, respectively(Ejigu, Lovelock, Licence, & Walsh, 2011; Wan et al., 2015). Hence the formal potential gradually increases as the concentration is increased. For 0.3 M solution the peaks are observed at the formal potentials of 180 mV and 500 mV. Similarly, the peak-to-peak (ΔE_p) separations are also increased with the concentration i.e. for 0.01M solution ΔE_p of I^- oxidation/reduction is

125.5 mV and I_3^- oxidation/reduction is 10.01 mV. However, ΔE_p of I^- oxidation/reduction and I_3^- oxidation/reduction is increased to 338.3 mV and 33.1 mV, respectively for the 0.3 M solution. This is an indication of increased electrolyte viscosity due to the higher amounts of iodine and potassium iodide (Ejigu et al., 2011). Nevertheless, the faradaic peak currents (i_{pc} and i_{pa}) are significantly increased from micro-ampere to milli-ampere scale upon concentrating the solution; boosting the TEC performance.

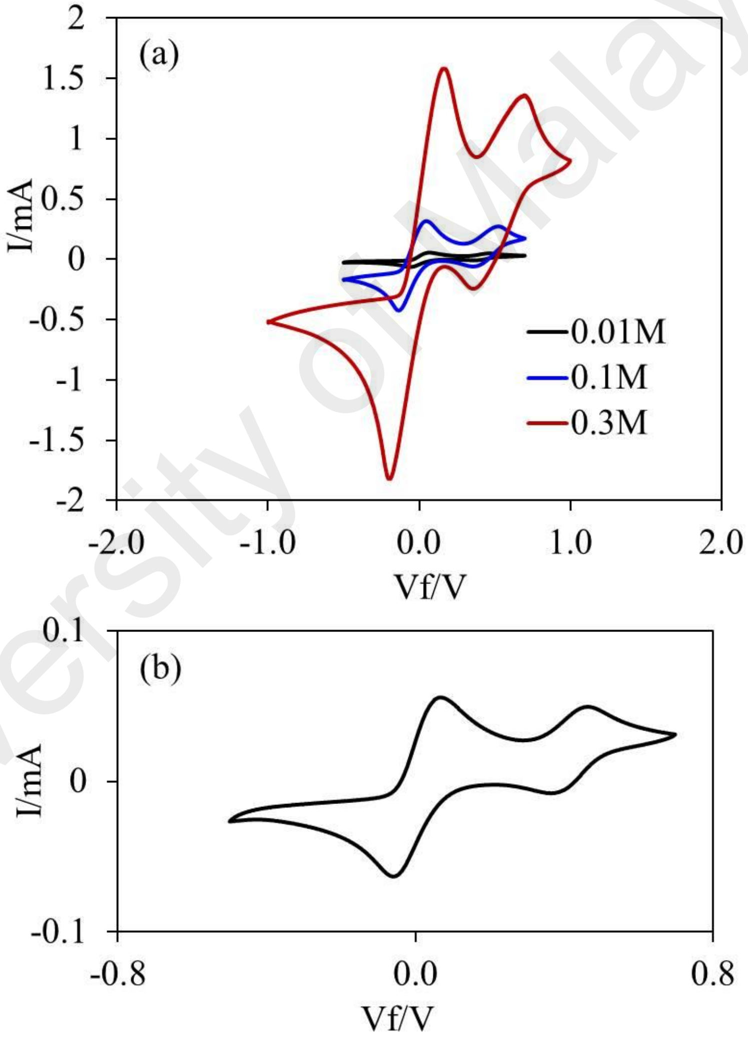

Figure 5.5: Cyclic voltammetry (CV) of iodide/triiodide (I^-/I_3^-) redox couples in $[C_4mim][BF_4]$ (a) CV of 0.01M, 0.1M, and 0.3M solutions (b) CV of 0.01M electrolyte solution showing reduction-oxidation peaks even at lower concentrtaions

The Figure 5.6 (a) and (b) show the power characteristics of the TEC against the current output for each of the concentrations for e-to-e separation of 5mm and 15mm, respectively. The power curves systematically follow the trends observed in CV curves showing higher power density for concentrated solutions owing to amplified current flow. Similar results have been published in literature exhibiting increment in power density with electrolyte concentration (Gunawan et al., 2014; Uhl et al., 2014). For 0.01M, 0.1M, and 0.3M the maximum power generated in e-to-e=15 mm is 0.42 mW.m^{-2}, 0.74 mW.m^{-2} and 1.46 mW.m^{-2}, respectively.

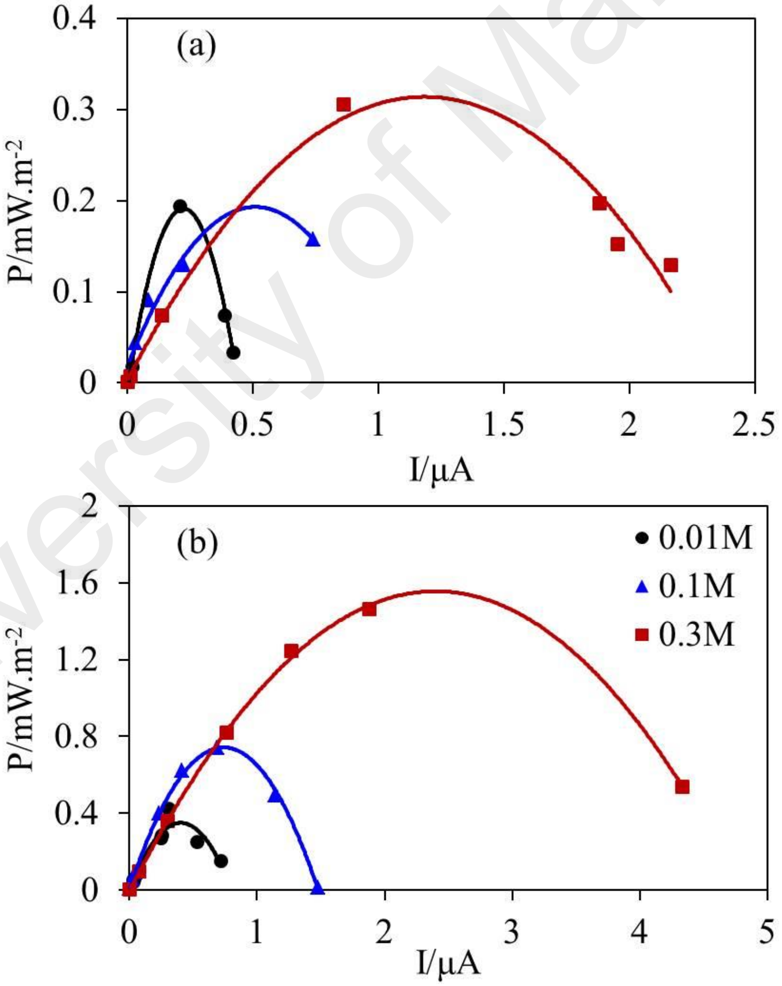

Figure 5.6: Power performance of TEC at various electrode-to-electrode separations (a) e-to-e separation of 5mm and (b) e-to-e separation 15mm

5.3.2 Power Enhancement in Membrane Embedded Thermocells (MTECs)

Since the best thermocell performance is observed with 0.3M electrolyte and 15 mm electrode separation, therefore, the polymer membranes were deployed only in this configuration keeping the membrane thickness as the only variable. In the previous chapter it has been shown that presence of a PVDF membrane between the electrodes in MTEC increased the power density from 54 nW.cm^{-2} to 245 nW.cm^{-2} (Hasan et al., 2016). Here, the threshold thickness of the membrane is found for optimum power density. The ideal membrane thickness should have chemical/thermal stability, optimized porosity, high thermal resistivity and optimized ionic conductivity.

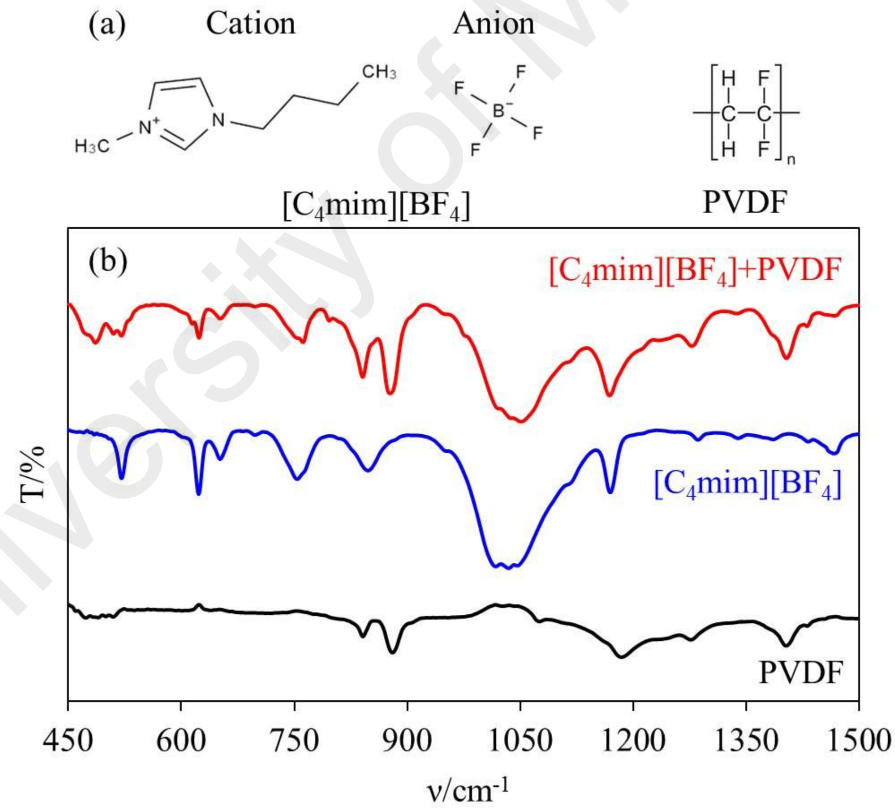

Figure 5.7: (a) Chemical structure of [C_4mim][BF_4] and PVDF (b) FT-IR spectra of PVDF, [C_4mim][BF_4] and PVDF containing [C_4mim][BF_4]

In Figure 5.7(a) the chemical structure of the ioinic liquid i.e. [C_4mim][BF_4] and the membrane i.e. PVDF is shown. In Figure 5.7(b), the FT-IR spectrum exhibits no change in the molecular interactions due to changing the membrane thickness. PVDF is a semi-crystalline polymer which owns four main polymorphs (α, β, δ and γ) characterized on the basis of their electric properties. The α–PVDF is the most stable form at ambient conditions and exhibit a non-polar thus paraelectric behaviour. On the contrary β–PVDF is polar and ferroelectric in nature and widely used for pyroelectric and piezoelectric applications. The remaining two polymorphs i.e. δ and γ are both ferroelectric, however, less explored as compared to former two polymorphs due to their difficult synthesis procedures (M. Li et al., 2013; Ratri & Tashiro, 2013). Thermally induced or stress induced transitions amongst the polymorphs (from α to β or α to δ) have also been reported in the literature. This diversity in the phases is originated by the orientation of the polymeric chains. In case of α–PVDF, $(CH_2–CF_2)_n$ chains are arranged in TG^+TG^- conformation negating the dipole effect. While β–PVDF has zig-zag conformation where the dipole effect is not cancelled internally thus results in a polar phase. FT-IR is a prominent spectroscopy to identify the peaks of respective phases.

It is noted that in the as-prepared membranes the characteristic peaks of β phases are dominantly present; however, traces of α phase are also visible. For the case of β–PVDF, the characteristic peak of 840 cm^{-1} represents the bending of CF_2 and mixed mode of CH_2 rocking and CF_2 asymmetric stretching however the band at 745 cm^{-1} is missing. The secondary peaks at 1431, 1406, 1279, 1074, and 881 cm^{-1} are also associated with β–PVDF (de Jesus Silva, Nascimento, & da Costa, 2016; Lanceros-Mendez, Mano, Costa, & Schmidt, 2001; M. Li et al., 2013; Ratri & Tashiro, 2013; N. Wu et al., 2012). Naturally, the β–PVDF is a dielectric material and the hysteresis loop between the I-V is shown in

Figure 5.8 which is independent of the thickness of the membrane. Before the deployment of the membrane in the cell, it is immersed in the electrolyte solution ((I^-/I_3^-) redox couple added in [C_4mim][BF_4]). The FT-IR spectrum of the polymer membrane, as shown in the Figure 5.7, shows that PVDF structure is intact and there is no chemical reaction between the electrolyte and the membrane.

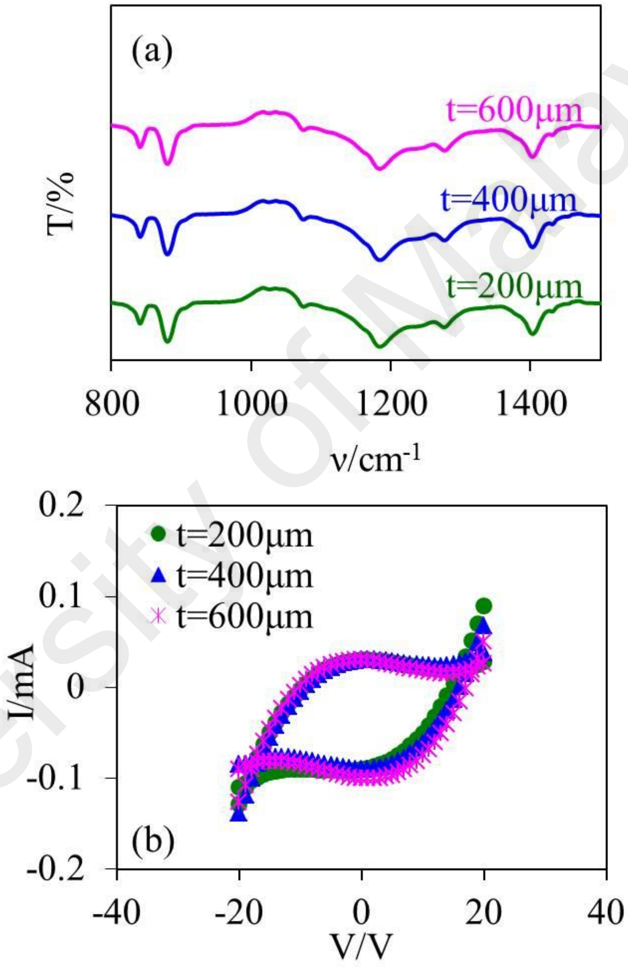

Figure 5.8: FT-IR Spectra and Dielectric behaviour of PVDF films with variable thickness

5.3.2.1 Porosity-Thickness-Power Density Correlation

Thickness of the membrane significantly affects the morphology of the membrane surfaces. In general the porosity of PVDF membranes ranges from 40 – 80% depending on various factors including the polymer content in the solution, solvent, additive and temperature of the water bath etc (AlMarzooqi, Bilad, Mansoor, & Arafat, 2016; Cui, Du, Xu, Ji, & Zhu, 2008; Ji et al., 2007; Pu, He, Wang, Jiang, & Wan, 2006; Zhao, Xu, Chen, & Yang, 2013). The SEM images of the PVDF membranes are shown in Figure 5.9. It is noted that the pore size increases with the increasing thickness, however, the porosity decreases simultaneously. The membrane thickness of 100 μm has the highest porosity and specific pore volume of 71% and 5.9(10^{-2}) cm^3g^{-1}, respectively. Similar porosity of 71.7% in 95 μm thick PVDF membrane has been reported in the literature(Zhao et al., 2013). Nevertheless, this thickness is very low but still improves the thermal gradient between the electrodes as compared to the membrane-less case, therefore improving the power density from 1.5 $mW.m^{-2}$ in TEC to 2.5 $mW.m^{-2}$ as shown in Figure 5.10(a).

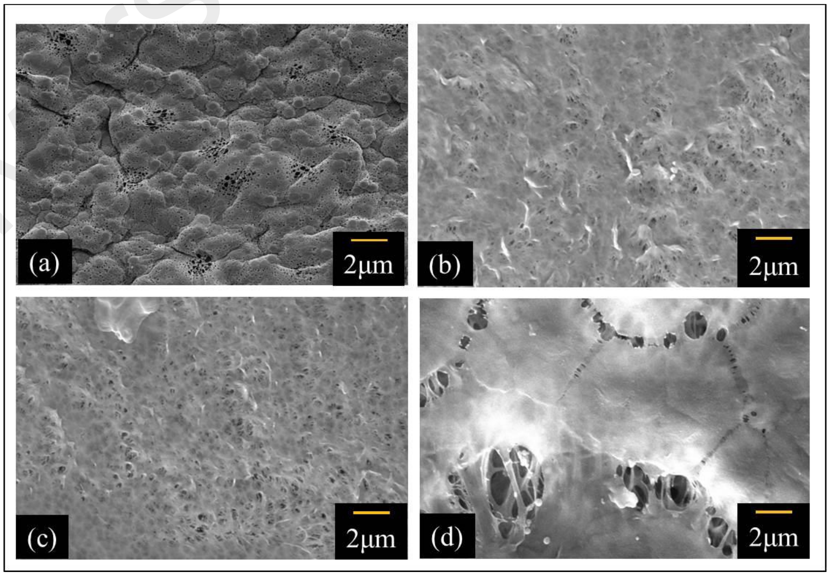

Figure 5.9: SEM micrographs of PVDF membranes with different thicknesses

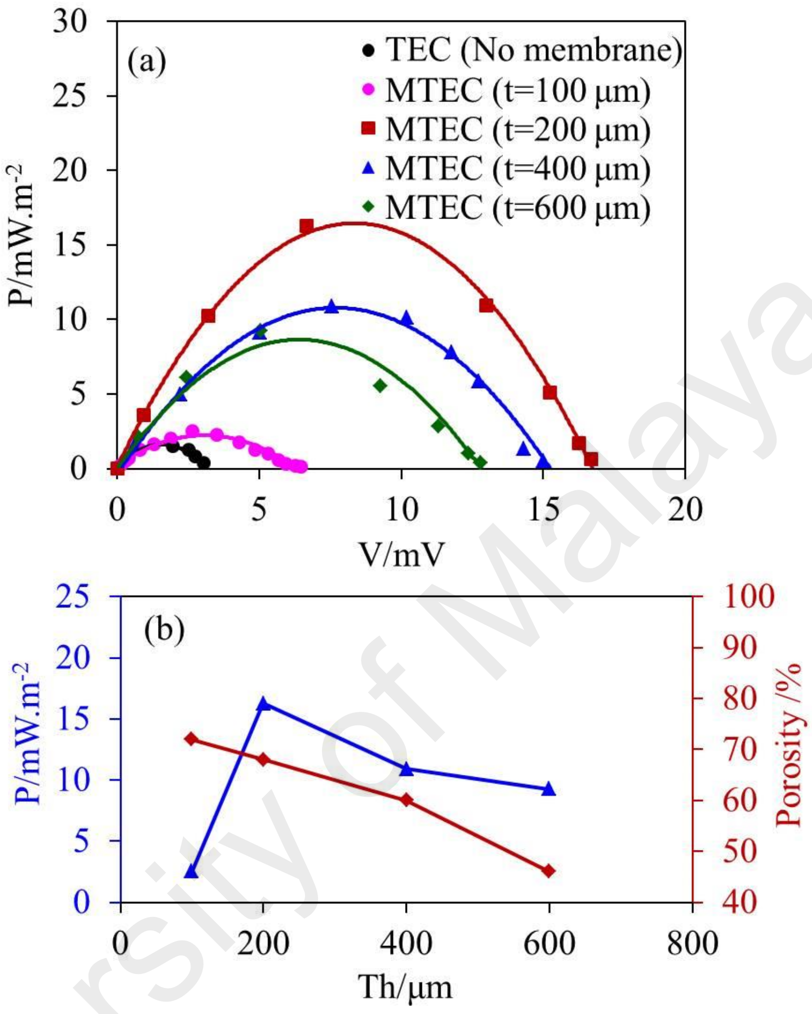

Figure 5.10: Membrane thickness dependent MTEC performance. (a) Power curves for TEC and MTECs (b) Relationship between the power density of MTEC with membrane thickness and porosity.

The low power density of TEC is owing to the lower thermal gradient maintained between the electrodes as the heat transport (through convection) from hot to cold electrode is fast (Ali H Kazim & Cola, 2016). Consequently, a polymer membrane in between the electrodes resists the heat flow and improves the power generation characteristics of thermocells. Similarly, as the membrane thickness is increased to 200 μm; the porosity and the specific pore volume have decreased to 68% and 3(10^{-2}) cm^{3}g^{-1}, respectively. However, the maximum power density dramatically increases to 16.3 $mW.m^{-2}$ which is 91% improvement as compared to the membrane less TEC. This reduction in porosity limits the convective flow and the thickness improves the thermal gradient within the cell, elevating the power density. However, with any further increment in thickness, the power density is decreased. Although the decrease in porosity and pore volume is still witnessed for thicker membranes and they are also beneficial for the thermal resistivity of the thermocell, the overall power density decrement is attributed to the membrane resistance as discussed in the following section.

5.3.2.2 Membrane Resistance and Power Density Correlation

To further elucidate the effect of thickness on the cell performance, we carried out electrochemical impedance spectroscopy (EIS) with our samples as shown in Figure 5.11 with real part of the impedance (Z') plotted on x-axis and imaginary part (Z'') plotted along y-axis. In Figure 5.11(a) the starting point of every curve at Z''=0 represents the bulk resistance (Rb) of the membrane (Costa, Nunes-Pereira, Sencadas, Silva, & Lanceros-Méndez, 2013; Song et al., 2015; D. Wu et al., 2015; Xiao et al., 2014; Yanilmaz, Zhu, Lu, Ge, & Zhang). It is a general practice to evaluate ionic conductivity (σ) through the Rb values by using the following relation:

$$\sigma = \frac{t}{A \times R_b} \tag{5.1}$$

where A is the area of the membrane and t is the thickness. The intrinsic resistance of the membrane is very high owing to the polymeric nature of the PVDF (ranging in various kΩ); however, a significant reduction in the resistance is observed once the electrolyte is added as shown in Table 1. Q.-Y. Wu et al has reported the resistance of 153.8 ± 5.8 μm thick PVDF membrane to be 2.3 ± 0.2 Ω which is very closer to our 200 µm thick membrane i.e. 2.42 Ω(Q.-Y. Wu et al., 2016).

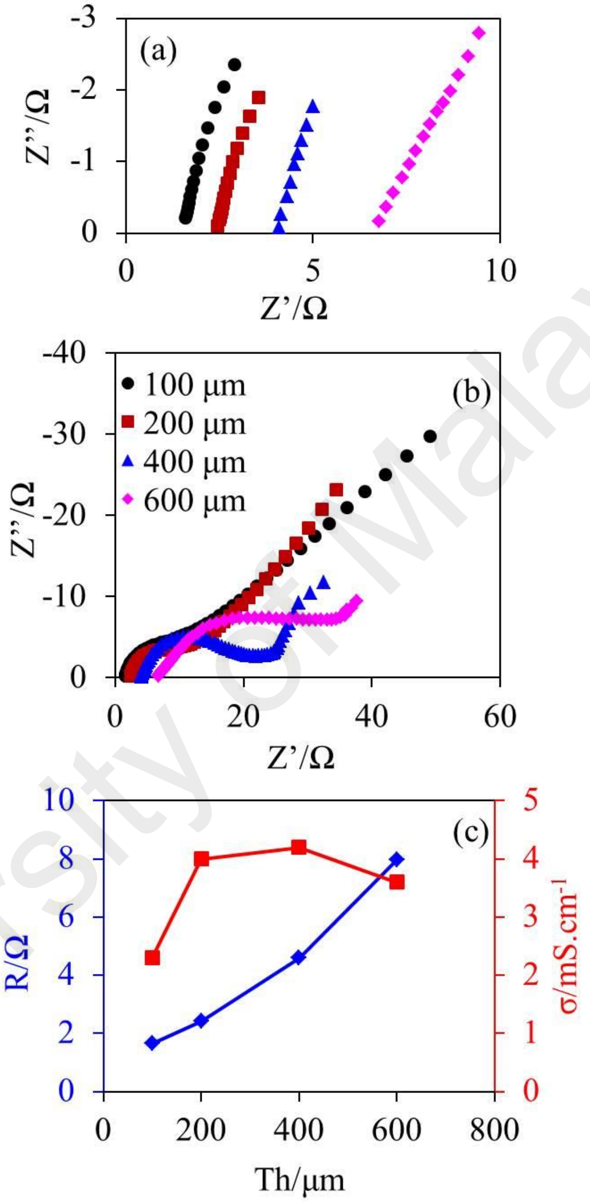

Figure 5.11: Nyquist Plot of MTECs with various membrane thickness

It is noteworthy that in both with and without electrolyte; the resistance increases with the increment of the thickness. The Table 5.1 illustrates a linear increment in the membrane resistance with thickness and the maximum resistance is observed for the thickest membrane. At this point, we can understand the reason of the reduced power density with the membrane thickness beyond 200 μm as indicated in section 3.2.1. In thicker membranes (i.e. 400 μm and 600 μm) the porosity is minimized and the redox species flowing across the membrane faces significantly high resistance. Thus the overall cell resistance is increased deteriorating the power density from 16.3 mW.m^{-2} (for 200 μm) to10.9 and 9.3 mW.m^{-2} for 400 μm and 600 μm thick membranes, respectively. The increasing trend in the conductivity (σ) of the membrane with increasing thickness is a normal phenomenon as observed for the 100 to 200 μm the conductivity increases from 2.3 to 4.0 mS.cm^{-1}. However, the change in conductivity is not significant by any further increment in the thickness (Table 5.1, Figure 5.11(c). Similar values for the ionic conductivities of PVDF membranes have been reported in the literature (Hakkak, Rafizadeh, Sarabi, & Yousefi, 2015; Zhiming Li et al., 2008). Thus the maximum power density of 16 mW.m^{-2} in 200 μm thick samples is justified by its optimal ionic conductivity and minimal cell resistance.

5.4 Discussion

In the previous section (5.3.2.1), we have noted that an increase in thickness results in a decrease in porosity and results in higher thermal resistivity of the thermocell, which is beneficial for the efficiency of the thermocell. On the other hand, from the ionic conductivity values of the membrane (section 5.3.2.2), we have identified that the optimized ionic conductivity was achieved for the case of membrane thickness of 200 μm. Thus, the final power density of the thermocell is a compromise between the porosity and membrane resistance, thus arriving at an optimal value of membrane thickness of 200 μm for this study. Although, our results (i.e. max. power density= 16.3 mW.m^{-2} and max. cell potential=16.7 mV) are not highest in the literature but still competitive with many recent reports. M. A. Lazar et al have shown that the power density of c.a. 800 mW.m^{-2} and cell potential of ca. 120 mV can be obtained by diluting the ionic liquids with organic solvents like 3-methoxypropionitrile (MPN) (Lazar et al., 2016). Similarly, J. He et al prepared composite electrolytes by diluting the ionic liquids with high boiling temperature solvents (e.g. Polycarbonate (PC) or Dimethyl Sulfoxide) obtaining cell potentials of ca. 60 mV, however, their power density was limited to maximum of ~ 8 mW.m^{-2} with IL:PC composites (He et al., 2016). In a recently published paper, J. Wu et al have studied a gel prepared by ferri/ferrocyanide electrolyte $K_3[Fe(CN)_6]/K_4[Fe(CN)_6]$ and reported the power density to be 1.6 mW.m^{-2} with the maximum cell potential of -30 mV (J. Wu, Black, & Aldous, 2016). Similarly, L. Jin et al have reported ca. 18 mW.m^{-2} and ~ 18 mV with their quasi-solid-state electrolytes (Jin, Greene, MacFarlane, & Pringle, 2016). P. Yang et al have prepared the gel capable of harvesting body temperature to generate electricity. They have reported the power output of ca. 18 nW with the maximum cell potential of ca. 25 mV at the temperature gradient of 10K (Yang et al., 2016).

5.5 Conclusion

The thermally driven electrochemical cells (TEC) convert the applied temperature gradient (ΔT) across electrodes, in redox-based electrolytes, into electricity. In this chapter the power generation characteristics of TEC, maintained at the ΔT of 45 K, was amplified by controlling the physical and electrical nature of the polymer membrane. The conductive membrane is prepared by trapping the solution of Iodide/triiodide (I^-/I_3^-) and 1-Butyl-3-methlyimidazolium Tetraflouroborate $[C_4mim][BF_4]$ in the mesoporous structure of poly(Vinylidene Fluoride) membranes. The intricate dependence of TEC performance on numerous thermophysical and electrical properties including thermal conductance, porosity, thickness and ionic resistance of the membrane has been identified. Higher thickness provides better thermal resistivity maintaining the TEC at high ΔT; however, this simultaneously reduces the porosity (limiting the redox reactions at the electrodes) and augmenting the membrane resistance. The 200 μm thick membrane is the sweet spot i.e. optimized ionic conductivity with appropriate porosity and cell resistance. Therefore, a compromise between high thermal gradient and availability of redox species at electrodes improves the maximum power density from 1.5 to 16.3 mW.m^{-2}.

Table 5.1: Relation between membrane physical parameters and power density of MTEC

Membrane Thickness	**Porosity**	**Sp. Pore Volume**	**Mx. Power Density**	**Membrane Resistance**	
(µm)	(%)	(cm$^{3.}$g^{-1})	(mW.m^{-2})	w/o electrolyte (kΩ)	with electrolyte (Ω)
100	71.4	0.06	2.5	0.1	1.65
200	67.9	0.03	16.3	0.104	2.42
400	59.9	0.02	10.9	20.2	4.59
600	45.8	0.02	9.3	56.8	7.96

CHAPTER 6:

THERMALLY RESISTIVE ELECTROSPUN COMPOSITE MEMBRANES FOR LOW GRADE THERMAL ENERGY HARVESTING

6.1 Introduction

The most important characteristic of the membrane separators for the MTECs (membrane thermocells) application is the thermal resistivity because higher is their thermal resistivity higher shall be the temperature gradient across the cell. Thus, identifying newer polymers which can offer maximum resistance to the heat flow within the cell is necessary to maintain non-isothermal state in MTECs. In addition of identifying newer materials, preparing membrane of composite polymers can be a great source to enhance thermal resistance as the composites generally possess higher thermal resistivity as compared to their individual constituents. Therefore, this chapter compares poly(Acrylonitrile) (PAN) membranes against the previously tested Poly(Vinylidene Fluoride) (PVDF) membranes, moreover, composites of PVDF/PAN are also investigated. The synthesis methodology also contributes significantly in the morphological and physical properties of the polymer membranes. In this chapter the comparison between the PVDF and PAN membranes prepared by phase inversion and electrospinning is also presented.

6.2 Methodology

6.2.1 Electrolyte Preparation

The 0.4M iodide/triiodide redox couple (I^-/I_3^-) is prepared in 1-Ethyl-3-Methylimidazolium Ethylsulfate [(Emim)(EtSO$_4$), from MERCK]. The solution is heated upto 120 ˚C for a complete dissolution of the Potassium iodine (KI, Sigma Aldrich) and Iodide ($I_{2,}$ Sigma Aldrich) powder following the addition of 0.2 mmol Acetonitrile (ACN,

C_2H_3N, b.p 81-82˚C, Sigma Aldrich 99.8%) in the solution. The solution was kept at 120 ˚C for next 24 hours and then allowed to cool down. The experiments are performed after 2-3 day of the preparation of the electrolyte.

6.2.2 Preparation of PVDF and PAN Electrospun Fibers

Poly(Vinylidene Fluoride) (PVDF, Kynar® K-761, Mw 440,000 $gmol^{-1}$) and poly(Acrylonitrile) (PAN, Sigma Aldrich, Mw 150,000 $gmol^{-1}$) are used to prepare the composite electrospun membranes. A 10 ml solution of PVDF powder (5 gm) in 1:1 ratio (by vol) of Acetone/DMF (N,N-Dimethylformamide Mw 73.1 $gmol^{-1}$) is prepared for PVDF electrospun membranes (Solution A). For the second solution (Solution B), the PAN powder (5 gm) is mixed in 10 mL of Dimethyl Sulfoxide (DMSO, Mw 78.13 $gmol^{-1}$). In order to prepare the nanocomposites the solutions A and B are mixed in 1:1, 1:2, and 1:3 before electrospinning process.

The nanofibers of PVDF and PAN are produced by electrospinning using a vertical arrangement. The distance between the needle and the collecting roller is maintained at 100 mm. The fiber morphology change is studied by jetting the polymer solution at the flowrate of 0.3mL/hr with 6.3 kV and 20 kV externally applied voltage. The rotating speed of the roller is maintained at 150 rpm while the electrospinning chamber is maintained at 60˚C to keep a dry environment and allowing the solvent to vaporize during the electrospinning process. For the composite membranes all of the parameters are maintained identically, however, owing to the increased density of the polymer solution by mixing solution A and B together, the electrospinning of the jet initiates from 10 kV (rather than 6.3 kV as in the case of pure polymer solutions). All membranes were prepared with the thickness of 200μm and allowed to dry properly before any further steps.

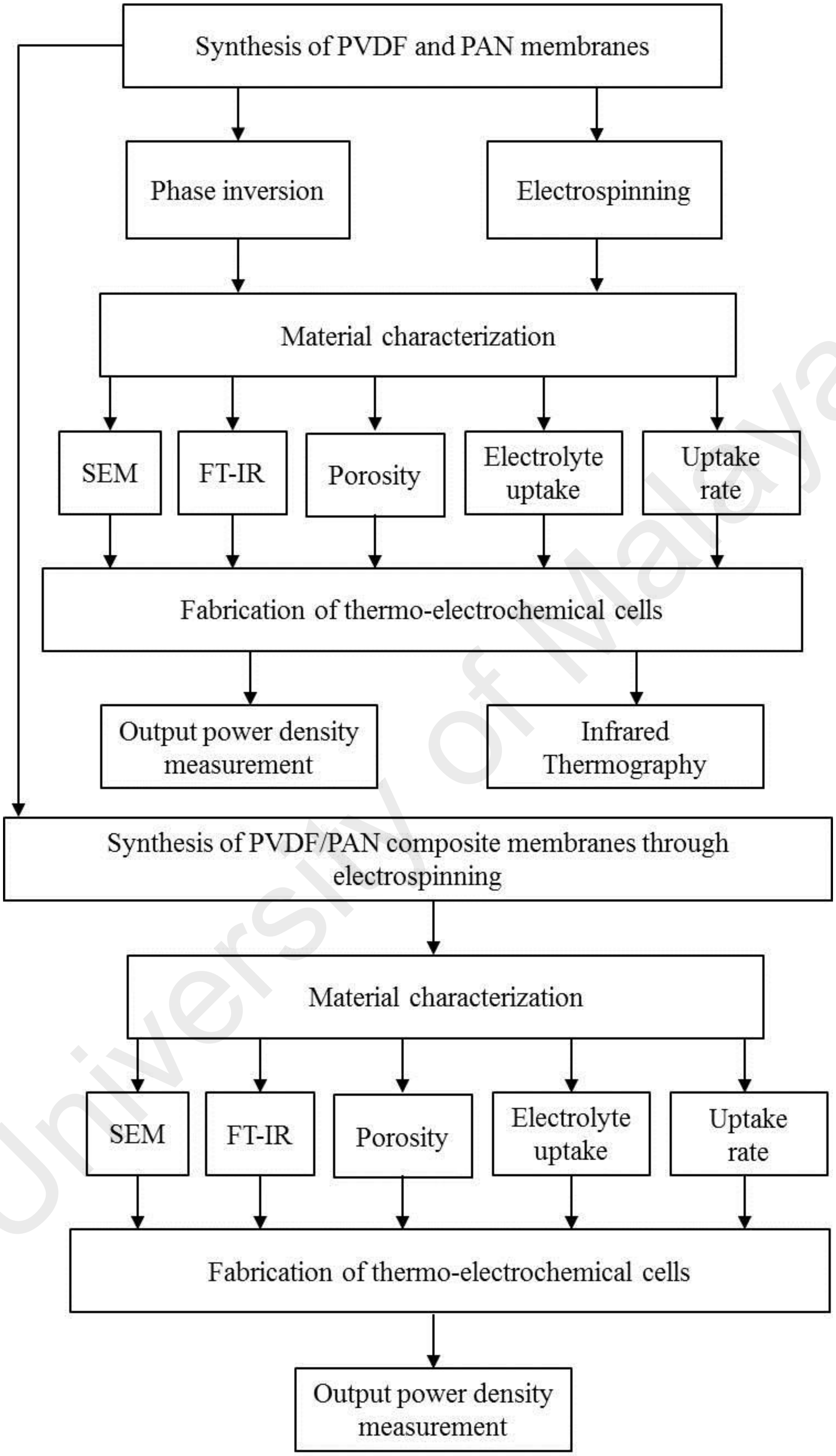

Figure 6.1: Flow-chart of the experimental methodology and results

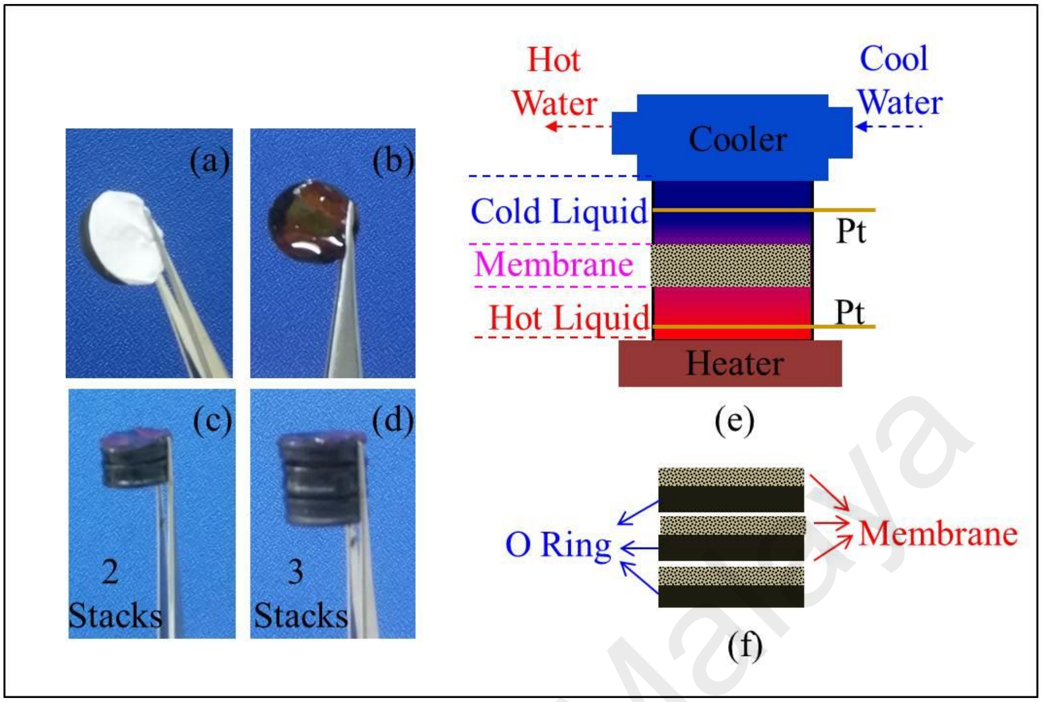

Figure 6.2: Schematic illustrations of electrospun membranes and thermocell device (a) monolayer membrane attached to O-ring before immersing it into the electrolyte (b) the monolayer membrane after immersing it into the electrolyte (c) bilayered membrane configuration (d) trilayered membrane stacking (e) schematic of membrane embedded thermocell (f) schematic of trilayer membrane architecture showing the membrane and the O-ring.

6.2.3 Fabrication of the thermocells

The fibrous membranes are cut in circular discs of 15 mm diameter. The membranes are attached to a thermoplastic O-ring followed by addition of the electrolyte. Later the gel assembly was placed in a 15mm thermocell barrel containing the 5mL of the (I^-/I_3^-):(Emim)($EtSO_4$) electrolyte solution. The Pt rod electrodes were submersed in (conc.) HNO_3 for 1 min and washed properly by Methanol and distilled water before any measurement. After inserting electrolyte, TEC and MTECs were left idle for 30 mins allowing open-circuit voltage to stabilize. The thermocell was heated in cold-above-hot arrangement maintaining a thermal gradient of 45 K. The bottom of the thermocell was kept at 70˚C while the top part was cooled by water circulation. The criteria to proceed in measurements was a constant ΔT of 45K (±1˚C) for 30 mins. Once the desired ΔT was achieved Pt electrodes were connected to a variable resistor box Elenco RS-500 to apply external loads (R; Ω). The potential drop (ΔV) across the electrodes was measured by Agilent 34461A 61/2 digital multimeter and power ($P=\Delta V^2/R$) was calculated by ohm's law as described in the literature. Corresponding resistances were applied keeping a time interval of 6 mins in between (5 mins to stabilize the cell potential and 1 min to record the potential values). The systematic flowchart of the experiments and the results is shown in Figure 6.1. The schematic of the thermocells are shown in Figure 6.2.

6.2.4 Materials Characterization

The Surface morphology of the pure and composite fibers is investigated through Scanning Electron Microscopy (SEM). The polymer structure of PVDF, PAN and composite membranes were investigated in the range of 450-4000 cm^{-1} on Fourier Transform Infrared Spectrum (FTIR). The electrochemical nature of the reduction-oxidation reactions of 0.4M electrolyte is studied through cyclic voltammetry at the scan rate of 100 mVs^{-1} using Platinum and Carbon as counter and working electrodes, respectively (Ref 600, Gamry Instruments). The contact angle on each of the membranes is measured using OCA15EC (Dataphysics) to analyse the hydrophobic nature of the fibers. Furthermore, the absorption rate of the electrolyte ($\mu L.s^{-1}$) in the membranes is measured by droping a 4μL of the electrolyte on the membrane surfaces and noting the time at which the whole drop is absorbed in the membrane.

6.3 Results

The phase inversion (PI) and electrospinning (ES) are two generally utilized processes to produce porous membranes and substantial literature for both of the techniques is available (Huang, Zhang, Kotaki, & Ramakrishna, 2003; Peng, Hu, & Fang, 2014; Pu et al., 2006). However, a comprehensive comparison between the two is relatively overlooked. The porosity of the membrane has a significant influence on the device performance as higher porosity enables higher electrolyte uptake in conventional batteries. Nevertheless, both phase inversion and electrospinning procedures can yield porosity upto 80 – 90% by engineering the process parameters. Herein, PVDF (Mw 440,000 gmol^{-1}) and PAN (Mw 150,000 gmol^{-1}) membranes were prepared using the two methods and compared for applications in thermo-electrochemical cells. The flat sheet PVDF and PAN PI membranes and electrospun PVDF and PAN fibrous mats are shown in Figure 6.3. The irregular pore size and inhomogenous pore density is normally observed in PI membranes as shown in Figure 6.3 (a) and (b). The electrospun membranes as shown in Figure 6.3 (c) and (d) are composed of nanosized fibers.

The electrospinning process has many dynamic factors which affects the morphology of the fibers. The impact of the applied electric field on the morphology by varying from 6 to 20 kV was investigated and the SEM micrographs are presented in the inset of Figure 6.3 (c and d). At lower applied electric fields (i.e. 6 kV), for both of the polymers nanofibers are obtained irrespective of their molecular weights. For PVDF fibers smooth and homogeneous fibers of ca. 500 nm diameters are prepared, however, for PAN the diameter of the fibers are further reduced to ca. 200 nm and smoothness and homogeneity is further enhanced. Here the impact of the lower molecular weight of the PAN can be witnessed. Once the electrospinning is carried out at higher applied voltages (20 kV) non-uniformity, inhomogeneity and surface defects (e.g. beads) are observed in both polymers. Although, no beads are formed in PVDF even at 20 kV but the diameters of the fibers lie in the wide range of 1200 to 400 nm (i.e. the homogeneity is disturbed). Similarly, for the case of PAN the higher electric field not only increases the diameters to ca. 300 nm but also beads are present and the smoothness of the fibers is also lost. If the comparison is made on the basis of applied voltage (omitting the effect of molecular weight) for respective PVDF and PAN case at 6 and 20 kV, it can be concluded that smaller diameters are produced when the applied voltage is less and the diameters increase as the electric field is increased (Zhenyu Li & Wang, 2013). Similarly, decreasing the molecular weight decreases the diameters of fibers irrespective of the applied voltage. The morphology of the membrane has the direct effect on the electrolyte uptake and the ionic conductivity. As indicated in the Table 6.1 the porosity of electrospun mats is significantly higher than the PI flat sheet membranes. The ionic conductivity of the respective membranes illustrates that the ionic movement across the fibrous mats is significantly higher than the PI sheets. Due to the higher porosity and larger void volume between the fibrous structure it is more convenient for the electrolyte ions to flow as compared to the PI flat sheets. It is also noteworthy that the ionic conductivity of electrospun PVDF (i.e. 5.9 $mS.mm^{-1}$) is higher than 3.3 $mS.mm^{-1}$ that of PAN electrospun mat.

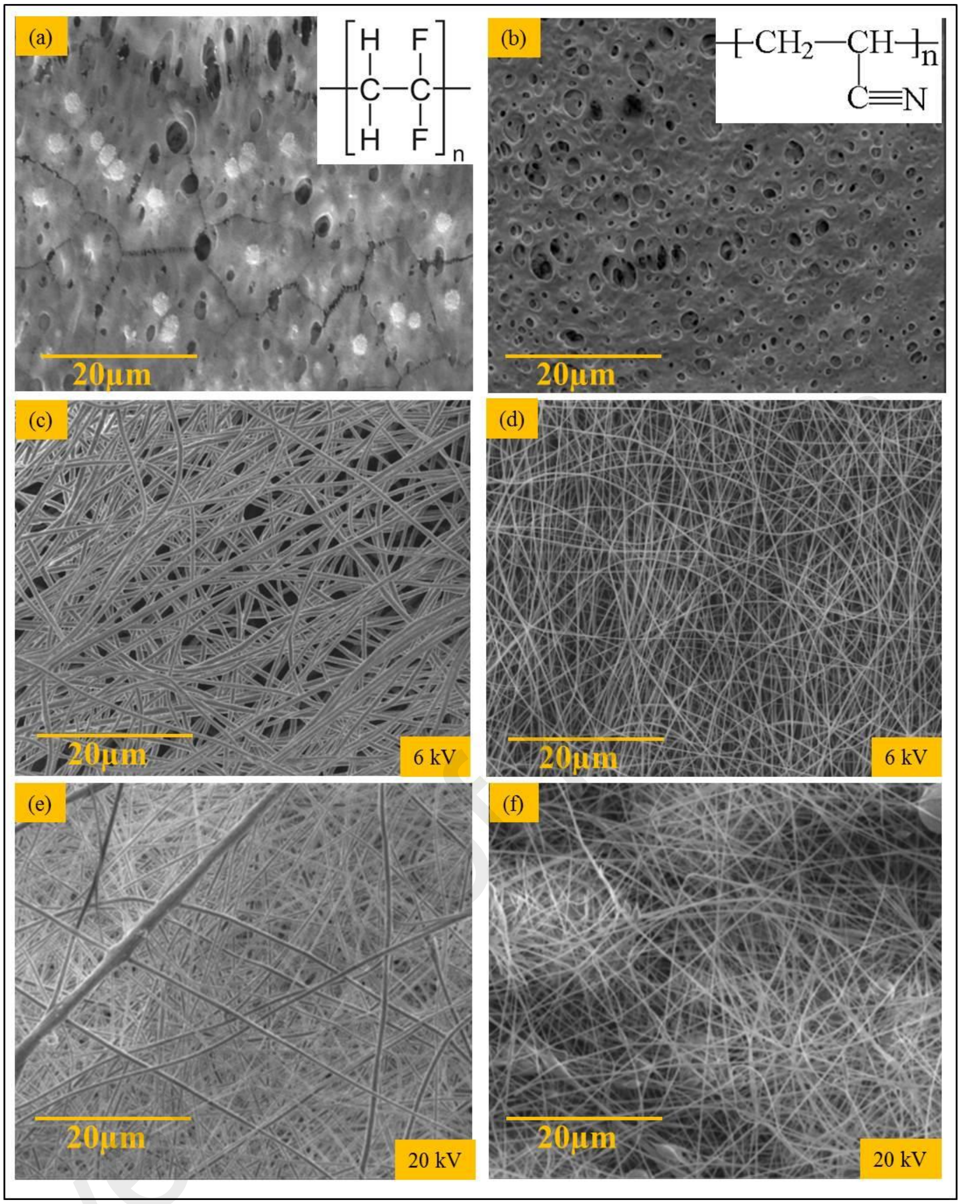

Figure 6.3: SEM micrographs of Phase inversion (PI) and Electrospinning (ES) membranes. (a) PVDF flat sheet prapered by PI (b) PAN flat sheet prepared by PI (c,d) Electrospun PVDF and PAN, respectively prepared at low voltage (6 kV) (e,f) Electrospun PVDF and PAN, respectively prepared at high voltage (20 kV). The inset of (a) and (b) shows the chemical structure of PVDF and PAN, respectively.

The Figure 6.4 is a conventional power density curve for thermocells. As described in previous reports (Hasan et al., 2016), the power density of a thermocell without a membrane is substantially low owing to rapid mass/heat transfer between the electrodes, due to convection of electrolyte subjecting the actual thermal gradient significantly minute as compared to the applied thermal gradient. Once a membrane is placed between the electrodes a distinct enhancement in the power density is witnessed. When temperature gradient (ΔT) of 45K is applied in the thermocell containing only the (I^-/I_3^-):(Emim)($EtSO_4$) electrolyte solution, the power generation is extremely minute i.e. the max. power density is ca. 2.2 mW.m^{-2} and the maximum cell potential is ca. 1.6 mV (Figure 6.4).

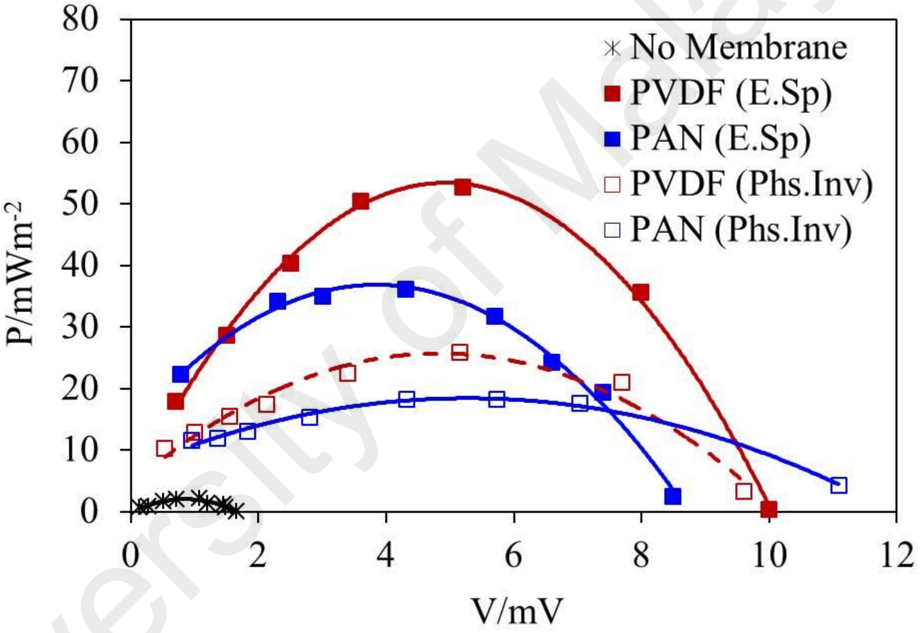

Figure 6.4: Comparison of MTECs with PI and ES membranes

The Figure 6.5 shows the infrared thermal image of the thermocell with two Pt rod electrodes assembled between the heating and cooling source. It is notable that although the thermocell was externally operated between 70˚C and 25˚C, however, the thermal images show the electrodes to be maintained at 70˚C and 42˚C reducing the ΔT from 45K (ideally) to 28K. This is the indicative of rapid heat flow within the thermocell reducing the temperature gradient i.e. the main reason of the diminished power density as the power generation is directly proportional to the actual ΔT. Nevertheless, the power generation is significantly enhanced once a membrane is added in the thermocells. The power density of PVDF and PAN containing thermocells is 52.1 and 36.1 mW.m^{-2}, respectively. Furthermore, the maximum cell potentials are also increased from 1.6 mV (for without membrane) to 6.7 mV for PAN and 10 mV for PVDF. The Figure 6.5 (b) and (c) are the infrared thermal images for PVDF and PAN separators embedded thermocells. It is noteworthy that, unlike in the previous membrane-less case, the cell containing either PVDF or PAN is well divided into two distinct temperature zones improving the thermal gradient. We can see that hotter electrode is now at 72˚C while the temperature of the colder electrode is maintained at 35˚C keeping the ΔT actual at 37K which is relatively closer to the applied ΔT of 45K. Comparing the performance of membranes prepared with phase inversion and electrospinning: it is notable that for both PVDF and PAN, electrospun membranes result in higher power density as compared to PI memrbanes. The power density of electrospun PVDF and PAN is 52.1 mWm^{-2} and 36.1 mWm^{-2}, respectively whereas the maximum power density of PI membranes is limited to 25.9 mWm^{-2} and 18.3 mWm^{-2} for PVDF and PAN, respectively. Another interesting point is that PVDF membranes, irrespective of the synthesis route, perform better than PAN membranes. The electrolyte uptake of the respective membranes plays a significant role in the thermocell performance. The electrospun membranes, which have higher performance simultaneously is capable of holding additional amount of electrolyte as compared to the PI membranes as shown in Table 6.1. The Table 6.1 shows that the electrolyte uptake for PVDF goes upto 434% for electrospun membranes which is 31% higher than the PI PVDF. Similarly, the difference between the electrolyte uptake of ES and PI PAN is 650%; however, the power density is not highest with PAN electrospun which will be further elaborated as the discussion proceeds.

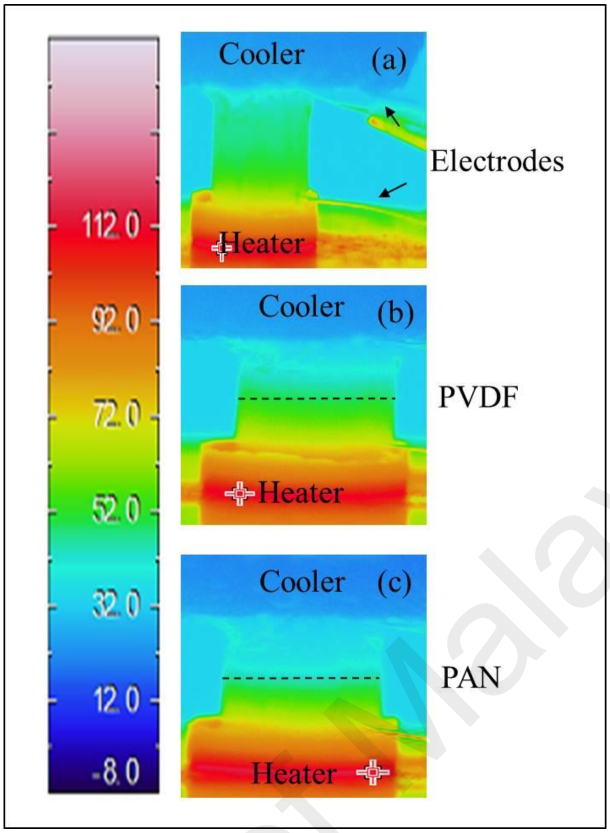

Figure 6.5: Infrared thermography images of MTECs containing PVDF and PAN electrospuns

The performance of a thermocell is directly integrated with the veracity of the actual thermal gradient between the two electrodes. Although, the embedded PVDF electrospun membrane improves the thermal gradient but in order to further extend the power density; more thermal resistive membranes are desired. Herein, PVDF/PAN composite membranes are also tested for thermocell performance. Three composite electrospun membranes are prepared by mixing the PVDF solution with PAN solution in the ratio of 25:75, 50:50, and 75:25 by volume and the SEM micrographs are shown in Figure 6.6. In Figure 6.6 (a) and (b), the SEM micrographs of pure PVDF and PAN prepared with the electrospinning voltage of 6 kV are shown. Since the composite solutions had slightly higher viscosity, there was no electrospinning jet at 6 kV, therefore, the applied voltage was increased to 10 kV and the respective SEM micrographs are shown in Figure 6.6 (c-e).

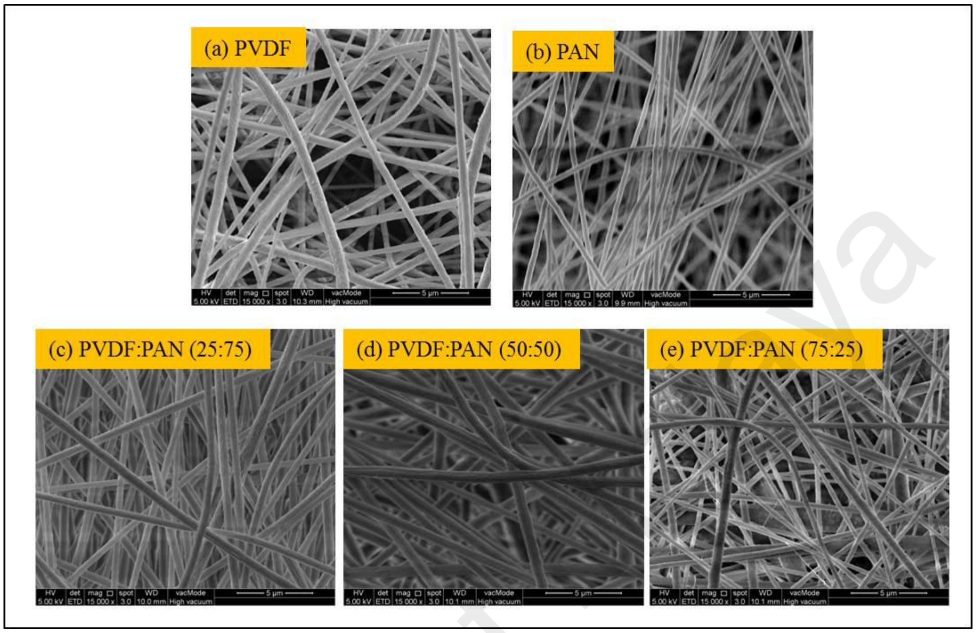

Figure 6.6: SEM micrographs of Electrospun PVDF/PAN composite membranes

An immediate impact of the composite can be noticed in the diameter of the fibers. The average diameter for the pure PVDF was noted to be 500 nm, once 25% (by volume) PAN is added in the PVDF the average diameter of the 75:25 composite is increased to ca. 520 nm. Similarly, when 25% (by volume) PVDF is added in PAN, the average fibrous diameter increases (from 300 nm for pure PAN) to 694 nm which further increases to ca. 770 nm upon making the 50:50 (by volume) PVDF/PAN composite.

The composite membranes were soaked in the (I^{-}/I_{3}^{-}):(Emim)(EtSO$_4$) electrolyte solution before deploying them into the thermocells. The power generation characteristics of the composites are represented in Figure 6.7(a). The maximum power densities are slightly improved to 57.1, 63.5 and 52.1 for 25:75, 50:50 and 75:25 respectively. Additionally, the cell potential of the thermocells containing the composites is enhanced from 10 mV to ca. 15 mV. Hence the maximum power density in composites is attained at the cell potential of 8.1 mV rather than 5.2 mV in the case of pure PVDF. Another interesting point to note is that the internal resistance of the cell, represented by the first point of each curve shown in Figure 6.7(a). The starting point for the PVDF and PAN membrane is (0.7 mV, 18 mW.m^{-2}) which is shifted to (1.5 mV, 28.7 mW.m^{-2}) for composites indicating higher internal resistance of the composite membranes.

Table 6.1: Summary of the membrane parameters comparing the flat sheet membranes prepared with phase inversion (PI) with the electrospun mats (ES)

Membrane	**Power Density (mW.m-2)**	**Porosity (%)**	**Electrolyte uptake (%)**	**Ionic conductivity (mS.mm^{-1})**
PVDF PI	25.9	74.8	298	0.8
PAN PI	18.2	66.2	300	0.86
PVDF	52.1	81.3	434	5.9
PAN	32.7	87.4	950	3.3
COMPOSITE (50:50)	63.5	85.4	583	3.2
COMPOSITE (25:75)	57.1	84.5	547	2.6
COMPOSITE (75:25)	52.1	82.9	489	2.3

The explanation of the performance of the thermocells with the composite membranes is an intricate relationship between the porosity, electrolyte uptake, electrolyte uptake rate of the membranes and the actual temperature gradient at the electrode surface. These parameters are summarized in Table 6.1 for respective membranes. The electrolyte uptake rate represents the convenience of the electrolyte transport within the membrane. Higher uptake rate indicates that the electrolyte can easily pass through the membrane.

For the thermocell performance, the convection within the electrolyte should be minimized as it enhances the heat transport within the cell diminishing the thermal gradient. It is notable that the porosity, electrolyte uptake and the electrolyte uptake rate for electrospun PAN, i.e. 87.4%, 950% and 0.56µLs^{-1} respectively, is highest as compared with other membranes. It is understandable that the membrane with highest porosity will absorb greater amount of the electrolyte and the electrolyte uptake rate will simultaneously be quicker. Similarly, the PVDF electrospun has the lowest porosity of 81.3% and consequently it has lower electrolyte uptake of 434% and very sluggish electrolyte uptake rate of 0.13 µLs^{-1}. For the case of composite membranes the magnitude of each of the parameters lies between the pure PVDF and PAN electrospuns. The average values of porosity, electrolyte uptake and the electrolyte uptake rate of composite membranes are ca. 84%, 540% and ~0.36 µLs^{-1}. The lowest power density for the membrane thermocells is obtained for PAN membranes owing to the quick electrolyte uptake rate as the convective flow in the cell will be increased. Although the convective flow would be minimum in the case of PVDF as the electrolyte uptake rate is minimum, however, the power density is maximum with the composite membranes. This can be explained by the improved thermal gradient between the electrodes when the composite membranes are embedded in the thermocells.

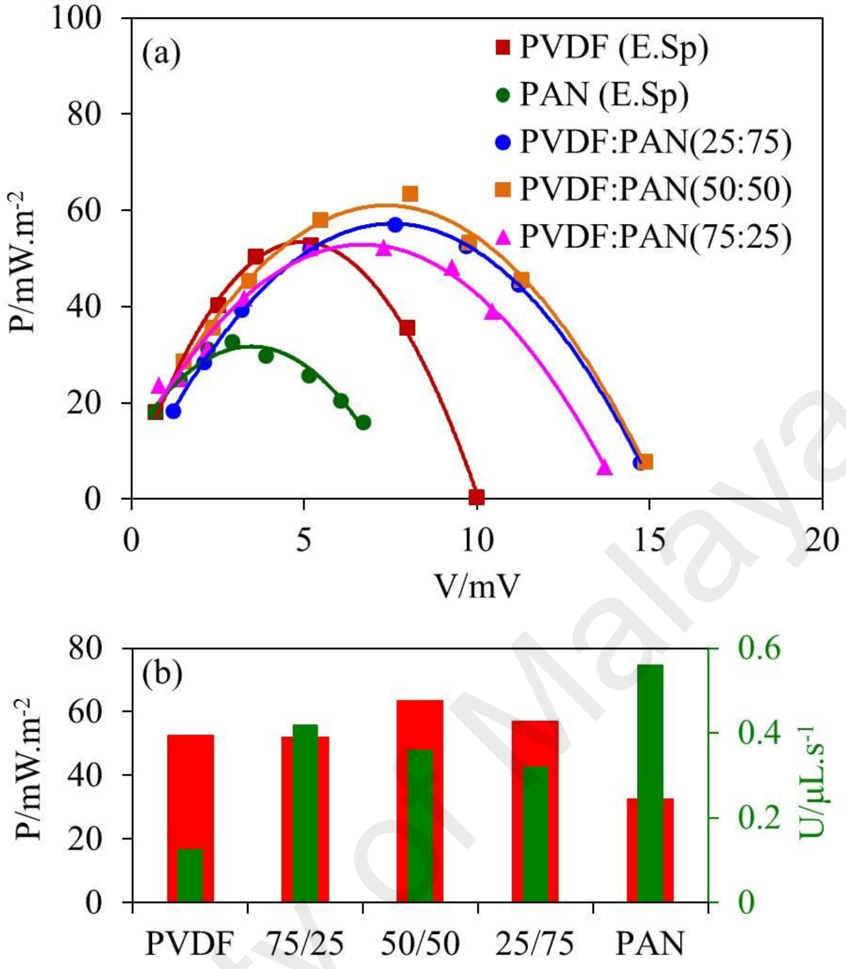

Figure 6.7: Power generation of MTEC containing composite membranes

In order to calculate the actual thermal gradient between the electrodes by using $\Delta T_{act} = \Delta V/S_e$ where ΔT_{act}, ΔV and S_e are actual temperature gradient, open circuit voltage and electrochemical Seebeck coefficient. The S_e of the (I^-/I_3^-):(EMIM)($EtSO_4$) electrolyte is evaluated by a conventional two-beaker experiments. The values of ΔT_{act} of each membrane are mentioned in the Table 6.2. It can be noted that although PVDF electrospun has minimum convective flow, however, the actual temperature gradient is 27.5 K which is better than the membrane-less thermocells but still very low as compared to the applied thermal gradient of 45 K. Nevertheless, the ΔT_{act} in the thermocells containing composite membranes is relatively closer to the applied ΔT. The composite membrane with the highest power density is 50:50 which simultaneously has the highest ΔT_{act} of 41 K which is very close to the applied ΔT. Similarly, the composites 25:75 and 75:25 which have power density of 57.1 and 52.1 mW.m^{-2}, respectively have the ΔT_{act} of 41 K and 37.8 K.

Table 6.2: Evaluation of the actual electrode temperature (ΔT_{act}) in thermocells with each membrane

Membrane	Electrochemical Seebeck (mV.K^{-1})	ΔTact (K)
PVDF	0.36	27.5
PAN		18.5
COMPOSITE (50:50)		40.9
COMPOSITE (25:75)		40.7
COMPOSITE (75:25)		37.8

Since embedding a monolayer polymer membrane enhances the power density of the thermocells, it is interesting to study the thermocell performance with multi-layered membrane stacking. It is noteworthy that a thermocell stacked with two layers of the 50:50 composite membrane has resulted in a highly significant improvement in the power density from 63.5 mW.m^{-2} (for the case of single membrane layer) to 102 mW.m^{-2} (Figure 6.8). However, the cell potential did not change as the effect of stacking and the maximum cell potential is limited to ca. 15 mV. In order to obtain the maximum attainable open circuit voltage of the (I^-/I_3^-):(EMIM)($EtSO_4$) electrolyte solution at ΔT of 45 K, we conducted the two-beaker experiment was conducted and found that the maximum open circuit voltage is limited to ca. 16.5 mV. Therefore, the maximum cell potential of the stack thermocells is limited to 15 mV which is very close to the maximum possible cell potential at this temperature gradient. It is important to note that the bilayered structure as discussed here is different from the thick membranes as discussed in the chapter 5. In present scenario, although each of the membrane layers is 200 µm and the two layers will make the overall thickness as 400 µm but it is important to note that between the two layers of membranes there is an 0.25 mm thick hollow O-ring. This O-ring provides a volume of 0.5ml solution of the electrolyte. The experimental results show that the ionic and thermal flow within the thermocells are optimized with the bilayered configuration. Another notable point with respect to stacked membrane in thermocells is that the performance is not linear i.e. the maximum power density of the stack thermocell with trilayer membrane is significantly reduced from 102 mW.m^{-2} to 15.5 mW.m^{-2}. The power density of trilayer membrane stacking is even lesser than the monolayer system. This is an indicative of the enhanced ohmic resistance in the cell because of the 3 layers of the membrane. The ionic resistances of monolayer, bilayer and trilayer thermocells as measured through electrochemical impedance spectroscopy are 66.8Ω, 72.7Ω and 84.31Ω.

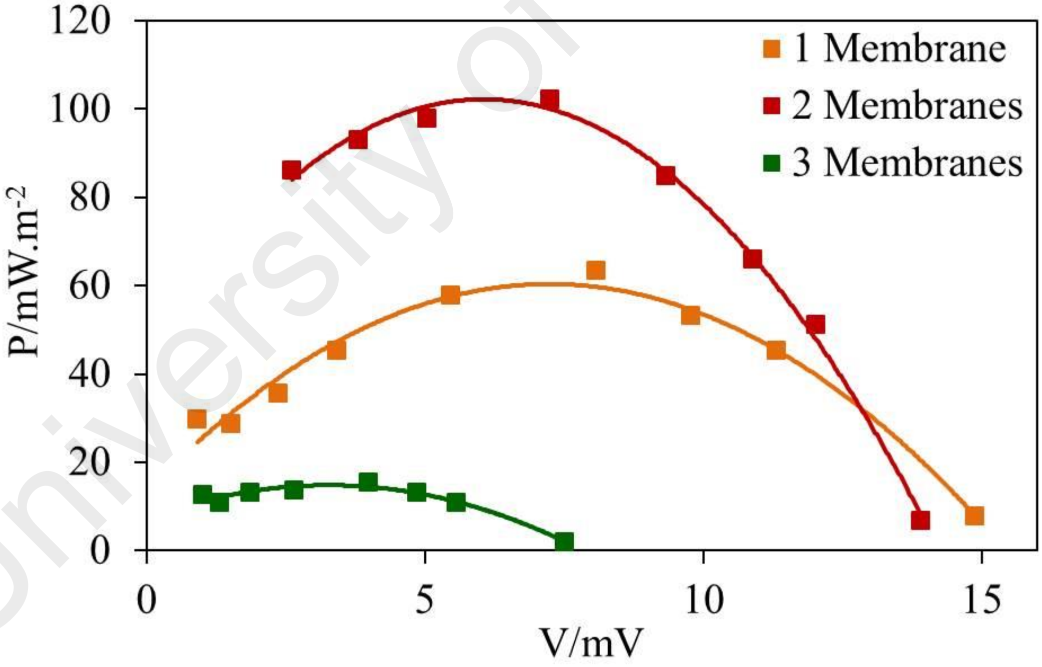

Figure 6.8: Power generation characteristics of stack MTECs

Although, the trilayer membrane may improve the thermal gradient across the cell but it simultaneously increases the ohmic resistance diminishing the effect of thermal gradient pinning down the power density. Although our results (i.e. max. power density = 16.3 mWm^{-2} and max. cell potential = 16.7 mV) are not highest in the literature but still competitive with many recent reports, Lazar et al. have shown that the power density of ca. 800 mWm^{-2} and cell potential of ca. 120 mV can be obtained by diluting the ionic liquids with organic solvents like 3-methoxypropionitrile (MPN). Similarly, He et al. prepared composite electrolytes by diluting the ionic liquids with high boiling temperature solvents (e.g. polycarbonate (PC) or dimethyl sulfoxide) obtaining cell potentials of ca. 60 mV; however, their power density was limited to maximum of 8 mWm^{-2} with IL:PC composites (He et al., 2016).

6.4 Conclusion

In conclusion, nanocomposite mats of poly(vinylidene fluoride) (PVDF) and polyacrylonitrile (PAN) are used as the separator membranes with highly ionic conductive and thermally insulating nature. The membranes improve the thermal-to-electrical energy conversion efficiency of a thermally driven electrochemical cell (i.e. thermocell) upto 95%. The justification of the improved performance is an intricate relationship between the porosity, electrolyte uptake, electrolyte uptake rate of the electrospun fibrous mat and the actual temperature gradient at the electrode surface. When the porosity is too high (87%) in PAN membranes the electrolyte uptake and electrolyte uptake rate are significantly high as 950% and 0.53 µLs^{-1}, respectively. In such a case, the convective heat flow within the cell is high and the power density is limited to 32.7 mW.m^{-2}. When the porosity is lesser (upto 81%) in PVDF membranes the electrolyte uptake and spread rate are relatively low as 434% and 0.13 µLs^{-1}, respectively. In this case, although the convective flows shall be low, however, the maximum power density of 63.5 mW.m^{-2} is obtained with PVDF/PAN composites as the aforementioned parameters are optimized. In addition, multilayered membrane structures are also investigated for which a bilayered architecture produces highest output power density of 102.7 mW.m^{-2}.

CHAPTER 7:

EQUIVALENT CIRCUIT MODELS FOR MEMBRANE THERMOCELLS

7.1 Introduction

As discussed in the previous sections, it has been elaborated that the ionic transport of the electrolyte within the thermocell is a complex integration of ionic diffusion, migration, thermal diffusion and natural convection. The electrode kinetics, surface conditions of the electrode (porosity etc) and inherent properties of the electrolytes (dielectric nature, ionic resistivity etc) supplement the complexity for designing an efficient thermocell. In such a complex scenario, electrochemical impedance spectroscopy (EIS) can provide an equivalent electrical circuit model of the thermocell accounting for the kinetic as well as the diffusion processes undergoing within the cell during the electron transfer process. Since any device may have multiple resistive, capactive or inductive components the overall effect is defined as Impedance (Z, Ω). Impedance is the measure of the ability of a circuit to resist the flow of the electrical current. Electrochemical impedance is measured by subjecting the cell to AC potential (Eo) and measuring the output current (Io). Mathematically, the impedance can be expressed as follows:

$$Z = \frac{Et}{It} = \frac{EoSin(\omega t)}{IoSin(\omega t + \phi)} = Zo\frac{Sin(\omega t)}{Sin(\omega t + \phi)} \qquad (7.1)$$

where ω, t and ϕ is the radial frequency of the applied AC potential, time and the phase shift. Solving the above equation using Euler relationship the impedance can be expressed as:

$$Z(\omega) = Zo\exp\left(j\phi\right) = Zo\left(\cos\phi + j\sin\phi\right) \qquad (7.2)$$

From the above equation, it can be realized that the frequency-dependent impedance is categorized into real (cosϕ) and an imaginary component (jsinϕ) (Orazem & Tribollet, 2011). If the real part is plotted on x-axis and the imaginary part is plotted on y-axis, a 2-dimensional plot is obtained referred to as “Nyquist plot”. Each point on the Nyquist plot represents the impedance of the cell at particular frequency. The experimental Nyquist curve obtained from any device can be analyzed by fitting to an equivalent electrical circuit model. Most of the Nyquist curves can be explained by applying resistors, capacitors and inductors(Yuan, Song, Wang, & Zhang, 2010). However, for non-linear inhomogeneous conditions Warburg diffusion coefficents can be applied. The Warburg coefficient expresses the diffusion of the ions in the solution. Generally, for low viscous solutions the ionic diffusion is considerably high while for the viscous solutions the diffusion coefficient is minimal.

For electrochemical cells certain parameters have been recognized contributing to the overall impedance. Foremost is the electrolyte resistance i.e. the retarding effect of the intermolecular species of the electrolyte towards the flow of current between the respective electrodes. The ionic resistance depends upon the electrolyte temperature, solution concentration and geometry of the conduit in which current is carried. The resistance is defined as:

$$R = \rho \frac{l}{A} \tag{7.3}$$

where ρ is the resistivity of the electrolyte, l and A are the length and the area of the current flow. For a precise resistance evaluation, the true area through which the current flows is desired and since the current flow has often non-uniform distribution it is an important aspect to address. Fortunately, by fitting the EIS data with electrical model the electrolyte resistance can be evaluated without figuring out the true area.

In addition to the ionic resistance offered by the electrolyte, the ionic layer of the electrolyte adsorbed on the electrode surface (which is normally few Angstrom thick) contributes in the overall impedance by behaving as double layer capacitor. And this capacitance effect depends on the temperature, ionic nature, electrode roughness, oxide layers and impurity adsorption etc. In real time applications, the capacitors in EIS experiments often do not behave ideally, therefore, it generally is replaced by a constant phase element (CPE) accounting for the leakage within the capacitor. Thicker is the adsorbed layer sluggish is the electron transfer between the electrode/electrolyte interface. At the electrolyte/electrode interface of thermocells the hot electrode (absorbs) the electron from the electrolyte while the cathode induces the electron into the electrolyte. This kinetically-controlled charge transfer has a certain speed which also depends upon the temperature, the concentration of the reaction products and the potential. The sluggish charge transfer also contributes in the overall impedance of the cell, known as charge transfer resistance (Rct). Ionic diffusion within the cell also creates a frequency-dependent impedance effect generally referred as Warburg impedance (Taylor & Gileadi, 1995). At higher frequency the Warburg impedance is generally neglected as the diffusing reactants don’t have to move very far. Similarly, when the diffusion length is increased at lower frequencies the Warburg impedance is also prominent. The Warburg diffusion may further be classified into three kinds (i) infinite Warburg impedance when the diffusion layer has the infinite thickness, (ii) bounded Warburg impedance when the diffusion, unlike in the infinite Warburg diffusion, the diffusion occurs within a thin film (i.e. infinite Warburg impedance) and (iii) porous Warburg impedance accounting for the porous materials.

The Figure 7.1 shows the Nyquist plot of the electrochemical cell along with the equivalent electrical circuit.

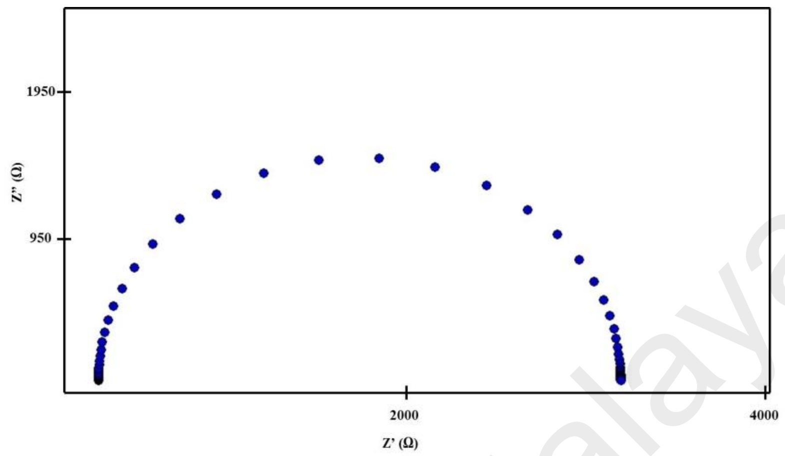

Figure 7.1: The Nyquist plot of a simple electrochemical cell

The semicircle observed shows that the resistive and capacitive nature co-exisits in this particular electrochemical cell. Furthermore, the semicircle does not emerges from the Z'=0 which is the indicative of the initial resistance offered by the electrolyte of the cell. Similarly, the maximum Z'=3.2 kΩ represents the charge transfer resistance (i.e. the resistance offered when the electrolyte absorbs an electron from the electrode or vice versa).

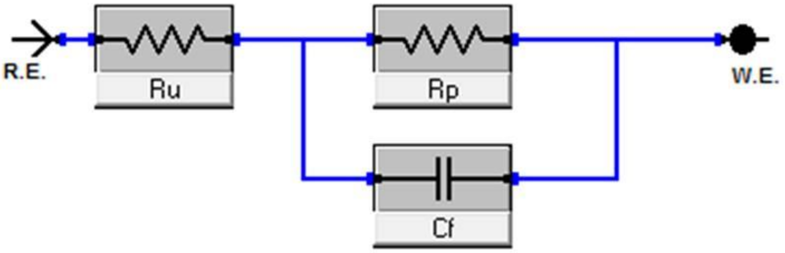

Figure 7.2: The equivalent electrical circuit of the electrochemical cell

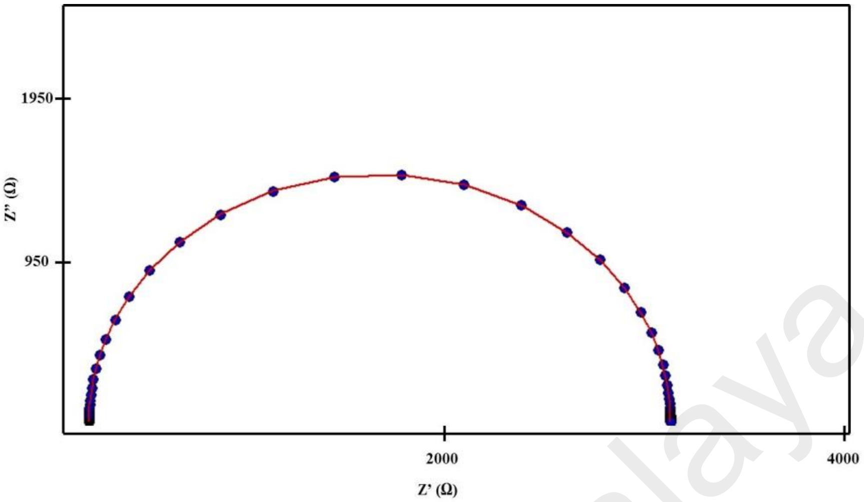

Figure 7.3: The fitting model of the Nyquist curve

In order to precisely estimate the elements present in the electrochemical cell an electrical model is prepared as shown in Figure 7.2 and the corresponding curve fitting is shown in the Figure 7.3. From the electrical model, it can be seen that Ru is the electrolyte resistance, Rp is the charge transfer resistance between the electrolyte/electrode interface and the Cf represents the capacitive nature of the electrolyte. Another useful attribute of the EIS curve models is to evaluate the accurate numeric values of the corresponding elements. For example, for the discussed electrochemical cell Ru= 199.7±0.89 **Ω**, Rp=3e3 ±13.03Ω and Cf=980.2e-9±7.5e-9 F.

In the following section of this chapter, the thermocell and membrane-thermocell shall be investigated through electrochemical impedance spectroscopy and a suitable equivalent electrical model shall be proposed.

7.2 Models for Thermocells/Membrane Thermocells

The thermocells containing the composite electrolyte of redox based 1-ethyl-3methylimidazolium ethysulfate and the acetonitrile was subjected to the electrochemical impedance spectroscopy. The Pt rod electrodes (anode/cathode) were connected to the reference and working electrodes of the potentiostat work station. The cell was tested on a wide frequency range from 1 – 1MHz.

The EIS data of the thermocell with two Pt electrodes and the electrolyte (Redox+IL+ACN) is shown in Figure 7.4. It can be noticed that the cell has minimum to two time constants as represented by two depressed semicircles. Furthermore, the slope of the data at lower frequencies are the indicative of the diffusion processes taking place during the thermo-electrochemical process. The initial resistance (R1) expresses the electrolyte resistance i.e. 66.92±0.63 Ω followed by the electrodes' contribution. The R2 and R6 are the charge transfer resistances at the electrodes' surfaces. It is interesting to note that the numeric values of R2 and R6 are almost equal to each other i.e. 4.51±1.58 Ω and 4.45±1.08 Ω which may indicate the homogeneous nature of the electrodes also noticed by the cyclic voltammetry data as presented in Chapter 4. The figure 7.5 has the further numeric details of the circuit elements. In addition to the resistive effect, the electrodes' surface adsorb a layer of the electrolyte forming a double layer capacitive layer, thus C6 and C7 express the same phenomenon. It is noteworthy that the numeric value of C6 i.e. 12.28e-3F is significantly higher than the C7 value of 322.9e-6 F. Since the capacitive elements shows the magnitude of the charged species accumulated at the electrode surface the higher value of C6 means that the charged species accumulated at that electrode is higher than the charged species gathered at C7 electrode. By the literature, it is known that generally the cathodic reactions within thermocells is sluggish as the temperature of the electrode is low, thus at boundary layer formed on the cathode is always thicker and more resistive for the electron transfer. Therefore, it can by concluded that the elements R2 and C6 are representing Cathode while R6 and C7 are representatives of anode. Since the anode is at higher temperature and the density of the electrolyte is less the charge accumulation is minor as compared to the cathode.

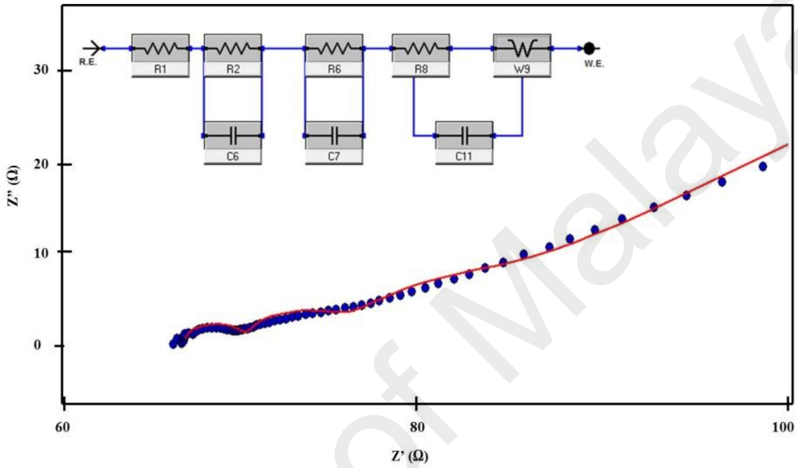

Figure 7.4: EIS data of thermocell containing the electrolyte without a membrane

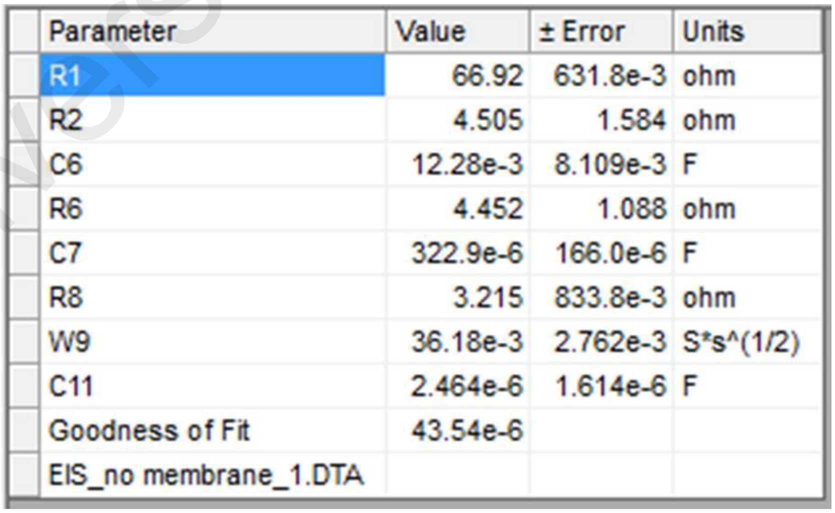

Parameter	Value	± Error	Units
R1	66.92	631.8e-3	ohm
R2	4.505	1.584	ohm
C6	12.28e-3	8.109e-3	F
R6	4.452	1.088	ohm
C7	322.9e-6	166.0e-6	F
R8	3.215	833.8e-3	ohm
W9	36.18e-3	2.762e-3	S*s^(1/2)
C11	2.464e-6	1.614e-6	F
Goodness of Fit	43.54e-6		
EIS_no membrane_1.DTA			

Figure 7.5. The numeric values of the electrical elements used to fit the EIS data of thermocell

After the two time constants, the experimental data shows as a slope with an increasing Z’ with respect to Z’’. Generally, this is regarded as the ionic diffusion of the species between the electrodes. Since the electrode to electrode separation is 10 mm, therefore, infinite Warburg impedance is implemented in the circuit. In addition to the Warburg impedance, it is necessary to incorporate a resistive as well as a capacitive element for the electrolyte representation because in the absence of the resistor (R8) and capacitor (C11), the fitting does not follow the experimental data as shown in Figure 7.6. The inset of the Figure 7.6 shows the electrical circuit without the resistor (R11) and the capacitor (C11). The absence of the R8 and C11 results in the deviation of the fitting curve from the experimental data in both domains of high and low frequencies. The logical illustration of the capacitance and resistance present in the electrolyte is necessary.

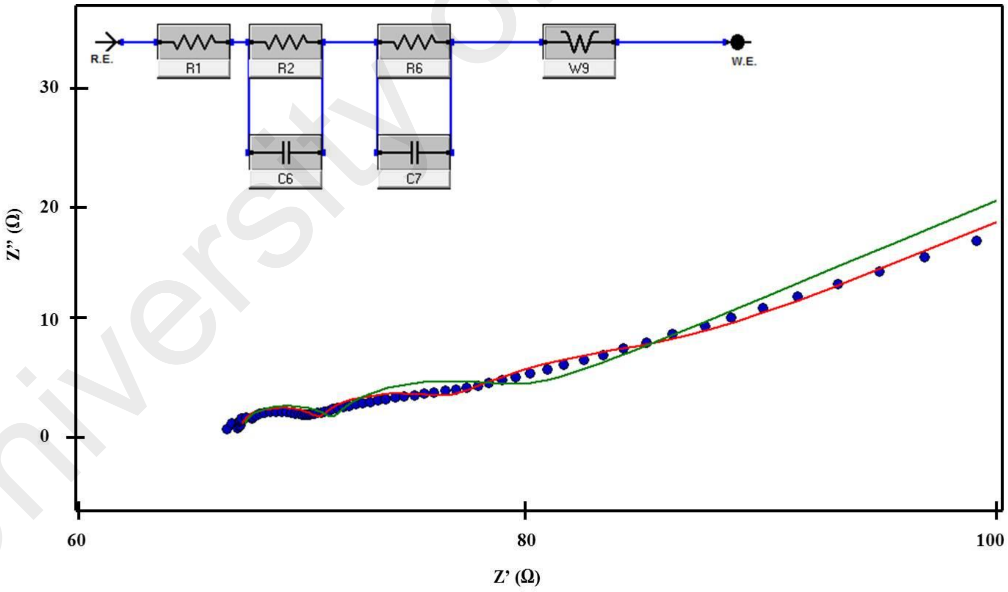

Figure 7.6: The Nyquist plot of the thermocell with equivalent electrical model without incorporating the resistance and capacitance effect within the electrolyte

A noteworthy point for the proposed model, as shown in the inset of Figure 7.4, is that it simultaneously satisfies the membrane-embedded thermocell EIS data. The Nyquist plot for the membrane-thermocell is shown in Figure 7.7 along with the fitting profile. The reason why the same model can be applied for the membrane thermocell is that the membrane itself does not incorporate any additional effect, rather its impact is automatically observed in the numeric values of the proposed model. The numeric values of the electrical elements of the model shown is Figure 7.4 is represented in Figure 7.8. It is notable that the membrane within the thermocell significantly enhances the initial resistance (R1) from 66.9 to 92.6 Ω. More interestingly the magnitudes of R2 and C6 are increased. The R2 and C6 can be attributed as the contribution of the Cathode, the reason of the increment can be easily understood i.e. the membrane terminates the heat flow across the thermocells maintaining the cathode at low temperatures. Thus at low temperature the density of the electrolyte is high, therefore, the resistance and capacitance is simultaneously high. On the other hand, the R6 and C7 which are the contributions from the anode have their respective magnitudes lessen owing to the membrane. As described previously for the case of cathode, the membrane maintains the anode electrolyte at higher temperature improving the electron transfer. Another important aspect noted as the impact of the membrane is the reduction in the Warburg diffusion impedance. It has been described that the mitigation of natural convection within the thermocell is the result of the membrane placement. The decreased diffusion in the case of membrane thermocells also supports the provided discussion.

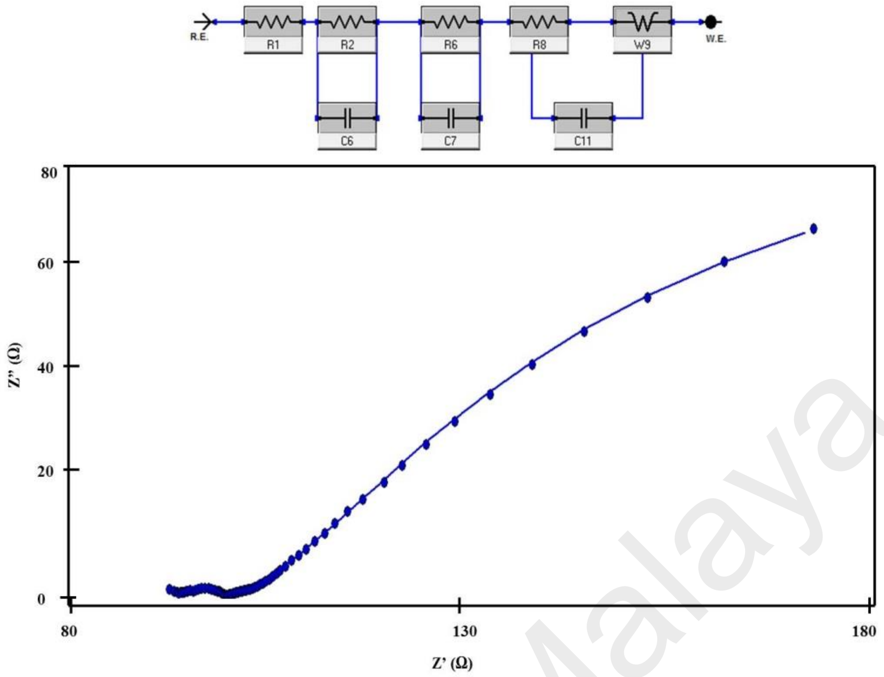

Figure 7.7: The Nyquist plot for membrane embedded thermocell along with the equivalent electrical model.

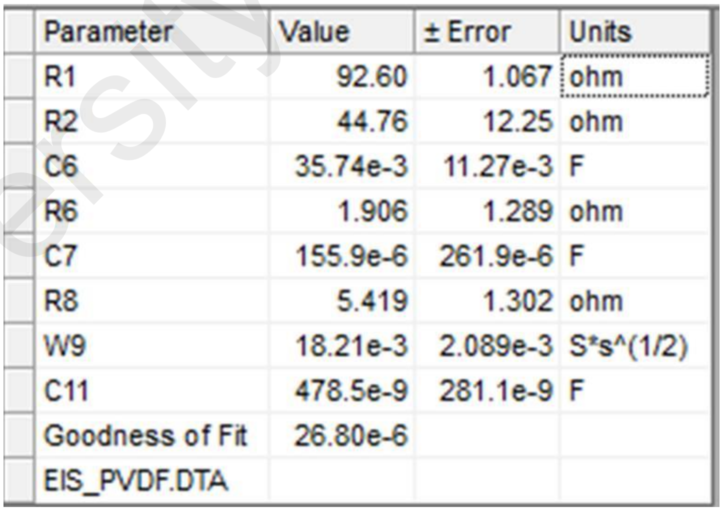

Parameter	Value	± Error	Units
R1	92.60	1.067	ohm
R2	44.76	12.25	ohm
C6	35.74e-3	11.27e-3	F
R6	1.906	1.289	ohm
C7	155.9e-6	261.9e-6	F
R8	5.419	1.302	ohm
W9	18.21e-3	2.089e-3	S*s^(1/2)
C11	478.5e-9	281.1e-9	F
Goodness of Fit	26.80e-6		
EIS_PVDF.DTA			

Figure 7.8: Numeric values of the electrical elements used in the proposed equivalent electrical model for membrane embedded thermocells

7.3 Conclusions

In this chapter the equivalent electrical circuits for the thermocells containing the [EMIM][EtSO$_4$] electrolyte are presented for both of the cases (i) without a membrane and (ii) with a membrane. Although, the electrochemical impedance spectroscopy (EIS) method implemented to evaluate the electrical circuit are not an exact way and a single EIS data can be fitted by multiple circuits and the single model which satisfies the theory of the device should be selected.

The electrical model selected for our thermocells show good fitting and acceptable error with the EIS data. The electrical model as shown in Figure 7.5 and Figure 7.7 shows that the electrolyte which contains (i) redox couple, (ii) [EMIM][EtSO$_4$] ionic liquid and (iii) acetonitrile (ACN) can be explained by a resistor, capacitor and the Warburg coefficient. It is necessary to connect the resistor with the Warburg coefficient in series and keeping the capacitor in parallel to the resistor and Warburg element. The resistor (R8) represents the resistance faced by the ions carrying the electron from anode to cathode (or vice versa) because of the intermolecular collisions. The effect of the capacitor is incorporated in the circuit as the electrolyte is mainly composed by the ionic liquid 1-ethyl-3-methylimidazolium ethylsulfate i.e. [EMIM][EtSO$_4$]. And finally, the Warburg coefficient is implemented to account for the ionic diffusions taking place within the cell owing to the applied thermal gradient. In fact for the case of membrane embedded thermocells, no additional electrical element or arrangement is desired as the EIS data for the membrane thermocells is satisfactorily fitted by the same circuit. The reason can be that the membrane used has the dielectric nature and its presence can be sufficiently described by a resistor, capacitor and the Warburg coefficient.

CHAPTER 8: CONCLUSIONS & RECOMMENDATIONS

This dissertation is based on the experimental research work focusing the role of a porous polymer membrane in thermo-electrochemical cells (or thermally driven electrochemical cells). Although, each chapter ends with a conclusive summary but herein this chapter, all of the major findings shall be summarized.. The major spectrum of this experimental research is focused on the morphological, physical, electrical and thermal properties of the embodied membranes. Nevertheless, in addition to contributing towards the quantitative improvement in the thermocell efficiency, this work also explains the theoretical aspects of heat propagation in thermocells.

The experimental work of this research begins, as discussed in chapter 3, by investigating the electrochemical Seebeck coefficient in three electrolyte solutions which included water, 1-ethyl-3-methylimidazolium ethylsulfate [EMIM][EtSO$_4$] and 1-butyl-3-methylimidazolium tetraflouroborate [C$_4$mim][BF$_4$]. The results showed that the power generation is higher for the electrolyte which has lower diffusion coefficient, thus the performance of water based solutions was higher. However, the low volatility of the aqueous solutions, it is preferred to reduce the diffusion coefficient of [EMIM][EtSO$_4$] by diluting it with acetonitrile (ACN). In literature, it has been reported that by diluting the ionic liquids with polar solvents the power generation of the thermocells can be increased. But herein, the experimental results highlighted an important condition in this observation i.e. the power generation of the thermocells is only increased in the composite electrolytes if the polar solvent does not increase the thermal conductivity of the base electrolyte. In the results, it is found that although ionic conductivity and the electrochemical Seebeck coefficient of ACN-diluted-[EMIM][EtSO$_4$] was higher than the base ionic liquid but the power generation was lower as ACN-diluted-[EMIM][EtSO$_4$] simultaneously had higher thermal conductivity. Therefore, this conclusion gives an important selection criteria for the polar solvents i.e. the pair of the base ionic liquid and polar solvent should be selected in which the overall thermal conductivity of the composite electrolyte is lesser (or atleast equal) to the base ionic liquid.

In chapter 4, the influence of placing a porous PVDF membrane in thermocells was investigated. The maximum potential generated in response to the externally applied thermal gradient increased from 1.1 mV to 3.5 mV. Furthermore, the power generation also increased from 0.54 mWm^{-2} to 24.5 mWm^{-2}. In order to elucidate the results, a thermal resistive model of the membrane embedded thermocells (MTEC) supported by infrared thermographical images of the MTECs, is presented. The thermography shows that the thermal resistance across the cell has been significantly increased owing to the presence of the polymer membrane. This thermal hindrance offered by the membrane limits the heat flow across the cell and drives the cell closer to the applied thermal gradient. The applied thermal gradient across the cell was 10K but for the case of a membrane-less TEC, the actual temperature gradient between the electrodes was noted to be only 2.7K due to the rapid heat loss to the environment (from the electrode & cell body). However, the presence of the membrane preserves the cell at temperature gradient of 8.8K (which is very closer to the applied $\Delta T \sim 10K$).

Thus, the membrane within a thermocell acts as a thermal barrier for the heat carriers; however, the porous nature of the membrane allows the charged carrier to transfer from anode to cathode resulting in circuit current.

Once it was realized that the power generation characteristics of thermocells is improved owing to the PVDF membrane, the research was further expanded to comprehend the optimal physical and morphological parameters of the PVDF membranes. The motivation of the chapter 5 is to find the optimal thickness of the PVDF membrane which can provide the maximum ionic transfer while maintaining higher thermal gradients. It was noted that the cell performance is the function of the thickness of the membrane. Actually, the thickness of the phase inversion membranes has a great influence in the porosity of the membrane. For thicker membranes the porosity is less (45%) i.e. during the phase separation water molecules cannot penetrate the thick polymer layer very quickly. However, in case of thinner membranes water molecules penetrates the surface of the forming flat sheet; increasing the porosity upto 71%. In terms of power generation, it was noticed that the maximum power density of 16.3 mWm^{-2} was observed with a 200 µm thick membrane; in fact this thickness resulted as the threshold thickness for the optimum power generation. Either increasing or decreasing the thickness reduces the power density. This is because, in the thinner membranes, the thermal gradient is disturbed and for thicker membranes (>200µm) the ionic resistance offered by the membrane is so immense that it diminishes any power enhancement owing to the higher thermal gradient.

As the final segment of this experimental work, it is shown that the synthesis route pursued to obtain the membranes has significant impact on the thermocell performance. The comparison has been presented between the membranes prepared by phase inversion and electrospinning methods (which are two well established methods to prepare the polymer membranes). The electrospun membranes of PVDF, PAN and PVDF/PAN composites were prepared amongst which the maximum power density of 63.5 mWm^{-2} was obtained with the composite with 1:1 ratio of PVDF/PAN solutions. The power density is an intricate function of the membrane porosity, thermal resistance and the ionic conductivity. Moreover, the effect of the multilayer membranes in thermocells was also experienced. The bilayer membranes showed the maximum power density of 102 mWm^{-2}, however, with any further increment in the number of membrane layers the power density is reduced owing to the increased ionic resistance. This dissertation is complemented by proposing an equivalent electrical model representing the thermocells with and without membranes which is discussed in chapter 7. After completing this experimental research, several recommendations can be concluded which can lay the foundation for the future thermocell research. The recommendations are presented as follows:

1. An obvious understanding from this thesis is that the fibrous composite membranes are preferred over flat sheet pure polymer membranes. The research can further be extended to investigate newer composite materials. Additionally, inorganic fillers like SiO_2, Al_2O_3, TiO_2 and $BaTiO_3$ can be added in the polymer materials and observe the thermocell performance.
2. As the extension of the understanding the fundamental heat and mass transport, the bilayered architectures are the topic of interest. The ionic and thermal flow between the two membrane layers can be further investigated through thermography and electrochemical impedance spectroscopy.
3. Heterogeneous structures can be very interesting and promising topic of research. From the results of bilayered architectures, an interesting research query arises i.e. will the thermocell performance with a 200 µm thick membrane be the same if two membranes of 100 µm are placed over each other and assembled in the thermocell. It is important to note that the heterogeneous interfaces in solid-state thermoelectric materials behave completely different as their bulk samples. Thus, investigating the interfacial science and phenomenon between the membrane layers shall not only be

interesting for the fundamental science but it can also improve the overall cell efficiency.

REFERENCES

Abraham, T. J., MacFarlane, D. R., Baughman, R. H., Jin, L., Li, N., & Pringle, J. M. (2013). Towards ionic liquid-based thermoelectrochemical cells for the harvesting of thermal energy. *Electrochimica Acta, 113,* 87-93.

Abraham, T. J., MacFarlane, D. R., & Pringle, J. M. (2011). Seebeck coefficients in ionic liquids–prospects for thermo-electrochemical cells. *Chemical communications, 47*(22), 6260-6262.

Abraham, T. J., MacFarlane, D. R., & Pringle, J. M. (2013). High Seebeck coefficient redox ionic liquid electrolytes for thermal energy harvesting. *Energy & Environmental Science, 6*(9), 2639-2645.

Abraham, T. J., Tachikawa, N., MacFarlane, D. R., & Pringle, J. M. (2014). Investigation of the kinetic and mass transport limitations in thermoelectrochemical cells with different electrode materials. *Physical chemistry chemical physics, 16*(6), 2527-2532.

AlMarzooqi, F. A., Bilad, M., Mansoor, B., & Arafat, H. A. (2016). A comparative study of image analysis and porometry techniques for characterization of porous membranes. *Journal of Materials Science, 51*(4), 2017-2032.

Alzahrani, H. A., Black, J. J., Goonetilleke, D., Panchompoo, J., & Aldous, L. (2015). Combining thermogalvanic corrosion and thermogalvanic redox couples for improved electrochemical waste heat harvesting. *Electrochemistry Communications, 58*, 76-79.

Anari, E. H. B., Romano, M., Teh, W., Black, J., Jiang, E., Chen, J., . . . Aldous, L. (2016). Substituted ferrocenes and iodine as synergistic thermoelectrochemical heat harvesting redox couples in ionic liquids. *Chemical communications, 52*(4), 745-748.

Armand, M., Endres, F., MacFarlane, D. R., Ohno, H., & Scrosati, B. (2009). Ionic-liquid materials for the electrochemical challenges of the future. *Nature materials, 8*(8), 621-629.

Black, J. J., Murphy, T., Atkin, R., Dolan, A., & Aldous, L. (2016). The thermoelectrochemistry of lithium–glyme solvate ionic liquids: towards waste heat harvesting. *Physical chemistry chemical physics, 18*(30), 20768-20777.

Bonetti, M., Nakamae, S., Roger, M., & Guenoun, P. (2011). Huge Seebeck coefficients in nonaqueous electrolytes. *The Journal of chemical physics, 134*(11), 114513.

Burrows, B. (1975). *Redox thermogalvanic cells for direct energy conversion.* Paper presented at the Energy 10; Annual Intersociety Energy Conversion and Engineering Conference.

Burrows, B. (1976). Discharge behavior of redox thermogalvanic cells. *Journal of The Electrochemical Society, 123*(2), 154-159.

Camacho, L. M., Dumée, L., Zhang, J., Li, J.-d., Duke, M., Gomez, J., & Gray, S. (2013). Advances in membrane distillation for water desalination and purification applications. *Water, 5*(1), 94-196.

Chum, H. L., Fahlsing, R., & Jayadev, T. (1980). *Analysis of the application of thermogalvanic cells to the conversion of low grade heat to electricity*. Retrieved from

Costa, C. M., Nunes-Pereira, J., Sencadas, V., Silva, M. M., & Lanceros-Méndez, S. (2013). Effect of fiber orientation in gelled poly (vinylidene fluoride) electrospun membranes for Li-ion battery applications. *Journal of Materials Science, 48*(19), 6833-6840.

Cui, Z. Y., Du, C. H., Xu, Y. Y., Ji, G. L., & Zhu, B. K. (2008). Preparation of porous PVdF membrane via thermally induced phase separation using sulfolane. *Journal of Applied Polymer Science, 108*(1), 272-280.

Curcio, E., & Drioli, E. (2005). Membrane distillation and related operations—a review. *Separation and Purification Reviews, 34*(1), 35-86.

de Jesus Silva, A. J., Nascimento, C. R., & da Costa, M. F. (2016). Thermomechanical properties and long-term behavior evaluation of poly (vinylidene fluoride)(PVDF) exposed to bioethanol fuel under heating. *Journal of Materials Science, 51*(19), 9074-9094.

Demirel, Y. (2012). Energy, green energy and technology: Springer-Verlag London.

Dhumal, N. R., Kim, H. J., & Kiefer, J. (2011). Electronic structure and normal vibrations of the 1-ethyl-3-methylimidazolium ethyl sulfate ion pair. *The Journal of Physical Chemistry A, 115*(15), 3551-3558.

Dincer, I. (2000). Renewable energy and sustainable development: a crucial review. *Renewable and Sustainable Energy Reviews, 4*(2), 157-175.

Ejigu, A., Lovelock, K. R., Licence, P., & Walsh, D. A. (2011). Iodide/triiodide electrochemistry in ionic liquids: Effect of viscosity on mass transport, voltammetry and scanning electrochemical microscopy. *Electrochimica Acta, 56*(28), 10313-10320.

Gunawan, A., Li, H., Lin, C.-H., Buttry, D. A., Mujica, V., Taylor, R. A., . . . Phelan, P. E. (2014). The amplifying effect of natural convection on power generation of thermogalvanic cells. *International Journal of Heat and Mass Transfer, 78*, 423-434.

Gunawan, A., Lin, C.-H., Buttry, D. A., Mujica, V., Taylor, R. A., Prasher, R. S., & Phelan, P. E. (2013). Liquid thermoelectrics: review of recent and limited new data of thermogalvanic cell experiments. *Nanoscale and Microscale Thermophysical Engineering, 17*(4), 304-323.

Hakkak, F., Rafizadeh, M., Sarabi, A. A., & Yousefi, M. (2015). Optimization of ionic conductivity of electrospun polyacrylonitrile/poly (vinylidene fluoride)(PAN/PVdF) electrolyte using the response surface method (RSM). *Ionics, 21*(7), 1945-1957.

Hasan, S. W., Mun, H., Kim, S. I., Cho, J. Y., Roh, J. W., Yang, S., . . . Kim, S. W. (2013). Formation of dense pore structure by te addition in Bi 0.5 Sb 1.5 Te 3: an approach to minimize lattice thermal conductivity. *Journal of Nanomaterials, 2013*, 9.

Hasan, S. W., Said, S. M., Sabri, M. F. M., Bakar, A. S. A., Hashim, N. A., Hasnan, M. M. I. M., . . . MacFarlane, D. R. (2016). High Thermal Gradient in Thermo-electrochemical Cells by Insertion of a Poly (Vinylidene Fluoride) Membrane. *Scientific Reports, 6*.

Hashim, N. A., Liu, F., & Li, K. (2009). A simplified method for preparation of hydrophilic PVDF membranes from an amphiphilic graft copolymer. *Journal of Membrane Science, 345*(1), 134-141.

He, J., Al-Masri, D., MacFarlane, D. R., & Pringle, J. M. (2016). Temperature dependence of the electrode potential of a cobalt-based redox couple in ionic liquid electrolytes for thermal energy harvesting. *Faraday discussions*.

Hu, R., Cola, B. A., Haram, N., Barisci, J. N., Lee, S., Stoughton, S., . . . Gestos, A. (2010). Harvesting waste thermal energy using a carbon-nanotube-based thermo-electrochemical cell. *Nano letters, 10*(3), 838-846.

Huang, Z.-M., Zhang, Y.-Z., Kotaki, M., & Ramakrishna, S. (2003). A review on polymer nanofibers by electrospinning and their applications in nanocomposites. *Composites science and technology, 63*(15), 2223-2253.

Hwang, J.-Y., Kim, E. S., Hasan, S. W., Choi, S.-M., Lee, K. H., & Kim, S. W. (2015). Reduction of lattice thermal conductivity in PbTe induced by artificially generated pores. *Advances in Condensed Matter Physics, 2015*.

Im, H., Kim, T., Song, H., Choi, J., Park, J. S., Ovalle-Robles, R., . . . Lee, H. H. (2016). High-efficiency electrochemical thermal energy harvester using carbon nanotube aerogel sheet electrodes. *Nature communications, 7*.

Im, H., Moon, H. G., Lee, J. S., Chung, I. Y., Kang, T. J., & Kim, Y. H. (2014). Flexible thermocells for utilization of body heat. *Nano Research, 7*(4), 443-452.

Inan, T. Y., Doğan, H., & Güngör, A. (2013). PVdF-HFP membranes for fuel cell applications: effects of doping agents and coating on the membrane's properties. *Ionics, 19*(4), 629-641.

Jadhao, J., & Thombare, D. (2013). Review on exhaust gas heat recovery for IC engine. *International Journal of Engineering and Innovative Technology (IJEIT), 2*(12).

Ji, G.-L., Zhu, B.-K., Cui, Z.-Y., Zhang, C.-F., & Xu, Y.-Y. (2007). PVDF porous matrix with controlled microstructure prepared by TIPS process as polymer electrolyte for lithium ion battery. *Polymer, 48*(21), 6415-6425.

Jin, L., Greene, G. W., MacFarlane, D. R., & Pringle, J. M. (2016). Redox-Active Quasi-Solid-State Electrolytes for Thermal Energy Harvesting. *ACS Energy Letters, 1*(4), 654-658.

Kazim, A. H. (2017). *Novel Electrolytes and System Designs for Thermo-electrochemical Cells.* Georgia Institute of Technology.

Kazim, A. H., & Cola, B. A. (2016). Electrochemical Characterization of Carbon Nanotube and Poly (3, 4-ethylenedioxythiophene)− Poly (styrenesulfonate) Composite Aqueous Electrolyte for Thermo-Electrochemical Cells. *Journal of The Electrochemical Society, 163*(8), F867-F871.

Kim, T., Lee, J. S., Lee, G., Yoon, H., Yoon, J., Kang, T. J., & Kim, Y. H. (2017). High thermopower of ferri/ferrocyanide redox couple in organic-water solutions. *Nano Energy, 31*, 160-167.

Lanceros-Mendez, S., Mano, J., Costa, A., & Schmidt, V. (2001). FTIR and DSC studies of mechanically deformed β-PVDF films. *Journal of Macromolecular Science, Part B, 40*(3-4), 517-527.

Lazar, M. A., Al-Masri, D., MacFarlane, D. R., & Pringle, J. M. (2016). Enhanced thermal energy harvesting performance of a cobalt redox couple in ionic liquid–solvent mixtures. *Physical chemistry chemical physics, 18*(3), 1404-1410.

Li, M., Wondergem, H. J., Spijkman, M.-J., Asadi, K., Katsouras, I., Blom, P. W., & de Leeuw, D. M. (2013). Revisiting the δ-phase of poly (vinylidene fluoride) for solution-processed ferroelectric thin films. *Nature materials, 12*(5), 433-438.

Li, Z., Shan, F., Wei, J., Yang, J., Li, X., & Wang, X. (2008). High ionic conductive PVDF-based fibrous electrolytes. *Journal of Solid State Electrochemistry, 12*(12), 1629-1635.

Li, Z., & Wang, C. (2013). *One-dimensional nanostructures: electrospinning technique and unique nanofibers*: Springer.

Lu, C., Qi, W., Li, L., Xu, J., Chen, P., Xu, R., . . . Yu, Q. (2013). Electrochemical performance and thermal property of electrospun PPESK/PVDF/PPESK composite separator for lithium-ion battery. *Journal of Applied Electrochemistry, 43*(7), 711-720.

Markov, B. F., & Kuzyakin, E. (1972). Thermogalvanic Cells with a Single Fused Salt. *Russian Chemical Reviews, 41*(3), 250.

Martín-González, M., Caballero-Calero, O., & Díaz-Chao, P. (2013). Nanoengineering thermoelectrics for 21st century: Energy harvesting and other trends in the field. *Renewable and Sustainable Energy Reviews, 24*, 288-305.

Migita, T., Tachikawa, N., Katayama, Y., & Miura, T. (2009). Thermoelectromotive force of some redox couples in an amide-type room-temperature ionic liquid. *Electrochemistry, 77*(8), 639-641.

Mohanraman, R., Lan, T.-W., Hsiung, T.-C., Amada, D., Lee, P.-C., Ou, M.-N., & Chen, Y.-Y. (2015). Engineering nanostructural routes for enhancing thermoelectric performance: bulk to nanoscale. *Frontiers in Chemistry, 3*, 63.

Mua, Y., & Quickenden, T. (1996). Power conversion efficiency, electrode separation, and overpotential in the ferricyanide/ferrocyanide thermogalvanic cell. *Journal of The Electrochemical Society, 143*(8), 2558-2564.

Orazem, M. E., & Tribollet, B. (2011). *Electrochemical impedance spectroscopy* (Vol. 48): John Wiley & Sons.

Peng, L., Hu, L., & Fang, X. (2014). Energy Harvesting for Nanostructured Self-Powered Photodetectors. *Advanced Functional Materials, 24*(18), 2591-2610.

Poudel, B., Hao, Q., Ma, Y., Lan, Y., Minnich, A., Yu, B., . . . Vashaee, D. (2008). High-thermoelectric performance of nanostructured bismuth antimony telluride bulk alloys. *Science, 320*(5876), 634-638.

Pu, W., He, X., Wang, L., Jiang, C., & Wan, C. (2006). Preparation of PVDF–HFP microporous membrane for Li-ion batteries by phase inversion. *Journal of membrane science, 272*(1), 11-14.

Qian, W., Cao, M., Xie, F., & Dong, C. (2016). Thermo-Electrochemical Cells Based on Carbon Nanotube Electrodes by Electrophoretic Deposition. *Nano-Micro Letters*, 1-7.

Quickenden, T., & Mua, Y. (1995). The power conversion efficiencies of a thermogalvanic cell operated in three different orientations. *Journal of The Electrochemical Society, 142*(11), 3652-3659.

Quickenden, T., & Vernon, C. (1986). Thermogalvanic conversion of heat to electricity. *Solar Energy, 36*(1), 63-72.

Ratri, P. J., & Tashiro, K. (2013). Phase-transition behavior of a crystalline polymer near the melting point: case studies of the ferroelectric phase transition of poly (vinylidene fluoride) and the β-to-α transition of trans-1, 4-polyisoprene. *Polymer journal, 45*(11), 1107-1114.

Riedi, P. C. (1976). First Law of Thermodynamics *Thermal Physics: An Introduction to Thermodynamics, Statistical Mechanics and Kinetic Theory* (pp. 17-43). London: Macmillan Education UK.

Romano, M. S., Li, N., Antiohos, D., Razal, J. M., Nattestad, A., Beirne, S., . . . Wallace, G. G. (2013). Carbon nanotube–reduced graphene oxide composites for thermal energy harvesting applications. *Advanced Materials, 25*(45), 6602-6606.

Romano, M. S., Razal, J. M., Antiohos, D., Wallace, G., & Chen, J. (2015). Nano-carbon electrodes for thermal energy harvesting. *Journal of nanoscience and nanotechnology, 15*(1), 1-14.

Salazar, P. F., Kumar, S., & Cola, B. A. (2012). Nitrogen-and boron-doped carbon nanotube electrodes in a thermo-electrochemical cell. *Journal of The Electrochemical Society, 159*(5), B483-B488.

Salazar, P. F., Kumar, S., & Cola, B. A. (2014). Design and optimization of thermo-electrochemical cells. *Journal of Applied Electrochemistry, 44*(2), 325-336.

Salazar, P. F., Stephens, S. T., Kazim, A. H., Pringle, J. M., & Cola, B. A. (2014). Enhanced thermo-electrochemical power using carbon nanotube additives in ionic liquid redox electrolytes. *Journal of Materials Chemistry A, 2*(48), 20676-20682.

Shin, J., Nho, Y.-C., seon Hwang, I., Fei, G., Kim, A. R., & Nahm, K. S. (2010). Irradiated PVdF-HFP–tin oxide composite membranes for the applications of direct methanol fuel cells. *Journal of membrane science, 350*(1), 92-100.

Singh, V. V., Nigam, A. K., Batra, A., Boopathi, M., Singh, B., & Vijayaraghavan, R. (2012). Applications of ionic liquids in electrochemical sensors and biosensors. *International Journal of Electrochemistry, 2012*.

Snyder, G. J., & Toberer, E. S. (2008). Complex thermoelectric materials. *Nature materials, 7*(2), 105-114.

Song, D., Xu, C., Chen, Y., He, J., Zhao, Y., Li, P., . . . Fu, F. (2015). Enhanced thermal and electrochemical properties of PVDF-HFP/PMMA polymer electrolyte by TiO 2 nanoparticles. *Solid State Ionics, 282*, 31-36.

Sosnowska, A., Barycki, M., Gajewicz, A., Bobrowski, M., Freza, S., Skurski, P., . . . Jeandupeux, L. (2016). Towards the Application of Structure–Property Relationship Modeling in Materials Science: Predicting the Seebeck Coefficient for Ionic Liquid/Redox Couple Systems. *ChemPhysChem, 17*(11), 1591-1600.

Taylor, S., & Gileadi, E. (1995). Physical interpretation of the Warburg impedance. *Corrosion, 51*(9), 664-671.

Telkes, M. (1947). The Efficiency of Thermoelectric Generators. I. *Journal of Applied Physics, 18*(12), 1116-1127.

Tritt, T. M. (2011). Thermoelectric phenomena, materials, and applications. *Annual review of materials research, 41*, 433-448.

Uhl, S., Laux, E., Journot, T., Jeandupeux, L., Charmet, J., & Keppner, H. (2014). Development of flexible micro-thermo-electrochemical generators based on ionic liquids. *Journal of electronic materials, 43*(10), 3758-3764.

Wan, L., Zhang, Q., Wang, S., Wang, X., Guo, Z., Dong, B., . . . Wang, B. (2015). A two-step reduction method for synthesizing graphene nanocomposites with a low loading of well-dispersed platinum nanoparticles for use as counter electrodes in dye-sensitized solar cells. *Journal of Materials Science, 50*(12), 4412-4421.

Wei, D., & Ivaska, A. (2008). Applications of ionic liquids in electrochemical sensors. *Analytica Chimica Acta, 607*(2), 126-135.

Wu, D., He, J., Zhang, M., Ni, P., Li, X., & Hu, J. (2015). Fabrication of a novel sandwich-like composite separator with enhanced physical and electrochemical performances for lithium-ion battery. *Journal of Power Sources, 290*, 53-60.

Wu, J., Black, J. J., & Aldous, L. (2016). Thermoelectrochemistry using conventional and novel gelled electrolytes in heat-to-current thermocells. *Electrochimica Acta*.

Wu, N., Jing, B., Cao, Q., Wang, X., Kuang, H., & Wang, Q. (2012). A novel electrospun TPU/PVdF porous fibrous polymer electrolyte for lithium ion batteries. *Journal of Applied Polymer Science, 125*(4), 2556-2563.

Wu, Q.-Y., Liang, H.-Q., Gu, L., Yu, Y., Huang, Y.-Q., & Xu, Z.-K. (2016). PVDF/PAN blend separators via thermally induced phase separation for lithium ion batteries. *Polymer, 107*, 54-60.

Xiao, S., Yang, Y., Li, M., Wang, F., Chang, Z., Wu, Y., & Liu, X. (2014). A composite membrane based on a biocompatible cellulose as a host of gel polymer electrolyte for lithium ion batteries. *Journal of Power Sources, 270*, 53-58.

Yamato, Y., Katayama, Y., & Miura, T. (2013). Effects of the interaction between ionic liquids and redox couples on their reaction entropies. *Journal of The Electrochemical Society, 160*(6), H309-H314.

Yang, P., Liu, K., Chen, Q., Mo, X., Zhou, Y., Li, S., . . . Zhou, J. (2016). Wearable Thermocells Based on Gel Electrolytes for the Utilization of Body Heat. *Angewandte Chemie, 128*(39), 12229-12232.

Yanilmaz, M., Zhu, J., Lu, Y., Ge, Y., & Zhang, X. High-strength, thermally stable nylon 6, 6 composite nanofiber separators for lithium-ion batteries. *Journal of Materials Science,* 1-10.

Yu, J., Huang, X., Wu, C., & Jiang, P. (2011). Permittivity, thermal conductivity and thermal stability of poly (vinylidene fluoride)/graphene nanocomposites. *IEEE Transactions on Dielectrics and Electrical Insulation, 18*(2), 478-484.

Yuan, X.-Z., Song, C., Wang, H., & Zhang, J. (2010). *EIS equivalent circuits*: Springer.

Zhai, Y., Wang, N., Mao, X., Si, Y., Yu, J., Al-Deyab, S. S., . . . Ding, B. (2014). Sandwich-structured PVdF/PMIA/PVdF nanofibrous separators with robust mechanical strength and thermal stability for lithium ion batteries. *Journal of Materials Chemistry A, 2*(35), 14511-14518.

Zhao, C., Xu, X., Chen, J., & Yang, F. (2013). Effect of graphene oxide concentration on the morphologies and antifouling properties of PVDF ultrafiltration membranes. *Journal of Environmental Chemical Engineering, 1*(3), 349-354.

Zhou, H., Yamada, T., & Kimizuka, N. (2016). Supramolecular Thermo-Electrochemical Cells: Enhanced Thermoelectric Performance by Host–Guest Complexation and Salt-Induced Crystallization. *Journal of the American Chemical Society*.

Zinovyeva, V., Nakamae, S., Bonetti, M., & Roger, M. (2014). Enhanced thermoelectric power in ionic liquids. *ChemElectroChem*, *1*(2), 426-430.